

Summer 2001

# Electrostatic micro actuators for mirror and other applications

Xingtao Wu

*New Jersey Institute of Technology*

Follow this and additional works at: <https://digitalcommons.njit.edu/dissertations>



Part of the [Other Physics Commons](#)

---

## Recommended Citation

Wu, Xingtao, "Electrostatic micro actuators for mirror and other applications" (2001). *Dissertations*. 508.  
<https://digitalcommons.njit.edu/dissertations/508>

This Dissertation is brought to you for free and open access by the Theses and Dissertations at Digital Commons @ NJIT. It has been accepted for inclusion in Dissertations by an authorized administrator of Digital Commons @ NJIT. For more information, please contact [digitalcommons@njit.edu](mailto:digitalcommons@njit.edu).

## **Copyright Warning & Restrictions**

The copyright law of the United States (Title 17, United States Code) governs the making of photocopies or other reproductions of copyrighted material.

Under certain conditions specified in the law, libraries and archives are authorized to furnish a photocopy or other reproduction. One of these specified conditions is that the photocopy or reproduction is not to be “used for any purpose other than private study, scholarship, or research.” If a user makes a request for, or later uses, a photocopy or reproduction for purposes in excess of “fair use” that user may be liable for copyright infringement,

This institution reserves the right to refuse to accept a copying order if, in its judgment, fulfillment of the order would involve violation of copyright law.

**Please Note: The author retains the copyright while the New Jersey Institute of Technology reserves the right to distribute this thesis or dissertation**

Printing note: If you do not wish to print this page, then select “Pages from: first page # to: last page #” on the print dialog screen

The Van Houten library has removed some of the personal information and all signatures from the approval page and biographical sketches of theses and dissertations in order to protect the identity of NJIT graduates and faculty.

## **ABSTRACT**

### **ELECTROSTATIC MICROACTUATORS FOR MIRROR AND OTHER APPLICATIONS**

**by**  
**Xingtao Wu**

Micro-electro-mechanical systems (MEMS) based electrostatic micro actuators are becoming important building blocks for innovations in optical signal processing and computing systems due to their inherently small size, high density, high speed and low power consumption. Generally, the principle of operation in these systems can be described as: an electrostatic attractive force causes a mechanical rotation, translation or deformation of a mirror plate, controlling the power, phase or direction of a light beam while it propagates through some medium or through free space. The fast paced, competitive research and development efforts widely being undertaken, both in academia and industry, are demanding simple, fast methods for the design of quasi-static mirror systems, with a large, stable, analog range of operation. In addition fast prototyping methods are in demand for the proof of concept fabrication of these mirror designs. This dissertation addresses these research topics by presenting 1) a general capacitance-based quasi-static design theory and methodology for electrostatic micro actuators, 2) a study of electrostatic travel range extension methods to minimize the pull in effect, and 3) a fast prototyping approach for electrostatic mirror devices using ultra thin silicon wafer bonding and deep reactive etching technologies.

In the first topic, two fundamental capacitance-based differential equations are developed for the quasi-static description of electrostatic micro actuator systems. A structural equation is developed to represent the coupled electromechanical response of



the system under applied voltage bias, and a pull in equation is determined to identify the intrinsic collapse point beyond which an actuator system no longer has a stable equilibrium, the so-called pull in point. These equations are applied to various complex electrostatic micro actuator systems to predict specific quasi-static behavior. A unitless equation is introduced for each actuator category, and based on it, a design method is proposed to quickly provide specifications for a particular desired performance of an electrostatically actuated micro-mirror system.

In the second topic, and as an application of the proposed design methodology, the travel range extension issue is addressed leading to two new methods to increase travel range by sacrificing driving voltage. Both methods are applied directly in the electrostatic domain. The first method utilizes a series capacitor to modulate the effective actuation voltage across the variable capacitor micro mirror. The second method utilizes negative feedback due to the coulombic repulsive interaction between charge layers inserted between the micro mirror electrodes. An analytical study of representative mirror devices is presented, and verification of the travel range extension models is provided via finite element analysis (FEA) simulation.

As a further application of the design methodology developed as part of the first research topic, three state-of-the-art micro actuator systems are designed and studied: 1) a variable optical attenuator (VOA), 2) an optical cross connect device (OXC) and 3) an electrostatically tunable, wavelength selecting device. FEA simulations are used to confirm design specifications.

In the third research topic, VOA and electrostatically tunable, wavelength selecting devices are fabricated using fast prototyping via ultra thin wafer bonding and deep reactive etching (DRIE) technologies. Both silicon wet-etching and SU-8 patterning

are investigated for the formation of mirror gaps. Testing in the mechanical domain and partial device characterization in the optical domain is provided for these devices.

Finally, as a demonstration that the actuator design approach developed in this thesis can be applied to systems other than micro mirrors, we use the approach to design an innovative true mass flow sensor using an electrostatic resonant beam as the sensing element.

**ELECTROSTATIC MICROACTUATORS FOR MIRROR AND OTHER  
APPLICATIONS**

**by**

**Xingtao Wu**

**A Dissertation  
Submitted to the Faculty of  
New Jersey Institute of Technology and  
Rutgers, The State University of New Jersey - Newark  
In Partial Fulfillment of Requirement for the Degree of  
Doctor of Philosophy in Applied Physics**

**Federated Department of Physics**

**August 2001**

Copyright © 2001 by Xingtao Wu

ALL RIGHT RESERVED

## **APPROVAL PAGE**

### **ELECTROSTATIC MICROACTUATORS FOR MIRROR AND OTHER APPLICATIONS**

**Xingtao Wu**

Dr. Kenneth R. Farmer, Dissertation Advisor Associate Professor of Physics, NJIT	Date
---	------

Dr. John F. Federici, Committee Member Professor of Physics, NJIT	Date
--	------

Dr. Dentcho V. Ivanov, Committee Member Director, Microfabrication Center, NJIT	Date
--	------

Dr. Chuni L. Ghosh, Committee Member President, Princeton Optronics, Inc.	Date
--	------

Dr. Earl D. Shaw, Committee Member Professor of Physics, Rutgers University, Newark	Date
--	------

## BIOGRAPHICAL SKETCH

**Author:** Xingtao Wu  
**Degree:** Doctor of Philosophy  
**Date:** August 27, 2001

### Undergraduate and Graduate Education:

- Doctor of Philosophy in Applied Physics,  
New Jersey Institute of Technology, Newark, NJ, 2001
- Master of Science in Physics,  
Sichuan Union University (Now Sichuan University), Chengdu, P. R. China, 1998
- Bachelor of Science in Physics,  
Sichuan Normal University, Chengdu, P. R. China, 1993

**Major:** Applied Physics

### Presentations and Publications:

Xingtao Wu, Richard A Brown, Smitha Mathews and K.R. Farmer,  
“The Effects of Oxide on the Travel Range Extension of Electrostatic Micro Mirror”, OMEMS 2000, IEEE, pp. 198-199.

Xingtao Wu, ZhiXiong Xiao, Jiang Zhe and K.R. Farmer,  
“Two Passive Methods to Extend the Travel Range of Electrostatic Micro Actuators”, Technical Proceedings of the MSM 2001 International Conference on Modeling and Simulation on Microsystems, pp. 342-346, Hilton Head Island, March 21-24, 2001.

Xingtao Wu, Jiang Zhe, Jingshan Wang, Jin Cheng, Vijay Modi, and K. R. Farmer,  
“A generalized capacitance-based model for the quasi-static description of electrostatic micro-actuators”, Have been Submitted to IEEE Transaction on Journal of MEMS

S. K. Sampath, L. St. Clair, Xingtao Wu, D. V. Ivanov, Q. Wang, C. Ghosh and K. R. Farmer,  
“Rapid MEMS Prototyping using SU-8, Wafer Bonding and Deep Reactive Ion Etching”, Proceedings of 13<sup>th</sup> Conference of UGIM, June 17-20, 2001, pp. 158-161.

Jiang Zhe, Xingtao Wu, Jin Cheng, Jingshan Wang and K. R. Farmer,  
“Analytic Pull-in Study on Non-deformable Electro Static Micro Actuators”,  
submitted to IEEE 2001 International Electron Device Meeting.

Zhixiong Xiao, Xingtao Wu, Wuyong Peng and K. R. Farmer,  
“An Angle Based Design Approach for Rectangular Electrostatic Torsion Actuators”, accepted by IEEE Transaction on Journal of MEMS.

Jin Cheng, Jiang Zhe, Xingtao Wu and K. R. Farmer,  
“Analytical and FEM Simulation Pull-in Study on Deformable Electrostatic Micro Actuators”, Submitted to IEEE MEMS 2002.

Xingtao Wu and K. R. Farmer  
“Simulation, Modelling and Optimization of A Micromachined Resonant Beam Coriolis Mass Flow Sensor”, to be submitted.

This dissertation is dedicated  
to my beloved family



## ACKNOWLEDGMENT

I wish to express my deepest appreciation to my advisor, Professor K. R. Farmer, for his great guidance throughout the whole research. Without his support, I could never complete this research topic.

Special thanks to the other members of the committee: Dr. John Federici, Dr. Dentcho Ivanov, Dr. Chuni Ghosh and Dr. Earl Shaw for their careful review of the dissertation and helpful comments.

I would like to thank Jiang Zhe for the computing and helpful suggestions. I would also like to thank Dr. Jingshan Wang for the productive discussions on physics aspect of electrostatic actuators.

I am very grateful to the staff of the Microelectronics Research Center of NJIT for their administrative work during the research, especially Ms. Lynn Stover. This work was supported partially by the NJMEMS Initiative by the New Jersey Commission on Science and Technology (NJCST). I would also like to thank Wuyong Peng, Dianhong Luo and other fellow students for helpful discussions during the study.

Finally, I would like to thank my parents and my family for their continuous support, encouragement and best wishes that were very important while I pursued my doctoral studies. I dedicate this thesis to the memory of my mother, Luo Jinping.

## TABLE OF CONTENTS

Chapter	Page
1 INTRODUCTION.....	1
2 QUASI-STATIC ANALYSIS AND DESIGN OF ACTUATORS.....	8
2.1 Introduction.....	8
2.1.1 A General Theory for the Quasi-static Description of Electrostatic Micro Actuators.....	8
2.1.2 Actuator Classification and Quasi-static Design Methodology .....	16
2.1.3 Pull-in Study of Non-Deformable Actuator Systems.....	21
2.2 Travel Range Extension Methods.....	26
2.2.1 Introduction.....	26
2.2.2 Series Capacitor Method.....	28
2.2.3 Charge Injection Method.....	31
2.2.4 Simulations on Series Capacitor Method.....	32
2.2.5 Simulations and Experiments on Charge Injection Method.....	35
2.3 Pull in Analysis of Complex Actuator Systems.....	39
2.3.1 Result Summary from Direct Force Analysis.....	39
2.3.2 Torsion actuators with general power function electrodes.....	41
2.3.3 The Effect of Strain Stiffening.....	43
2.3.4 The Effect of Fringe Field Capacitance.....	44

## TABLE OF CONTENTS (Continued)

Chapter	Page
3 STUDY OF EXAMPLE DEVICE APPLICATIONS.....	46
3.1 Variable Optical Attenuator.....	47
3.1.1 Introduction.....	47
3.1.2 The Effect of Gravity.....	49
3.1.3 Fabrication by Ultra Thin Silicon Wafer Fusion Bonding and Deep Reactive Etching .....	51
3.1.4 The Effect of Trapped Charges.....	54
3.2 Fabry-Perot Wavelength Selector.....	57
3.2.1 Basics of Fabry-Perot Filter.....	57
3.2.2 Mirror Plate Direct Actuation scheme.....	60
3.2.3 Mirror Tuning with Proximity Actuators.....	65
3.2.4 Mirror Tuning with Proximity Actuators.....	65
3.2.5 Fast Prototyping by Silicon Wafer Bonding using SU-8 as Spacer.....	68
3.3 Analysis of High Angular Deflection Electrostatic Mirror with Shaped Electrodes.....	72
3.4 Device Concept of Resonant Beam True Mass Flow Sensor .....	80
3.4.1 Introduction.....	80
3.4.2 Mode Analysis.....	83
3.4.3 Beam to String Transform.....	86

**TABLE OF CONTENTS**  
**(Continued)**

<b>Chapter</b>	<b>Page</b>
4 CONCLUSIONS AND DISCUSSION.....	88
APPENDIX: PUBLICATIONS AND MANUSCRIPTS.....	92
REFERENCES.....	131

## LIST OF TABLES

Table	Page
1.1 The Comparison of typical microactuation mechanisms for optical MEMS research and development.....	2
3.1 Summary of dimension and material parameters under tests.....	57
3.2 Pull-summary of shaped electrode actuation scheme.....	80
3.3 Mode frequency dependence on material density being measured (device sample 6).....	86

## LIST OF FIGURES

Figure	Page
1.1 An ideal one-dimensional parallel-plate electrostatic actuator with linear restoring force and graph showing actuator deflection versus voltage.....	4
1.2 Light transmittance versus wavelength .....	6
2.1 A sketch of model of a 3D electrostatic actuator system .....	9
2.2 Design flow for 1D actuator system. The equation for the actuation curve usually can be specified for each specified actuator type.....	12
2.3 Characteristic actuation equation of pure torsion actuators and parallel plate actuators.....	13
2.4 The schematic of a torsion actuator with a rigid center boss. The boss is viewed as rigid body during actuation and the rotational sections are viewed as wedge-shaped for small gap and displacement.....	14
2.5 Pull in dependence on the length ratio of a wedge-shape capacitor with center boss.....	15
2.6 Detailed actuator list with variation factors. Each line links to the center bar representing an actuator type with one variation factor.....	18
2.7 A stream down flow illustrating the pull-in based design method.....	20
2.8 Schematic view of a series connected capacitor network with one capacitor fixed.....	22
2.9 The schematics of torsion mirrors with far-spring-end and near-spring-end electrode actuation, respectively.....	23
2.10 Analytical unitless pull-in position $\Theta$ of cantilever rectangular torsion actuators with electrode located at the far-end from the torsion springs.....	24
2.11 Layout and cross section views of full elliptic-electrode-actuated torsion actuator.....	25

## LIST OF FIGURES (Continued)

Figure		Page
2.12	Effect of semi axis $a$ and $b$ on unitless pull in position $\theta$ of full elliptic electrode actuation.....	25
2.13	Circuit of Series Capacitor Loop.....	28
2.14	Torsion Micro Mirror with Oxides.....	31
2.15	Effective Actuation Voltage vs. Applied Bias Voltage for Different Capacitance Ratio ( $R=C_s/C_{ao}$ ) for Vertical Z Actuator.....	33
2.16	Normalized Deflection vs. Applied Voltage for Different Capacitance Ratios. Vertical Z Actuator VC1 with Gap Depth=4 $\mu$ m.....	34
2.17	Normalized Deflection vs. Applied Voltage for NC3 Torsion Mirror with Gap Depth=12 $\mu$ m.....	35
2.18	finite element meshing of D3 mirror, 7179 8-node block elements with 33409 nodes.....	36
2.19	finite element meshing of C3 mirror, 940 8-node block elements with 6698 nodes.....	37
2.20	Simulation of C3 device response to applied voltage.....	37
2.21	Simulation of D3 device response to applied voltage.....	38
2.22	C-V curve at 1KHz, indicating a 6.5V shift.....	38
2.23	The Measured Effects of Oxides on The Deflection Dependence on Bias Voltage for D3 Device.....	39
2.24	The effect of power index on the normalized pull-in displacement.....	42
2.25	The effect of stiffness coefficient ratio on the normalized pull-in displacement for torsion actuator.....	44
2.26	The effect of fringe field on system pull in.....	45

## LIST OF FIGURES (Continued)

Figure		Page
3.1	Schematic of the large area torsion mirror used as optical attenuator.....	48
3.2(A)	Schematic of the fabrication sequence: cavities are anisotropically etched into a standard thickness silicon wafer which is subsequently oxidized.....	51
3.2(B)	An ultra-thin silicon wafer is fusion bonded over the etched wafer, forming sealed cavities.....	51
3.2(C)	The mirror surface and springs are patterned into the top wafer for DRIE.....	51
3.2(D)	Completed devices with Cr/Au coating for high reflectivity.....	51
3.3(A)	SEM Micrograph of one of the micromirror structures.....	52
3.3(B)	Close-up views of the springs formed by deep reactive ion etching.....	52
3.3(C)	Close-up views of the springs formed by deep reactive ion etching For scale, the top sections of the springs are 10 $\mu$ m wide.....	52
3.4	SEM Micrograph of DRIE side walls of one of the micromirror structures, and mounting for quasi-static test.....	52
3.5	Wyko profilometer data, showing mirror deflection at 55 volts. (top) Profilometer image of the actuated device, confirming that the deflection is only along the symmetry axis, and (bottom) data extracted along the symmetry axis, showing a deflection of $\sim 7\mu$ m at the mirror tip at this applied voltage.....	53
3.6	Mirror displacement data extracted from Wyko profilometer along the mirror length confirming that the deflection is only along the symmetry axis and the flatness of the mirror reflective surface even at its pull-in state.....	53
3.7	Zero bias profiles of D3 device along the mirror length showing an upward deflection.....	55
3.8	A simple optical scheme of a Fabry-Perot filter.....	57



## LIST OF FIGURES (Continued)

Figure		Page
3.9	Layout of two types of spring configurations.....	60
3.10	Spring stiffness comparison for two types of spring configurations with various folded-spring numbers.....	61
3.11	Comparison of mode frequencies and spring configurations. “2 spr-side” and “2 spr-corner” represent two springs along each side or corner of the square mirror, respectively, etc.....	62
3.12(A)	Finite element meshing of the mirror structure, meshing uses 3200 8-node block elements with 14395 nodes.....	63
3.12(B)	The graph shows the meshing of the elastic folded springs. This high stress area requires fine meshing.....	63
3.12(C)	The graph illustrates the mirror behavior under 100V bias electrostatic load, showing a maximum displacement of 2.76 $\mu\text{m}$ in z direction. The system capacitance at this deflection is 0.289pF and force in the z-direction is $F_z=8.44\mu\text{N}$ .....	63
3.12(D)	The graph shows the Mise stress distribution through the mirror and spring structure, and high stress density occurs at mirror-to-spring and spring-to-fixed bank junctions as expected.....	63
3.13	Graph of the first 6 mode shapes of “4 spr-corner” device shows the lowest frequency at vertical bending mode, and the cornered spring configuration introduces torsion modes at higher order.....	64
3.14	The graph is the electrostatic response of “4 spring-corner” device showing $\sim 0.78\mu\text{m}$ piston-only deflection at $\sim 50\text{V}$ , which corresponds to a full wavelength phase shift.....	64
3.15	Electrostatic response of “4 spring-corner” device showing a full wavelength phase shift at $\sim 50\text{V}$ .....	65
3.16	Shape graph of the springs under electrostatic load for small amplitude deflection. The springs are mainly working in the torsion mode such that the system pull in is increased from 1/3 to $\sim 44\%$ , which implies that further reduction of actuation voltage is possible by decreasing the air gap depth of the actuators.....	66
3.17(A)	Sampling of the electrostatic actuated mirror, purple balls indicate sampling points.....	67

## LIST OF FIGURES (Continued)

Figure	Page
3.17(B) The graph shows the deflection profile extracted from sampling points displayed in 3.17(A).....	67
3.17(C) The graph illustrates the mirror behavior under 80V bias electrostatic load, showing a maximum displacement magnitude of 2.3 $\mu\text{m}$ in z direction. This maximum deflection is uniform across the whole area of the center mirror.....	67
3.17(D) The graph shows the Mise stress distribution through the mirror and spring structure. The four beams at four corners of the center square mirror are operating at bending mode, and the springs linking 4 actuator plates to fixed ends are taking zigzag shape, implying that these springs are working mainly at torsion mode.....	67
3.18 Patterned 3" ultra-thin Silicon wafer (50 $\mu\text{m}$ ) bonded to a patterned 4" Substrate having SU-8 structures, and close-up of a region showing good alignment and bonding.....	69
3.19 Cross sectional view of mirror device fabricated through 5 major developing steps.....	70
3.20 Surface profile of a fabricated mirror structure using SU-8 as mirror spacer and bonding interface layer.....	71
3.21 Graph illustrating the optical performance at transmission mode for 0V and 40V .....	71
3.22 Graph illustrating the optical performance at transmission mode from 0V to 100V biases for a mirror using 5 folded spring suspension.....	72
3.23 Graph shows the typical layout of an 2D mirror with two rotational stages along the x and y axis, respectively. The mirror shape is investigated as elliptical and assumed to have a larger area than the bottom electrodes so that the actuation properties will mainly be determined the shapes and sizes of the bottom electrodes.....	73
3.24 Solution of unitless pull in position $\theta$ of full hyperbolic electrode actuation under different ratios of $a/a_0$ , $b/b_0$ and $L/L_0$ . $a_0$ , $b_0$ and $L_0$ are reference semi axis and electrode length.....	75

## LIST OF FIGURES (Continued)

Figure		Page
3.25	Effect of constant $p$ and electrode length $L$ on unitless pull in position $\Theta$ of full parabolic electrode ( $y^2 = px$ ) actuation. $L_0$ is reference electrode length.....	76
3.26	Partial actuation scheme of elliptic-shaped electrode.....	77
3.27	Analytical unitless pull in position $\Theta$ of partial elliptic, hyperbolic, triangular and parabolic ( $y^2 = px$ ) results.....	78
3.28	Comparison between MEMCAD simulation and analytical results of a circular electrode. The simulation is based on a circular electrode with radius of $200\mu\text{m}$ , $d=12\mu\text{m}$ , $\gamma=L_1/L$ from 0.43 to 1.0.....	79
3.29	A schematic graph showing the operational principle of mass flow measurement using resonant beam vibration pick-up scheme.....	81
3.30	A block diagram illustrating the relationship among the three vibrations of the device.....	82
3.31	An 3D solid view of the device showing the fabrication layers and electrode configurations.....	83
3.32	Mode shapes for the double-loops structure.....	84
3.33	Natural frequency vs. mode number for double loop structures with various dimensional sizes.....	84
3.34	Mode frequency dependence on material density being measured (Device Sample 6).....	85
3.35	The mode frequency variation due to changes of beam length.....	86

## CHAPTER 1

### INTRODUCTION

The foundation of Micro-Electro-Mechanical Systems (MEMS) technology dates back at least to the early 1960s [1]. The field has given rise to many important applications, particularly in inertial and pressure sensing. It is believed that the next innovative implementation of MEMS technology will include applications in the optical signal processing and computing field [2] where MEMS based micro optic devices inherently offer small size, high density, high speed, low power consumption and high reliability. This emerging optical MEMS technology favors the electrostatic actuation mechanism, based in part on the fact that the elastic properties of MEMS structural materials and the electric field of the free space gap scale differently with decreasing device dimensions. It is found that micron-sized gaps, which are frequently used in microactuator systems, can generate electric fields higher than  $10^6(\text{Vm}^{-1})$  by application of only several volts bias voltage. In Table 1.1, a comparison of different microactuation schemes is given to support the MEMS community's current preference to use electrostatic actuation over other mechanisms. In part, because of its better compatibility with existing IC technology, as indicated in Table 1.1, electrostatic actuators are expected to become one of the most common micro-mechanical components in developing complex optics-oriented micro-systems.

Electrostatic actuator based micro mirrors are usually referred to as those microscopic optical mirrors that display mechanical motion through a capacitor system in response to an external bias voltage or current source. Generally, the principle of operation in these systems can be described as: an electrostatic attractive force causes a

mechanical rotation, translation or deformation of a mirror plate, controlling the power, phase or direction of a light beam while it propagates through some medium or through free space. “*There is plenty of room at the bottom*” [3]. As for optical MEMS (OMEMS) devices, if the light wavelength that is being modulated or steered is much smaller than the physical size of the micro mirror, the micro lever mirror displacement, as can be actuated by electrostatic forces, will be sufficient for light modulation and steering purposes. OMEMS are becoming important building blocks for the innovations of optical signal processing and computing systems. For example, electrostatic actuator based OMEMS switching fabric is a critical sub system in the all-optical network that is currently being considered for dynamic traffic control of DWDM wavelengths [4]. Other typical devices currently under research and development (R&D) are tunable optical attenuators [5], optical filters [6], spatial light modulators [7], light valves [8], interferometers and spectrometers [9] and micro displays [10], to name a few. R&D efforts are currently being widely undertaken, both in academia and industry, and the fast paced competitive atmosphere demands 1) a simple methodology for the design of the electrostatically driven mirror systems [11], 2) a much larger, stable range of micromirror operation before the so-called pull in instability occurs [12], and 3) a fast prototyping method for the realization of proof of concept devices to demonstrate mirror designs.

**Table 1.1** Comparison of typical microactuation mechanisms for optical MEMS research and development

Actuation Mechanism	Power consumption	Force density	Switching rate	Electronics source	Standard IC compatibility
Electromagnetic	Low	Medium	ms~ $\mu$ s	High current	Poor
Electrostatic	Low	Medium	ms~ $\mu$ s	High voltage	Good
Thermal	High	High	<ms	Medium voltage	Normal

In general, the quasi-static modeling of an electrostatic actuator system demands self-consistent computing in the coupled electrostatic and mechanical elastic energy domains. Quasi-static characteristics can be obtained by finite element method (FEM) [13-17], but the complex solid building and meshing processes require expert know-how, and the final time-consuming computation demands enhanced hardware sources. Furthermore, the FEM treatment is deficient in identifying dynamic properties, which are, at present, alternatively treated by macromodeling the actuators using system level circuit simulators [18,19]. In comparison to FEM methods, analytical approaches are efficient for simple systems such as vertical piston-only and pure torsion actuators [20], but because it has been traditionally implemented by balancing electrostatics force with elastic restoring forces, it has been difficult to apply to complex actuator systems where expressions for the force equations are not straightforward. Examples of such complex systems include actuators with shaped electrodes, systems with built-in strain stiffening and systems where the effects of fringing fields cannot be ignored. This force-balancing approach is also awkward when applied to systems where both torsion and bending are important. Also, the approach is challenging when applied to systems with more than one degree of freedom (DOF). For these reasons, the focus of the dissertation is on applying capacitance-based theory for analytical modeling, avoiding the difficulties of the force-balanced approach. The quasi-static properties of a wide range of simple and complex systems are treated using capacitance-based equations, and the effectiveness of the approach is verified using both software-based FEA simulations and, in some cases, comparison with measured data using microfabricated structures.

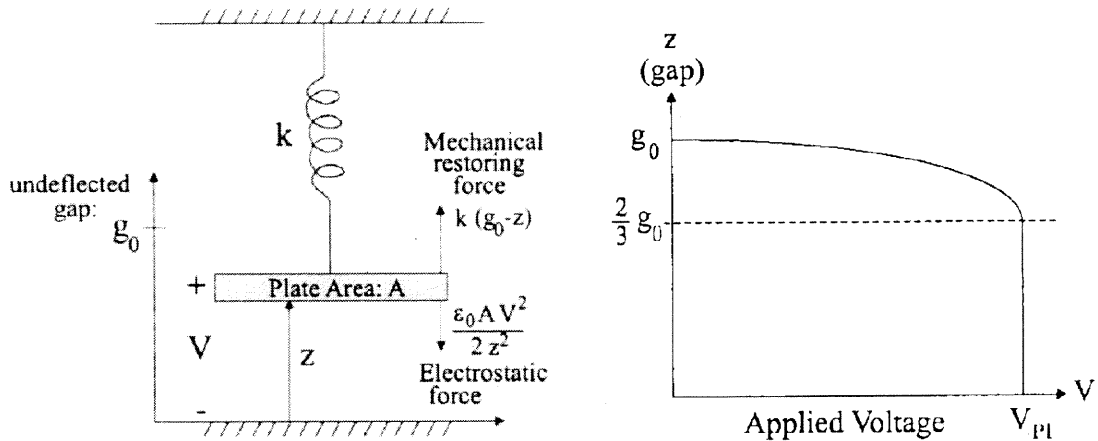


**Figure 1.1** An ideal one-dimensional parallel-plate electrostatic actuator with linear restoring force and graph showing actuator deflection versus voltage [21].

One important quasi-static property of electrostatic actuators is the pull in phenomenon. Due to the nonlinear electrostatic force, the electrostatic actuation intrinsically exhibits a pull in phenomenon in which the elastic restoring force cannot balance the electrostatic force, causing the movable electrode plate to collapse down into the well to make mechanical contact with the substrate or counter electrode. Fig. 1.1 illustrates the mechanism of the pull in event by using a simple parallel plate actuator. The range of motion for analog tuning is limited by this instability. “Leveraged bending” and “strain stiffening” approaches have been introduced to extend the stable travel range [21]. These methods are applied in the mechanical domain. In this thesis, two new travel range methods are introduced, which are applied directly in the electrostatic domain.

Many alternative micro mirror device concepts are being considered for optical applications [22, 23], making it necessary rapidly fabricate prototypes in order to quickly verify these concepts. Bulk micromachining is desirable since it allows for the creation of optically flat surfaces and the application of multiple stress isolation techniques. Single crystal silicon substrates are desirable for many reasons related to the properties of silicon including:

1. High ratio of modulus over volume density
2. Low defect density and high fracture strength
3. Good transparency at IR wavelengths
4. Standard CMOS compatibility
5. Optical coating compatibility

As can be seen in Fig. 1.2, which plots the dependence of light transmittance versus light wavelength, for light wave manipulation at IR wavelengths, the lightly doped silicon substrate is a good candidate as a transmission medium. Through the implementation of commercially available ultra thin silicon wafers, the actuation voltage of the bulk micromachined devices can be decreased to an acceptable level while, at the same time, maintaining high enough switching speed. Deep reactive ion etching (DRIE) enables the high aspect ratio vertical micromachining. At the same time, this method leaves the optical surface of interest untouched by, for example, the wet etching chemicals used in alternative approaches that are believed to roughen the mirror, and hence deteriorate optical performance [24].

The above three topics have been studied at the Microelectronics Research Center (MRC), at New Jersey Institute of Technology (NJIT), in the efforts to develop wafer-bonded micro-mirror technology for device applications involving the modulation and steering of IR light. This dissertation addresses these topics by 1) presenting a general electrostatic microactuator design theory and methodology, 2) elaborating new electrostatic travel range extension methods, and 3) investigating fast prototyping of micro-mirror devices using ultra thin silicon wafer bonding and deep reactive etching technologies.



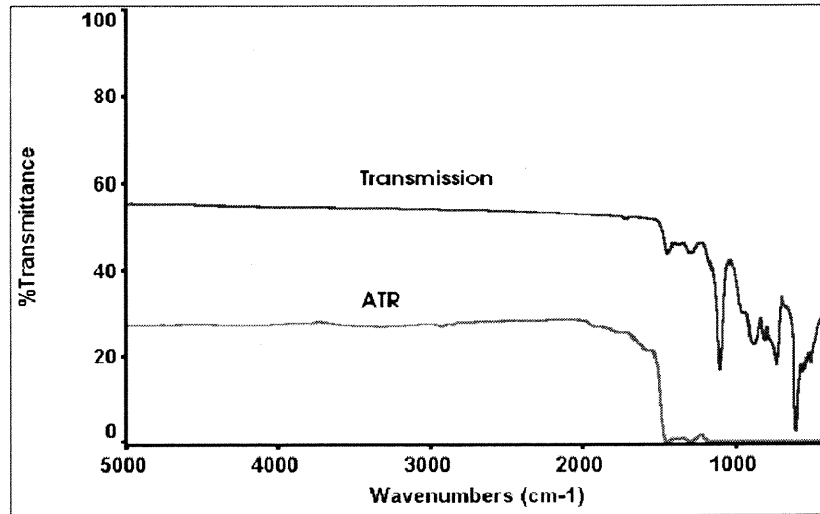


**Figure 1.2** Light transmittance versus wavelength.

In this dissertation, the design methodology of mirror devices is discussed in detail in Chapter 2. It includes:

(1) Introduction (section 2.1) --- A Theory for Quasi-static Descriptions of Electrostatic Micro Actuators (section 2.1.1), Quasi-static Design Methodology and Actuator Classification (section 2.1.2), and Pull in studies of non-deformable torsion actuator systems (sections 2.1.3);

(2) Electrostatic methods of the travel range extension (section 2.2) --- series capacitor method (section 2.2.1), charge injection method (section 2.2.2) and their simulations (section 2.2.3 and section 2.2.4)

(3) Pull in analysis of a complicated actuator system (section 2.3) --- torsion actuators with shaped electrodes (section 2.3.2), the effect of strain stiffening on system pull in (section 2.3.3) and the effect of fringe field capacitance (section 2.3.4).

In Chapter 3, three state-of-the-art application systems are investigated: variable optical attenuators (VOA), high angular torsion mirrors for the optical cross connect

fabric (OXC), and an electrostatic tunable IR wavelength selector are designed using the methodology. Finite element analysis simulation is used to verify mirror designs. Ultra thin silicon wafer bonding technology, combined with the deep reactive etching (DRIE) process, is employed for fast prototyping of the electrostatic micro mirrors.

Finally, as a demonstration that the actuator design approach developed in this thesis can be applied to systems other than micromirrors, the approach is used to design an innovative true mass flow sensor using an electrostatic resonant beam as the sensing element. (sections 3.5.1-3.5.3).

## **CHAPTER 2**

### **DESIGN METHODOLOGY**

#### **2.1 Introduction**

In this section general capacitance-based differential equations are developed to describe the quasi-static behavior of an arbitrary electrostatic micro actuator system. The displacement and voltage parameters are then normalized with respect to their pull in values, yielding a general, unitless structural equation that valid for a wide variety of electrostatic actuators. Using this theory, a straightforward design approach is developed, and is used to model a range of simple and complex actuators to determine specified pull in solutions and actuation curves.

##### **2.1.1 A Theory for Quasi-static Descriptions of Electrostatic Micro Actuator**

Electrostatic micro actuators are those microscopic variable capacitor systems that exhibit mechanical motion in response to an applied external electrical bias source. There have been numerous articles on quasi-static modeling for many kinds of electrostatic actuators [25-31]. Usually theoretical modeling has been accomplished by balancing the elastic restoring force with the attractive electrical force to construct a structural equation and obtain a pull in solution. For example, the maximum fractional travel range before pull in is calculated to be 0.33 and 0.44 for the parallel rigid plate capacitor system and the full plate torsion actuator system, respectively [25, 26]. For the purpose of obtaining larger travel range, incorporation of a series capacitor circuit has been recently reported by Chan et al. [27]. Actuations using various electrode shapes [28] and sizes [29], and

actuators involving strain stiffening [30] and residual stresses [31] have also been investigated.

An electrostatic actuator can be modeled as a variable capacitor suspended by elastic springs as shown in Fig. 2.1. To elucidate the theory in a succinct manner, the equations are derived under the assumption that the spring stiffness matrix has only non-zero diagonal elements that are constants and independent of the actuated structure strain.

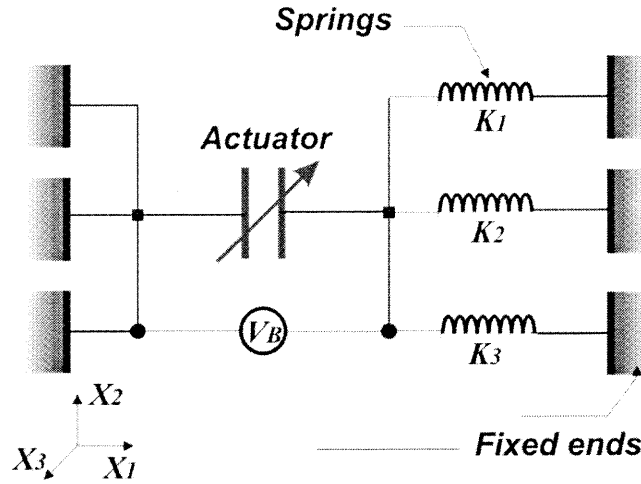


**Figure 2.1** A sketch of model of a 3D electrostatic actuator system

Applying the energy conservation law to the electro-mechanical system and differentiating with respect to displacement components,  $x(i)$ , results in a structural equation in the force domain as:

$$\frac{1}{2} V^2 \nabla C = \frac{1}{2} \left[ \frac{\partial C}{\partial x^{(i)}} \quad \frac{\partial C}{\partial x^{(j)}} \quad \frac{\partial C}{\partial x^{(k)}} \right] V^2 = \begin{bmatrix} x^{(i)} & x^{(j)} & x^{(k)} \end{bmatrix} \cdot \begin{bmatrix} K^{(i)} & 0 & 0 \\ 0 & K^{(j)} & 0 \\ 0 & 0 & K^{(k)} \end{bmatrix}, \quad (1)$$

where  $C$  is the actuator capacitance of the system, and  $K^{(i)}$  and  $x^{(i)}$  are orthogonal spring stiffness and displacement components, respectively. Multiplying by  $x^{(i)}$  on both sides of

Eq. (1) and differentiating with respect to  $x^{(i)}$ , yields the pull in equation of the structure:

$$\left[ \frac{\partial^2 C}{\partial [x^{(i)}]^2} - \frac{1}{x^{(i)}} \frac{\partial C}{\partial x^{(i)}} \right]_{x^{(i)}=x_{PIN}^{(i)}} = 0. \quad (2)$$

Hence the pull in voltage can be derived as:

$$V_{PIN}^{(i)} = \sqrt{\frac{2K^{(i)}}{\left( \frac{\partial^2 C}{\partial [x^{(i)}]^2} \right)_{x^{(i)}=x_{PIN}^{(i)}}}}. \quad (3)$$

The above three equations govern the quasi-static behavior of electrostatic micro actuators, from which displacement dependence on applied bias voltage can be obtained by Eq. (1) and pull in displacement and voltage can be obtained by Eqs. (2) and (3), respectively.

The static characteristics of an arbitrary electrostatic micro actuator are determined by the 1st and 2nd derivatives of the overall capacitance of the actuator system with respect to displacement. Therefore, the design of an actuator system is actually a design of the derivatives of the system capacitance. From the pull in equations, it can also be concluded that pull in displacement has no spring stiffness dependence, and the stiffness only contributes to the pull in voltage. This is true for actuator problems without strain stiffening and residual stress effects. Those equations are also valid for actuator systems with multiple capacitors. When using them, one needs to plug in overall capacitance instead of the single variable capacitance. The capacitance-based equations imply an electrostatic method for the purpose of large travel range actuator design, which will be addressed later in section 2.2.

In real applications, the actuator system is usually engineered to be a one degree

of freedom (1 DOF) system, so assume a 1 DOF actuator system and rewrite Eq. (1) at the pull in point as:

$$\frac{1}{2} \frac{dC}{dx} \Big|_{x_{PIN}} V_{PIN}^2 = Kx_{PIN}. \quad (4)$$

Its combination with the general structural equation cancels out spring parameters and yields a two-parameter unitless equation:

$$\Lambda \cdot U^2 = 1, \quad (5)$$

where,  $\Lambda$  is defined as  $\Lambda \left( \frac{x}{x_{PIN}} \right) = \frac{\frac{1}{x} \frac{dC}{dx}}{\left[ \frac{1}{x} \frac{dC}{dx} \right]_{x=x_{PIN}}}$ , and  $U = \frac{V}{V_{PIN}}$ .

The unitless structural equation, Eq. (5), is valid for 1 DOF electrostatic actuator systems. If an analytical approximation can be found for the capacitance, the actuation curve can be obtained using the design flow shown in Fig. 2. This enables actuator designers to obtain characteristics of an electrostatic micro actuator quickly without going through exhaustive force analysis. As an example, consider a parallel rigid plate capacitor system where the capacitance expression is simply  $C = \frac{\epsilon_0 A}{(D - x)}$ . Solving the

pull in equations leads to  $x_{PIN} = \frac{1}{3}D$  and  $V_{PIN} = \sqrt{\frac{8KD^3}{27\epsilon_0 A}}$ . Here,  $A$  is the plate area,  $D$

and  $x$  are the initial and biased gap depth, respectively, and  $K$  is the spring constant.

Defining  $X = \frac{x}{x_{PIN}}$ , the unitless electro-mechanical response equation is obtained as

$$2U = X \cdot \left( \frac{3}{\sqrt{X}} - X \right) \quad (6)$$

The two normalized parameters, voltage and displacement, are deliberately



$V_{PIN} \approx \sqrt{\frac{0.83K_{\theta}D^3}{\epsilon_0L^3W}}$ , where  $K_{\theta}$  is the torque stiffness, and  $D$ ,  $W$  and  $L$  are the initial gap depth, electrode width and length, respectively. By using the capacitance-based equation,

the specified unitless equation for this case is obtained as

$$4.48U^2 = \Theta^3 \left[ \frac{0.44\Theta}{1-0.44\Theta} + \ln(1-0.44\Theta) \right]^{-1}, \text{ which agrees with the normalized equation}$$

first introduced by the force analysis method [32]. Again this characteristic equation should be the same for all pure torsion actuators, as shown in Fig. 2.3, which compares torsion actuators with various actuation schemes.

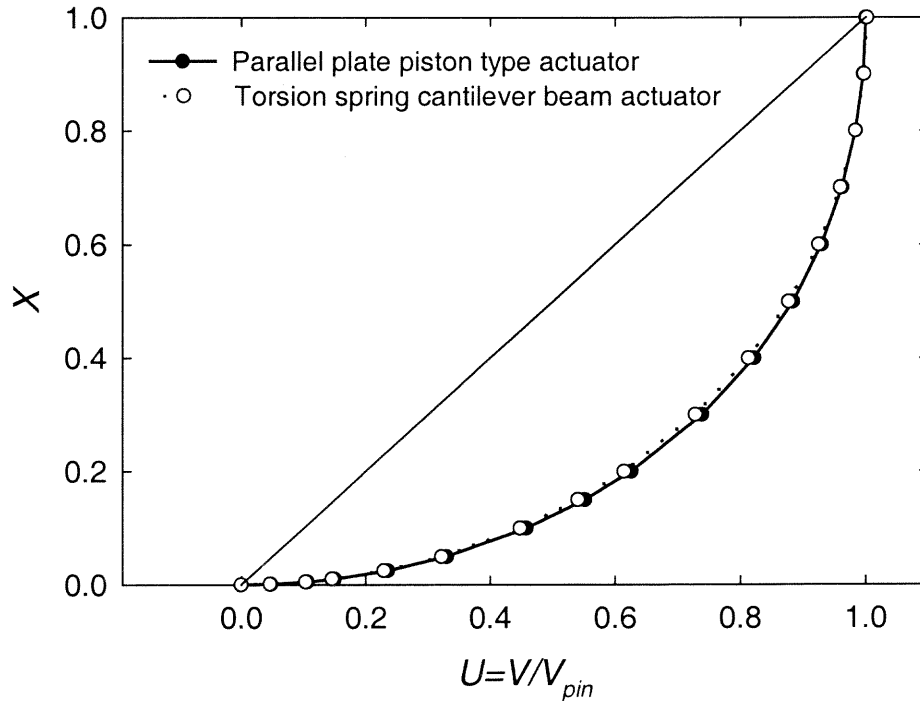


**Figure 2.3** Characteristic actuation equation of pure torsion actuators and parallel plate actuators.



It should be noted that the capacitance-based equations and the force-balanced equations are principally the same in physics. Both approaches represent the law of conservation of energy. The advantage in using the capacitance-based approach is that it avoids the complicated force analysis and is most suitable for the analysis of complex microactuator systems in which the usual force analysis is not straightforward. To demonstrate its usage, a beam that is suspended by torsion springs at four ends and has a rigid boss at the center, is simplified; and the pull in dependence on the length ratio of the two capacitor types is solved. As shown schematically in Fig. 2.4, the movable electrode plate of the actuator is suspended by a set of serpentine torsion springs, and undergoes quasi-rigid deflection during electrostatic actuation.

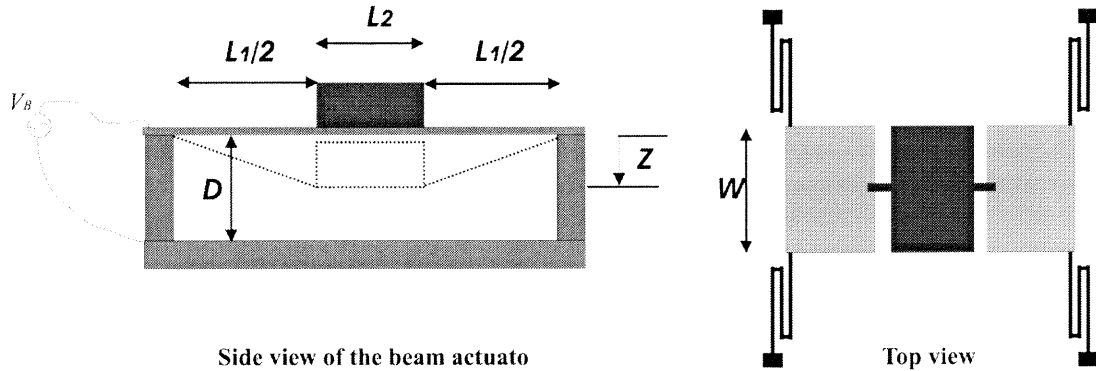


**Figure 2.4** The schematic of a torsion actuator with a rigid center boss. The boss is viewed as a rigid body during actuation and the rotational sections are viewed as wedge-shaped for small gap and displacement.

The two edge sections are assumed to have a wedge-shaped contour, with capacitance that is given as  $C_1 = \frac{\epsilon_0 W L_1}{z} \ln \frac{D}{D-z}$ . By adding the center parallel plate

capacitor  $C_2 = \frac{\epsilon_0 W L_2}{D-z}$ , the overall capacitance of the actuator system is:

$$C = \frac{\epsilon_0 W L_1}{z} \ln \frac{D}{D-z} + \frac{\epsilon_0 W L_2}{D-z}, \quad (7)$$

where  $z$  is the center deflection of the beam,  $D$  is initial gap, and  $W$  and  $L_1, L_2$  are the beam width and length parameters, respectively. The pull in displacement is found to be between 0.33 and 0.44 of the initial gap depth  $D$ , depending on the two length parameters  $L_1$  and  $L_2$ , ( $L=L_1+L_2$ ) as shown in Fig. 2.5.

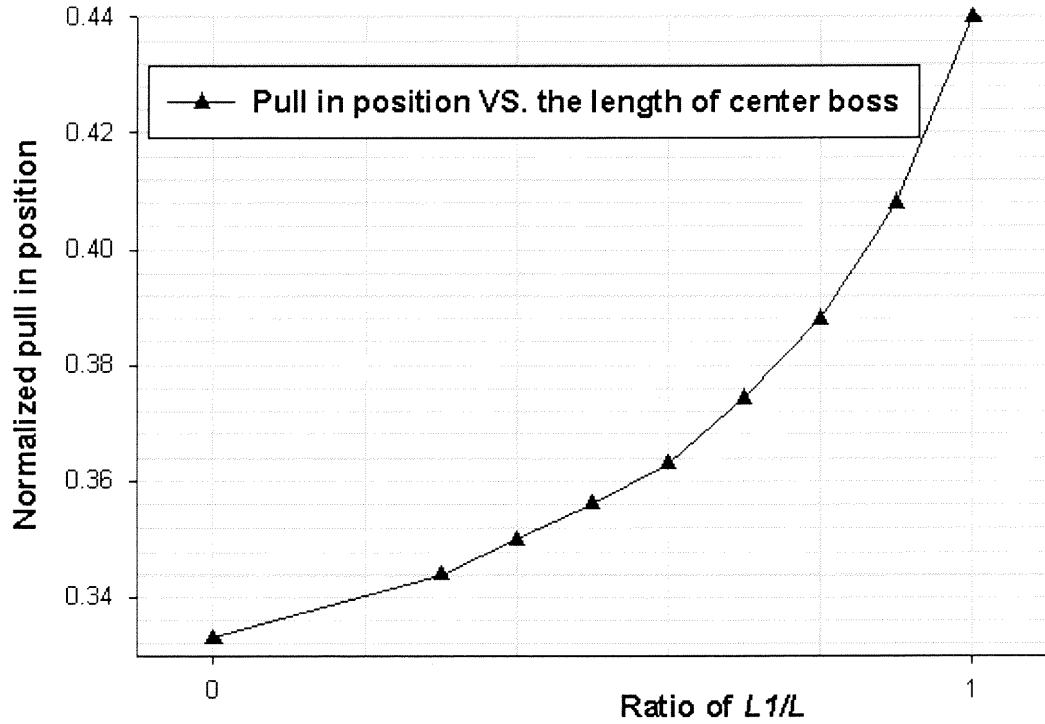


**Figure 2.5** Pull in dependence on the length ratio of a wedge-shape capacitor with center boss.

This capacitance-based analytical approach is very suitable for actuator systems with multiple capacitor elements for which the designer should plug in overall capacitance. For example, in the analysis of the series capacitor method for extending travel range in the electrostatic domain, the overall capacitance satisfies the relation  $C^{-1} = C_a^{-1} + C_s^{-1}$ , where  $\alpha$  is the capacitance ratio at zero bias. For the case of a

constant series capacitor, the characteristic equation is also the same because the system is identical to the single capacitor system with a modified initial gap depth. If the series capacitor is also a variable parallel plate capacitor, then the unitless actuation equation of the system will also take the same form as that of a single parallel plate capacitor system. The two separate actuation equations are added directly.

The equations and methods can be applied to handle complex actuator systems with various electrode shapes and sizes, systems with non-negligible fringing field effects, and systems with built-in spring stiffening, since all the derivations after using the modified overall capacitance and stiffness expressions still hold. These issues will be addressed in later sections.

### **2.1.2 Actuator Classification and Quasi-static Design Methodology**

The design methodology presented in this dissertation is based on the pull in theory which says that a threshold point exists in any electrostatic actuator system before which motion of the system is continuous and can maintain a stable equilibrium. Beyond this point, there is no stable equilibrium. The design methodology assumes the general fact that electrostatic actuators can be specified by mechanical boundary conditions which, in combination with the electrode design, will solely determine the pull in condition. A common list of such actuators includes:

- A. 1-D parallel rigid plate actuator
- B. Pure torsion rigid cantilever actuator
- C. Deformable cantilever actuator
- D. Double-clamped deformable beam actuator

### E. Clamped deformable membrane actuator

If variations of electrode configuration and material elastic properties are considered, this summary list would be sufficient to cover almost all actuators that have been used to realize micro mirror system in the MEMS community, with comb drive actuators as an exception. Variations in the electrode configuration include projection factor (electrode fill factor from partial to full), electrode shape factor and fringing field effects. Variations in material properties include strain stiffening. These possible actuator variations are summarized in Fig. 2.6.

The multiple actuator types and variations make engineering design difficult if any particular device design has to go through analysis separately. Fortunately, pull in positions of these actuator types and variations have certain constant values through which a design methodology can be derived. The design methodology normalizes the actuation curve by comparing arbitrary displacement and corresponding voltage during operation with the displacement and voltage at pull in. The two unitless variables, one for displacement and one for actuation voltage, form a unique characteristic function for each

actuator type. For example, starting from capacitance  $C = \frac{\epsilon_0 A}{L\theta} \ln \frac{D}{D - L\theta}$  for a full-plate, rectangular, pure torsion actuator, the unitless characteristic function is derived as

$$4.48U^2 = \Theta^3 \left[ \frac{0.44\Theta}{1 - 0.44\Theta} + \ln(1 - 0.44\Theta) \right]^{-1}. \text{ Here, the normalized displacement and}$$

voltage parameters  $\Theta$  and  $U$  are used, where  $\Theta$  and  $U$  are the ratio of deflection angle and voltage over the pull in values. The pull in values are found to be

$$\theta_{PIN} \approx 0.44 \cdot \tan^{-1}(D/L) \text{ and } V_{PIN} \approx \sqrt{\frac{0.83K_\theta D^3}{\epsilon_0 L^3 W}}, \text{ respectively. } K_\theta \text{ is the torque}$$

stiffness, and  $D$ ,  $W$  and  $L$  are the initial gap depth, electrode width and electrode length, respectively.

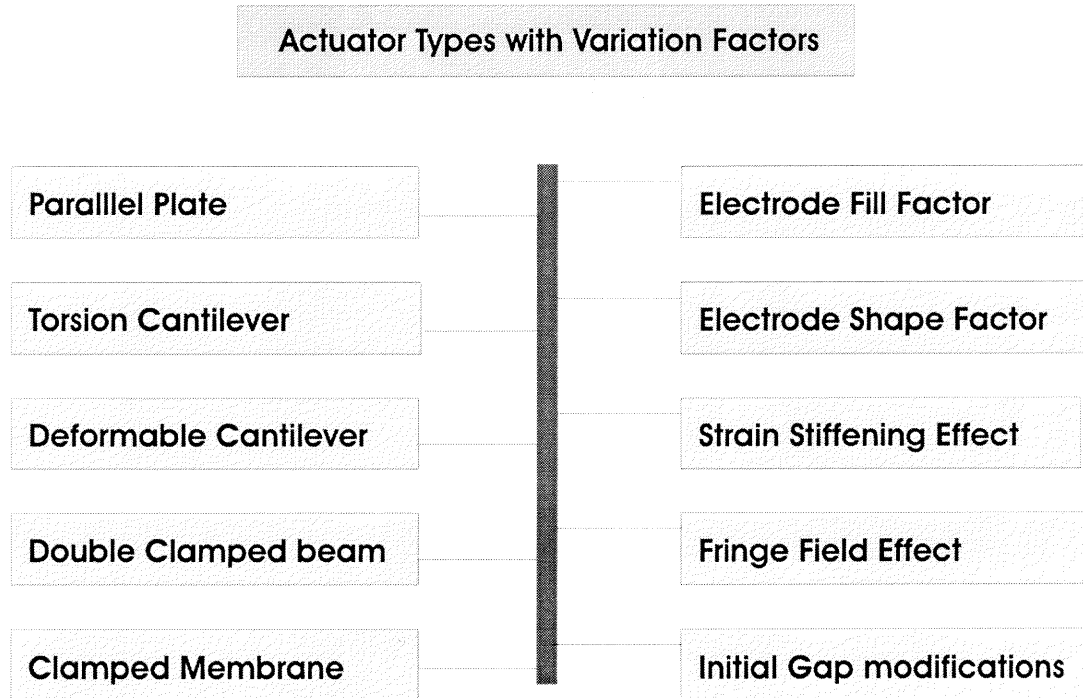


**Figure 2.6** Detailed actuator list with variation factors. Each line links to the center bar representing an actuator type with one variation factor.

Referring to Fig. 2.6, although a real system would have all kinds of variation factors, a practical design guide in engineering is to approximate the system with acceptable accuracy. Reasonable simplification is always possible for a real system. For example, for the 1D parallel plate system, one can conveniently ignore the strain stiffening and residual stress effects to get only three variations: fill factor, fringing fields and shaped electrodes. Furthermore, if the gap is narrow compared to the plate lateral dimensions, one can also exclude fringing field effects. In this simple system, notice that

the shaped electrode factor can be addressed as fill factor, so only electrode area and spatial symmetry count. The latter is usually necessary to maintain a true parallel plate actuation. The parallel plate system is the simplest and most useful actuator type that has been implemented by MEMS researchers. Practical actuators that have been presented in current real applications include:

Case 1: Full plate actuated parallel plate system

Case 2: Rectangular torsion cantilever actuators with fill factor

Case 3: Torsion actuators with shaped electrodes

Case 4: Deformable cantilever beam with fill factor and shaped electrodes

Case 5: Double clamped beam with strain stiffening and residual stress effect

Case 6: Clamped membrane with residual stress effects

Actuators 1-3 are rigid plate actuators, the other three actuators employ deformable continuums. For rigid plate actuators with small amplitude displacement, the system capacitance is usually independent of spring stiffness. In Fig. 2.7 a down stream design flow is presented for actuator system where the capacitance and spring constant are not coupled. In these systems the capacitance function has only spatial dependence and does not explicitly contain spring parameters. In other words the strain stiffening and residual stress effects are excluded. Usually for rigid plate systems and systems with small-amplitude displacements and minimized thermal mismatch between materials, this uncoupled model provides a good approximation. As mentioned above, the quasi-static investigation provided in this dissertation is targeted for the purpose of engineering reference at acceptable accuracy.

In this design flow, the displacement contour of the movable electrode is first used to obtain the capacitance expression, and material elasticity and device dimensions are used to obtain the spring constant. Next, the capacitance expression is plugged into the pull in position equation to obtain the pull in displacement  $X_{pin}$ .  $X_{pin}$  is then input into the pull in voltage expression together with the spring constant to acquire the pull in voltage. Stable operation values are then expressed as ratios over pull in values. Finally, after normalizing the voltage and displacement data, a general actuation equation is determined in step 5. A different equation is expected for each actuator type.

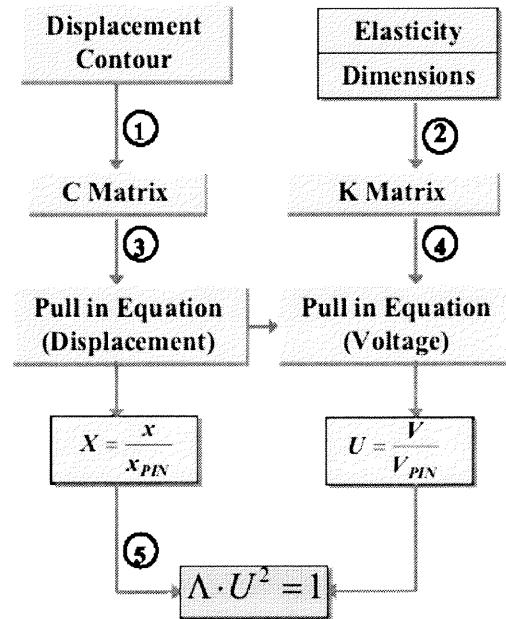


**Figure 2.7** A stream down flow illustrating the pull-in based design method.

As shown in Fig. 2.7, the actuator designer should follow the design flow in reverse to extract actuator parameters at a physics level. The following sections introduce analytical results for non-deformable actuator systems.

### 2.1.3 Pull in Studies of Non-Deformable Torsion Actuator Systems

In this section emphasis is put on pull in solutions of non-deformable actuator systems. The study of pull in is important not only because it reveals the allowable stable operation region, but also because it provides useful information for actuator optimization, for example to increase the efficiency of the applied drive voltage. The pull in analysis also provides the preliminary information required to use the static design method.

#### 2.1.3.1 Series Connected System with Multiple Variable Parallel Plate Capacitors

Consider the series connection of parallel plate capacitors  $C_1$  and  $C_2$ . Mechanically the movable plates with area  $A_1$  and  $A_2$  are suspended by two independent springs  $K_1$  and  $K_2$ , respectively. Two displacement variables are involved,  $X_1$  and  $X_2$ . Assuming identical initial gap depth  $D$ , the system overall capacitance is written as:

$$C = \frac{C_1 \cdot C_2}{C_1 + C_2} = \epsilon_0 \left[ \frac{A_1}{D - X_1} \cdot \frac{A_2}{D - X_2} \right] / \left[ \frac{A_1}{D - X_1} + \frac{A_2}{D - X_2} \right]$$

It can be rewritten in single parallel plate form by inserting an arbitrary area factor  $A$ .

$$C = \frac{\epsilon_0 A}{D \left( \frac{A}{A_1} + \frac{A}{A_2} \right) - \left( \frac{A}{A_1} X_1 + \frac{A}{A_2} X_2 \right)}$$

Therefore the system pull in occurs at

$$\left( \frac{X_1}{A_1} + \frac{X_2}{A_2} \right)_{PIN} = \frac{D}{3} \left( \frac{1}{A_1} + \frac{1}{A_2} \right).$$



In the case of  $A_1=A_2$ , this equation becomes  $(X_1 + X_2)_{PIN} = \frac{2D}{3}$ , which suggests a travel range extension approach. To increase the stable operation region of  $C_1$ , for example, if  $K_1=K_2$  and capacitor  $C_2$  is fixed, then  $X_2=0$  leads to pull-in position of  $C_1$  at  $X_1=2D/3$ . If  $A_1=2A_2$ , then  $X_2=0$  leads to  $X_1=D$  for  $C_1$  capacitor, i.e., full gap stable operation for  $C_1$ . Fig. 2.8 is a schematic view of a series connected capacitor network with one capacitor fixed.

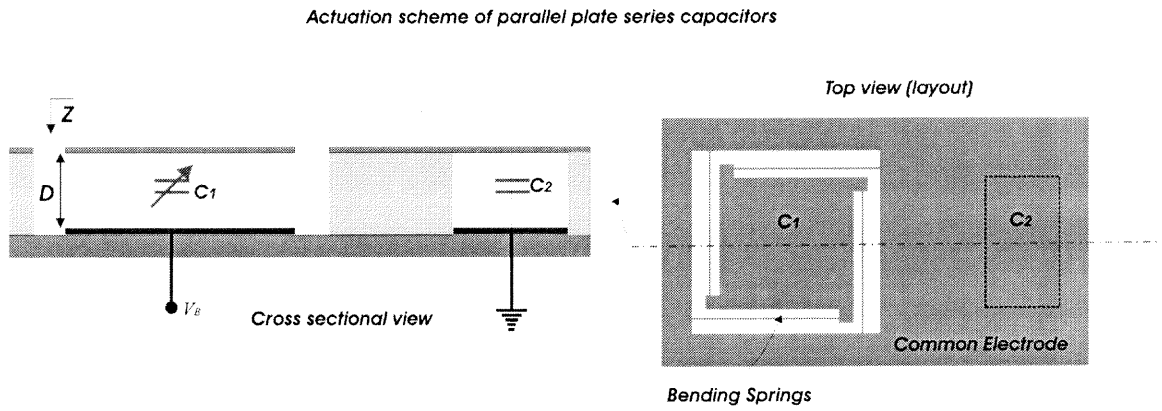


**Figure 2.8** Schematic view of a series connected capacitor network with one capacitor fixed.

**2.1.3.2 Rectangular Torsion Actuators with Partial Electrodes.** As shown in Fig. 2.9,  $L_1$  and  $L$  are the lengths of the electrode and the proof mass, respectively. If the electrode is located at the edge away from the spring, the capacitance is given by

$$C = \int_0^{L_1} \frac{\epsilon_0 W dx}{D - (L - L_1)\theta - x\theta} = \frac{\epsilon_0 W}{\theta} \ln \left[ \frac{D - (1 - r)L\theta}{D - L\theta} \right].$$

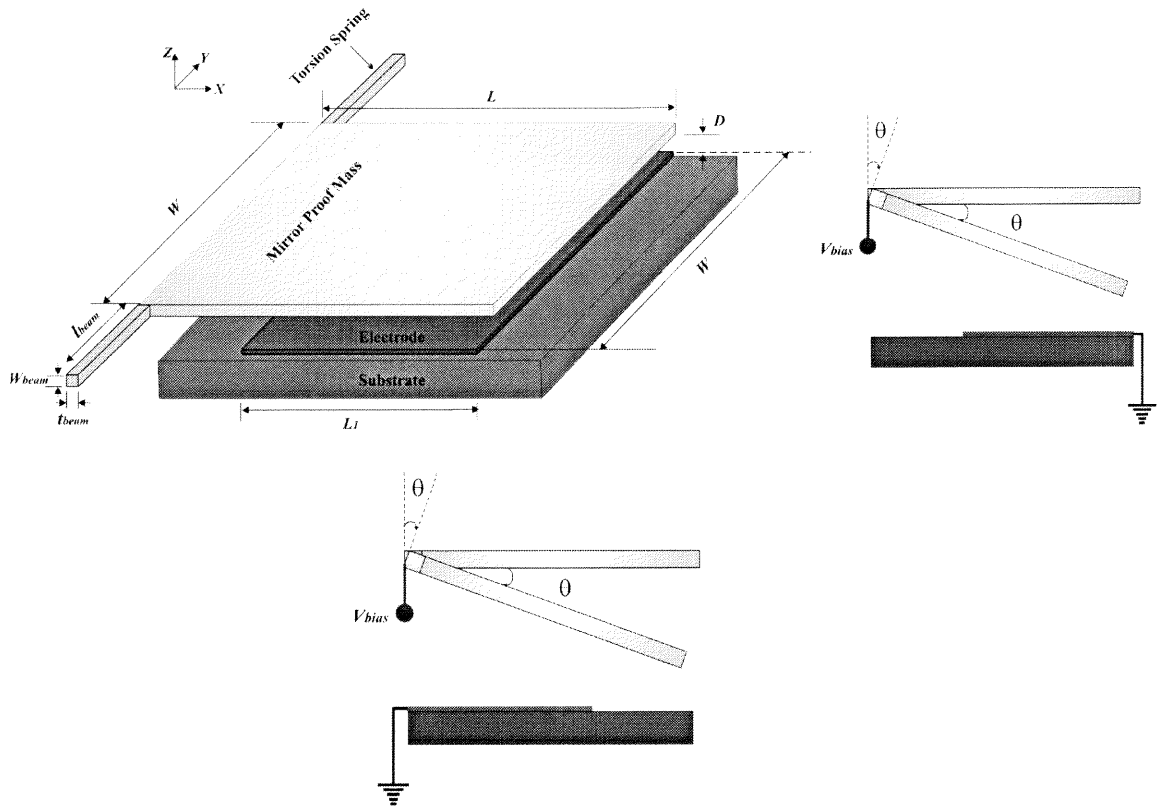
It can be shown that as the electrode length ratio  $\gamma$  ( $\gamma = L_1/L$ ) decreases from 1.0 to 0.1,  $\theta$  decreases from 44% to 33%, as shown in Fig. 2.10. This is not surprising since as the ratio  $\gamma$  decreases, the configuration is more like a simple parallel plate. The actuation curves are all identical while  $\gamma$  changes from 0.1 to 1.0.

If the electrode is located at the edge close to the spring, the capacitance becomes

$$C = \int_0^{L_1} \frac{\epsilon_0 b dx}{D - x\theta} = \frac{\epsilon_0 b}{\theta} \ln \frac{D}{D - rL\theta}$$

Taking the fill factor  $\gamma$  as a state variable leads to relationship  $\gamma \bullet \Theta = 0.44$ . The full-gap travel range can be obtained by reducing the electrode length to  $0.44L$  or less. As for the characteristic function, it should be the same for all rigid pure torsion actuators since the structural equation is normalized to be unit-less.

Partial Actuation Scheme with Electrode at far end from springs



Partial Actuation Scheme with Electrode at near end from springs

**Figure 2.9** The schematics of torsion mirrors with far-spring-end and near-spring-end electrode actuations, respectively.

**2.1.3.3 Torsion Actuators with Elliptic-Shape Electrodes.** The elliptical electrode actuation scheme is schematically illustrated also as Fig. 2.9, except that the electrode should take the shape of a half ellipse, as shown in Fig. 2.11. The capacitance integral of the system is given as

$$C = 2\varepsilon \int_0^a \frac{y dx}{d - x\theta} = 2\varepsilon \int_{\pi/2}^0 \frac{b \sin t (-a \sin t) dt}{d - a \cos t \cdot \theta} = 2\varepsilon \int_0^{\pi/2} \frac{ab \sin^2 t}{d - a\theta \cos t} dt$$

where  $a$  and  $b$  are semi major axis and semi minor axis, respectively and  $t \in (-\pi/2, \pi/2)$ .

The resulting capacitance is

$$C = \left( 2b\varepsilon \left( (0.5d\pi + a\theta)\sqrt{-d^2 + a^2\theta^2} + (2d^2 - 2a^2\theta^2) \text{ArcTanh} \left[ \frac{d + a\theta}{\sqrt{-d^2 + a^2\theta^2}} \right] \right) \right) / (a\theta^2 \sqrt{-d^2 + a^2\theta^2})$$

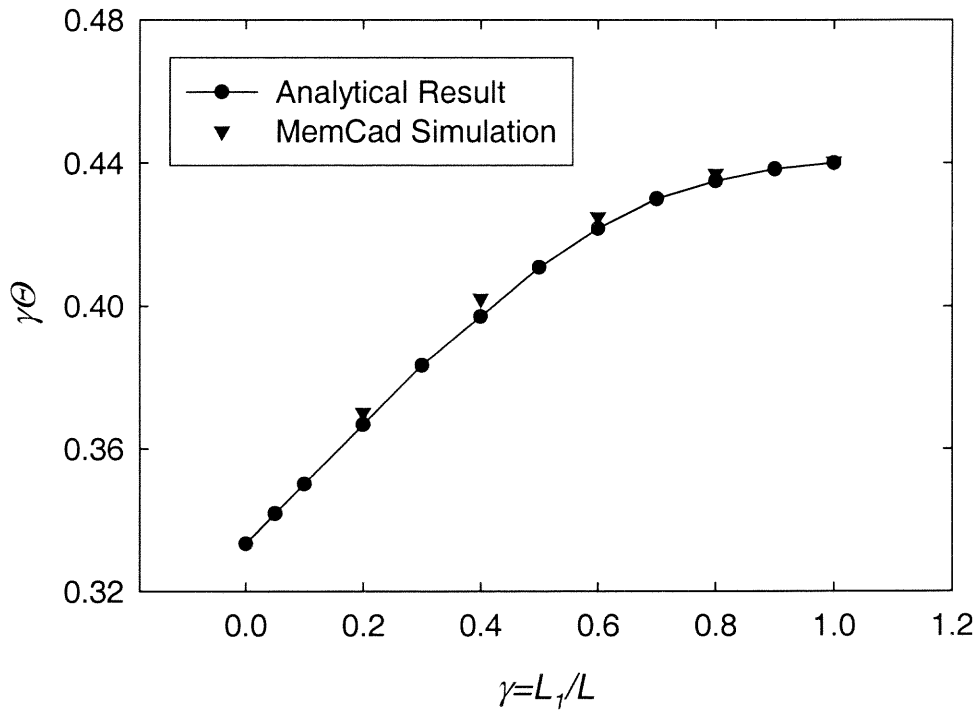


**Figure 2.10** Analytical unitless pull-in position  $\theta$  of a cantilever rectangular torsion actuator with electrode located at the far-end from torsion springs.

For full plate elliptical electrodes (where  $a=L$ ),  $\theta$  is 0.4833, independent of the semi-major axis  $a$  and semi-minor axis  $b$ , as shown in Fig. 2.12. A special case is actuation with a full circular shape electrode in which  $a$  is equal to  $b$ . In this case the pull-in position is 0.4833.

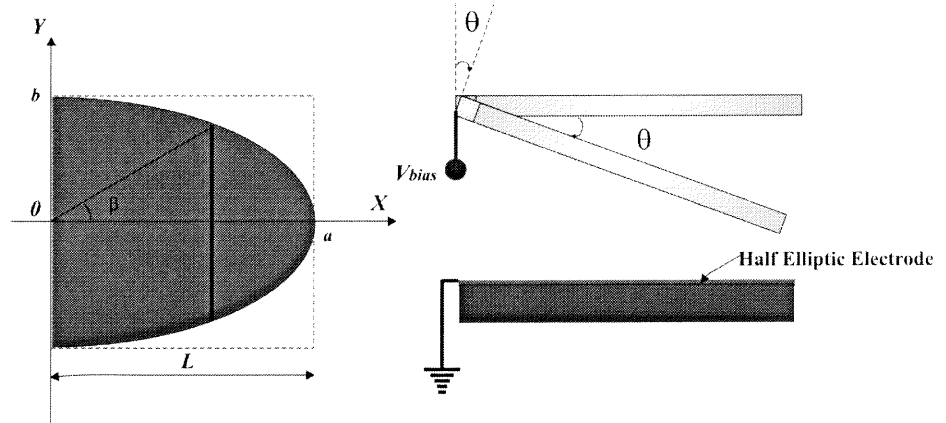


**Figure 2.11** Layout and cross section views of full elliptic-electrode-actuated torsion actuator.

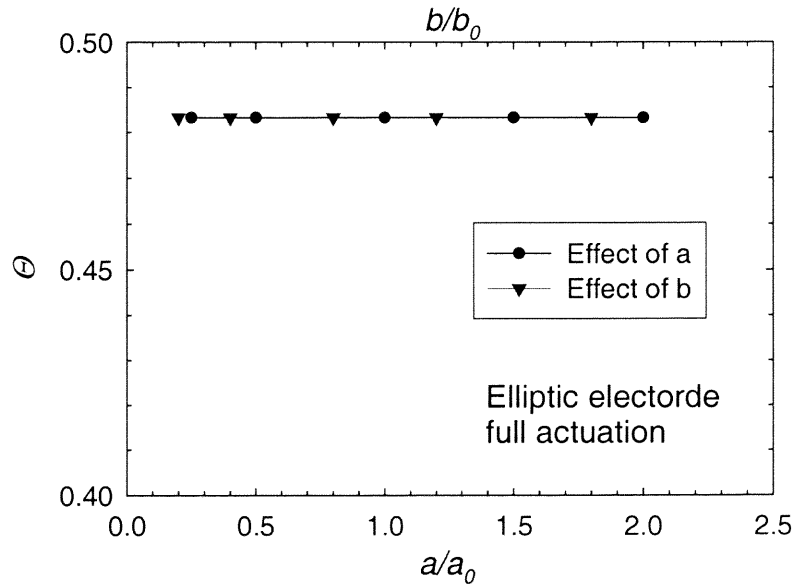


**Figure 2.12** Effect of semimajor and semiminor axes  $a$  and  $b$  on unitless pull in position  $\theta$  of full elliptic electrode actuation.

In summary, the simple capacitance-based equations have been applied to various complex actuator systems to analytically acquire quasi-static solutions. Although principally one can obtain the solutions also by using the traditional force balanced method, the complexity of the required field and force analysis makes the task very challenging.

## 2.2 Travel Range Extension Methods

### 2.2.1 Introduction

Large travel range is especially important in emerging optical micro mirror and variable capacitor applications. In theory, the maximum travel range before pull in is 33.33% for full-plate vertical out-of-plane electrostatic actuators and 44.04% for torsion electrostatic actuators [33]. Generally, in order to extend an actuator's travel range before snap down, a negative feedback mechanism is required. *Mechanical* approaches such as leveraged bending and strain stiffening have been examined previously [30]. The two methods described here introduce negative feedback and extend the travel range directly in the *electrostatic* domain. These methods are passive in that no external closed loop feedback control is employed.

The first method utilizes a series capacitor to modulate the effective actuation voltage across the variable capacitor. The resulting voltage across the actuator exhibits a maximum value at a specific applied bias, beyond which it begins to drop even though the charge density keeps increasing to give an increased electrostatic torque. The effect of this decreasing voltage is to delay the increase of electrostatic torque so that the restoring

elastic torque can balance it at an expanded travel range. Two typical micro mirror structures: out-of-plane vertical and torsion mirrors, are used to verify this concept. In this section the mathematical analysis of the series capacitor loop model will be first presented, then simulation results obtained using the CoSolver feature of Memcad<sup>TM</sup> software are compared with analytical results with good agreement.

The second method utilizes negative feedback due to coulombic repulsion between the net oxide charges that exist in two oxide layers placed between the actuator electrodes. The net oxide charge is modeled to be immobile and located within 25Å of the Si-SiO<sub>2</sub> interface, without electrical communication with the Si. The C-V characteristics of the fabricated torsion mirror structure show a negative net oxide charge density of magnitude  $10^{10-12}/\text{cm}^2$ . The repulsive interaction will occur significantly when oxides layers are in close proximity (e.g.  $d=6.96\mu\text{m}$  for our example device). In addition, the fixed charge density is comparable to the surface charge density ( $10^{9-12}/\text{cm}^2$ ) due to applied bias voltage from 1V to 200V for our prototype device. Therefore an extra repulsive electrostatic torque is superimposed on the attractive electrostatic torque to retard the increasing rate of the total electrostatic torque in such a manner that a negative feedback mechanism is introduced into the actuator structure that enables the elastic torque of the spring structure to balance the electrostatic torque at an expanded travel range up to 62% of full scale deflection. This increased travel range occurs at the expense of an increased bias voltage. It should be mentioned that the oxide layers also serve as a voltage divider in the prototype structure, but this effect is not dominant due to its comparatively larger capacitance value.

### 2.2.2 Series capacitor method

As modeled in Fig. 2.13, the first method utilizes an integrated fixed series capacitor as a voltage divider to modulate the effective voltage across the variable capacitor/actuator. Applying Newton's second law to the 1-D actuator system gives the structural equation. Differentiating with respect to  $x$ , multiplying by  $x$  and subtracting equation 1 (see Section 2.1.1) gives the pull-in equation.

$$\frac{1}{2} \frac{dC}{dx} V^2 = Kx$$

$$\frac{d^2 C}{dx^2 x_{PIN}} - \frac{1}{x_{PIN}} \frac{dC}{dx} = 0$$

where  $C$  is the overall capacitance of the actuator system and  $K$  and  $x$  are the generalized spring stiffness and the change of generalized displacement, respectively.

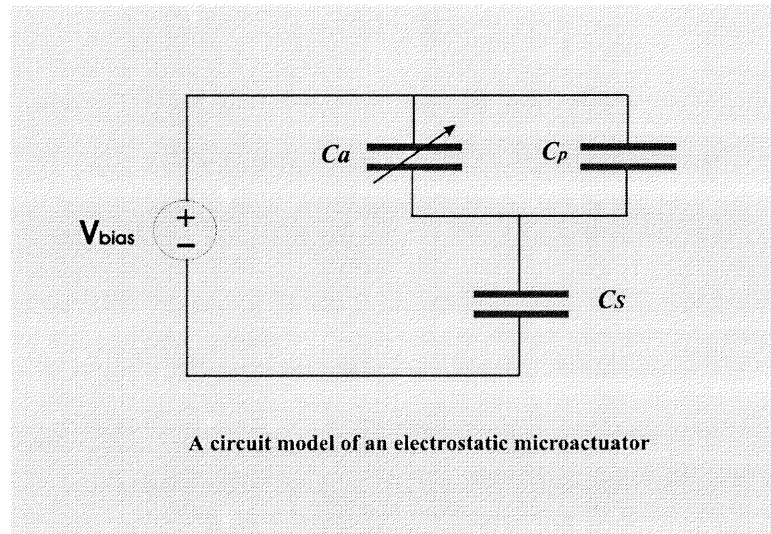


**Figure 2.13** Circuit of Series Capacitor Loop

The static characteristics of an arbitrary electrostatic micro actuator are determined by the 1<sup>st</sup> and 2<sup>nd</sup> derivatives of the overall capacitance of the actuator system

with respect to  $x$ , and the design of an actuator system is simply the design of its overall capacitance. For most applications, there are analytical expressions or empirical approximations for the overall capacitance that enable designers to obtain quick characteristics for the static behavior of an electrostatic micro actuator by utilizing the above equations. Now address the obtainable large travel range for two popular electrostatic micro mirror structures.

### Vertical Z Actuator

In the vertical Z actuator, the movable plate is rigid and suspended by a folded spring structure. Assume that no deformation occurs on the movable electrode plate during actuation as illustrated in Fig. 2.8, and consider the case of full plate actuation.

Referring to Fig. 2.8, and defining the capacitance ratio  $\alpha = C_{a0}/C_s$  (where  $C_{a0}$  is  $C_a$  at  $x=0$ ), then  $C_s$  takes the form:  $C_s = \alpha^{-1}C_{a0} = \alpha^{-1}(\epsilon_0 A/D)$ . Considering this integrated capacitance, the net capacitance of the actuator system satisfies the relation  $C^{-1} = C_a^{-1} + C_s^{-1}$ . The overall capacitance  $C$  can be shown to be:

$$C = \frac{\epsilon_0 A}{(1 + \alpha)D - x}$$

Plugging the 1<sup>st</sup> and 2<sup>nd</sup> derivatives of the expression into Eq. 2, the structural and pull in equations are obtained as:

$$\frac{\epsilon_0 A V^2}{2[(1 + \alpha)D - x]^2} = Kx$$

$$\frac{2}{[(1 + \alpha)D - x_{PIN}]} - \frac{1}{x_{PIN}} = 0$$



The travel range is solved to be:

$$TR = \frac{x_{PIN}}{D} = \frac{1}{3}(1 + \alpha)$$

Thus, the effect of the incorporated capacitance is equivalent to a gap depth extension from  $D$  to  $(1 + \alpha)D$ . The travel range of the new system becomes  $1/3$  multiplied by  $(1 + \alpha)$ , always larger than that of a single capacitor system for  $\alpha \neq 0$ . A ratio  $\alpha = 2$  leads to 100% gap depth travel range, where the series capacitance is equal to half of the zero deflection  $C_{a0}$  value.

The corresponding pull in voltage is obtained as:

$$V_{PIN} = \sqrt{\frac{8KD^3}{27\epsilon_0 A}(1 + \alpha)^3}$$

The equation indicates that the increased travel range is obtained at a sacrifice of actuation voltage by a factor of  $(1 + \alpha)^{3/2}$ . At  $\alpha = 0$  the well-known  $1/3$  travel range is obtained for a single capacitor vertical z-actuator.

### Cantilever Torsion Actuator

For the wedge shaped capacitance of the actuator shown schematically in Fig. 2.11 and considering the single active wedge-like capacitance:

$$C_a = \frac{\epsilon_0 W}{\theta} \ln \frac{D}{D - L\theta}$$

where  $W$  and  $L$  are the mirror width and length respectively,  $D$  is the initial gap depth and  $\theta$  is the angle of tilt under bias voltage. In this system the introduction of a series capacitor leads to the ratio  $\alpha(\theta)$  such that  $[\alpha(\theta)^{-1} - 1] = C_a(\theta)/C_s$ . The overall capacitance  $C$  of the torsion actuator system can be easily expressed as:  $C = C_a(\theta) \cdot \alpha(\theta)$ . For this system, the structural and pull-in equations become:

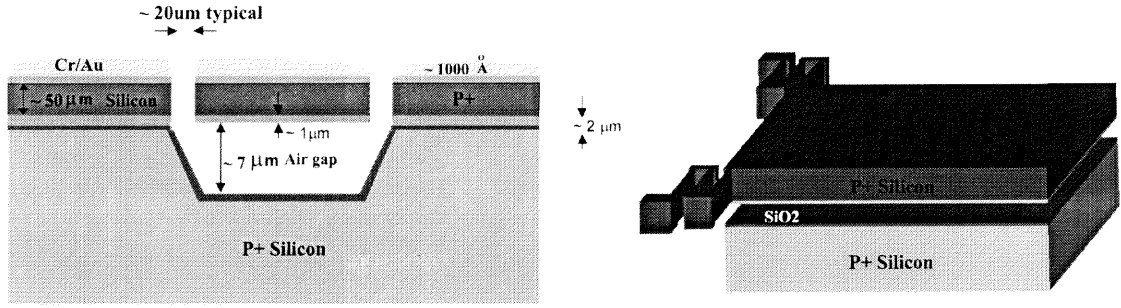


**Figure 2.14** Torsion Micro Mirror with Oxides

$$\frac{1}{2}(C'_a\alpha + C_a\alpha')V^2 = K_\theta\theta$$

$$\left[ (C''_a\alpha + 2C'_a\alpha' + C_a\alpha'') - \frac{1}{\theta}(C'_a\alpha + C_a\alpha') \right]_{\theta_{PIN}} = 0$$

The complexity of the capacitance expression requires numerical iteration in order to solve the equations. Section 2.2.5 will provide a comparison between these solutions and FEA simulation results. It can be shown that for the example device NC3 (in Section 2.2.4), the travel range increases up to 70% of the full scale.

### 2.2.3 Charge injection method

Many research results support the existence of fixed oxide charge [52, 53]: It is positive, immobile, and is located within 25Å from the Si-SiO<sub>2</sub> interface and does not communicate electrically with the Si. In electrostatic actuators where positive charge is incorporated in an oxide layer on each electrode, a significant repulsive interaction will occur when both oxides are closely spaced and when the fixed charge density is of the same order as the capacitance charge. A typical fixed charge density (10<sup>10-12</sup>/cm<sup>2</sup>) is comparable to the surface charge density (10<sup>9-12</sup>/cm<sup>2</sup>) due to applied bias voltage from 1V to 200V in the devices discussed in later sections. The operation of an electrostatic torque

modulator is based on the simple principle of Coulomb's repulsive force due to the two positive fixed oxide charge sheets near the Si-SiO<sub>2</sub> interfaces. An extra repulsive electrostatic torque is superimposed on the voltage-induced attractive electrostatic torque, retarding the increasing rate of the total electrostatic torque in a manner that a negative feedback mechanism is introduced into the actuator structure. The electrostatic attractive torque becomes less sensitive to bias voltage increases, and the delayed electrostatic torque enables the elastic torque of spring structure to balance the electrostatic torque at an expanded large deflection angle, up to 70% of the full-scale angle at the expense of an extra bias voltage.

For the torsion actuator of Fig. 2.14, the structural equation is:

$$M^{(A)}(\theta) - M^{(R)}(\theta) = K_\theta \theta$$

$M^{(A)}(\theta)$  and  $M^{(R)}(\theta)$  are the electrostatic attractive and repulsive torques respectively. The pull-in angle and bias voltage are determined by solving the equation:

$$\left( \theta \cdot \frac{dM^{(A)}(\theta)}{d\theta} - M^{(A)}(\theta) \right) - \left( \theta \cdot \frac{dM^{(R)}(\theta)}{d\theta} - M^{(R)}(\theta) \right) = 0$$

Numerical approximation by expansion techniques and FEA simulation can be used to find the solutions for the equations.

## 2.2.4 Simulation and calculation of series capacitor method

### Vertical Z Actuator

For vertical bending actuators, as shown in Fig 2.15, the resultant voltage across the actuator exhibits a maximum value at a specific applied bias, beyond which it begins to drop. It can be seen from this calculation that the maximum effective voltage occurs exactly at the original pull in position if no series capacitor were present. Although the

charge density on the movable plate always increases with the bias voltage, the voltage across the air gap does not increase beyond the maximum value because of the rapid capacitance increase of the variable capacitor.

The effect of this decreasing voltage is to delay the increase of electrostatic torque so that the restoring elastic torque can balance it at an expanded travel range. Numerical analysis shows that at the expense of increased applied voltage, the series capacitor can expand the travel range to 100% full scale for out-of-plane, vertical, full-plate, microactuators. The extended travel range (vertical (VC1) devices) is illustrated in Fig 2.16, showing the travel range extension results for different ratios of the series to initial actuator capacitance.

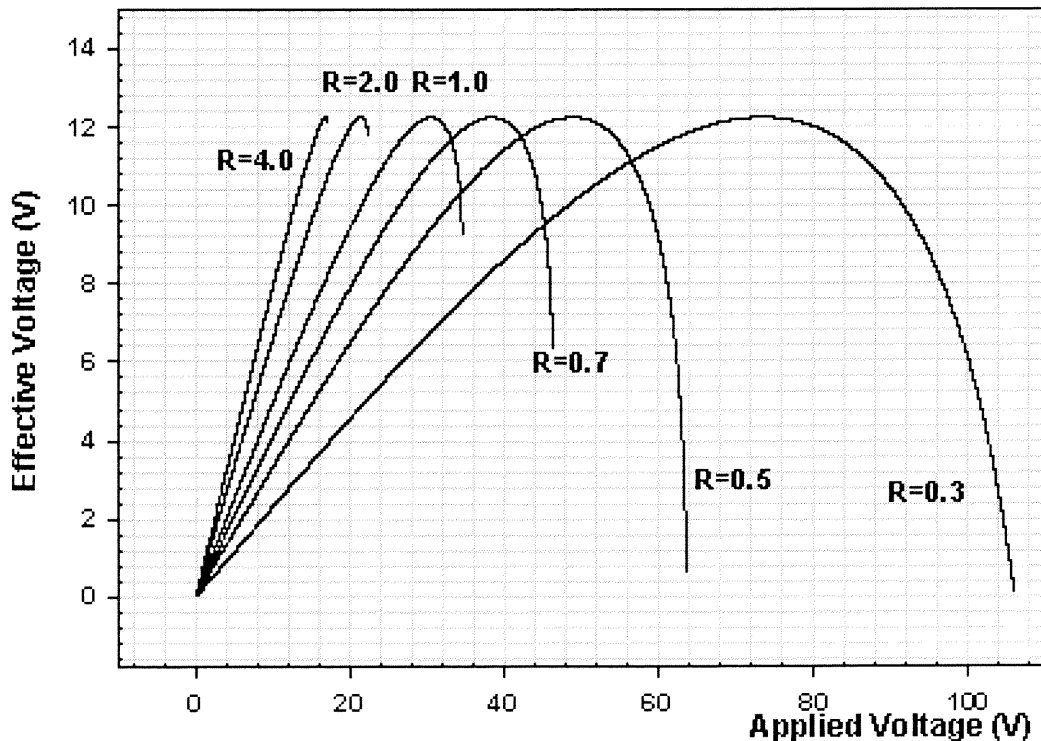


**Figure 2.15** Effective Actuation Voltage vs. Applied Bias Voltage for Different Capacitance Ratio ( $R=C_s/C_{ao}$ ) for a Vertical Z Actuator.

In Fig. 2.16,  $R$  is the reciprocal of the pre-defined capacitance ratio  $\alpha$ . The

theoretical analysis results agree very well with simulated results. If  $R$  is chosen to be smaller than 0.5, then full-scale travel range can be achieved.

### Cantilever Torsion Actuator

A torsion mirror (NC3) as illustrated in Fig. 2.17, neglecting the effects of oxides, is simulated with different capacitance ratios. Fig. 2.17 shows the comparison of iteration and simulation results, where  $R$  is equal to  $C_s/C_{a0}$ . These results are found to be in good agreement.

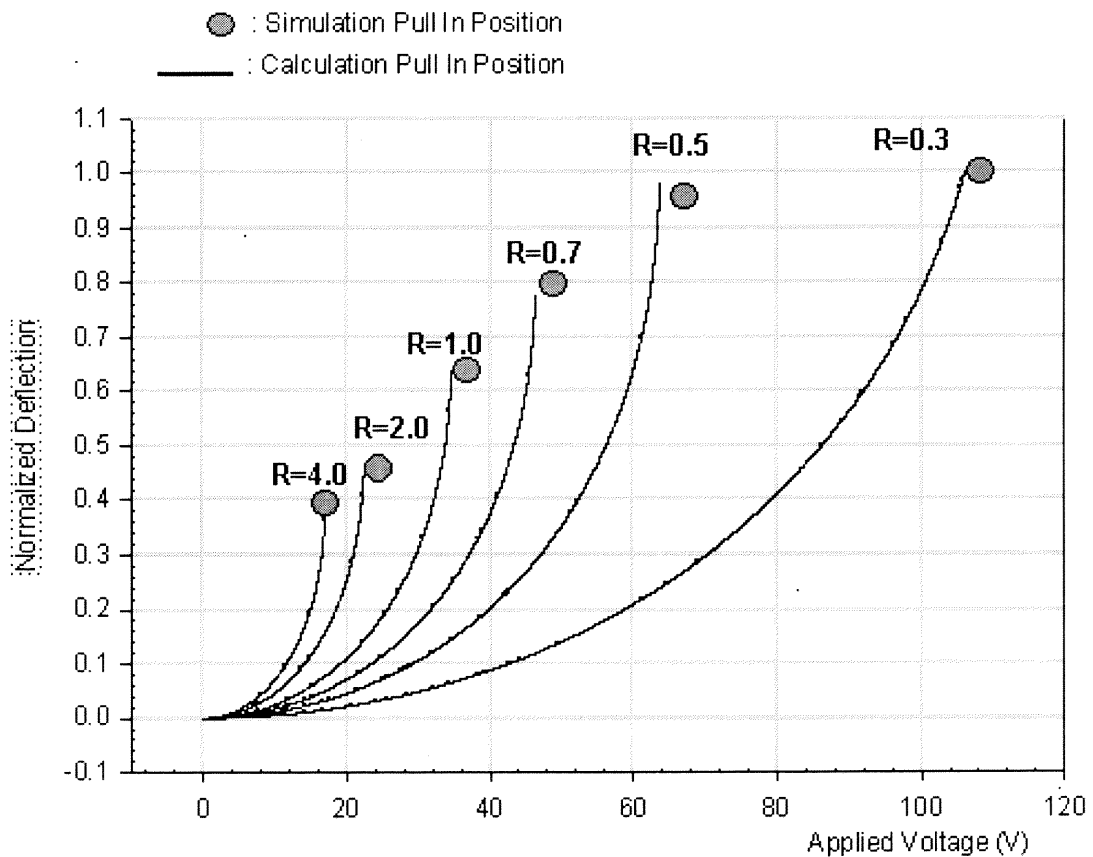


**Figure 2.16** Normalized Deflection vs. Applied Voltage for Different Capacitance Ratios. Vertical Z Actuator VC1 with Gap Depth=4 $\mu$ m.

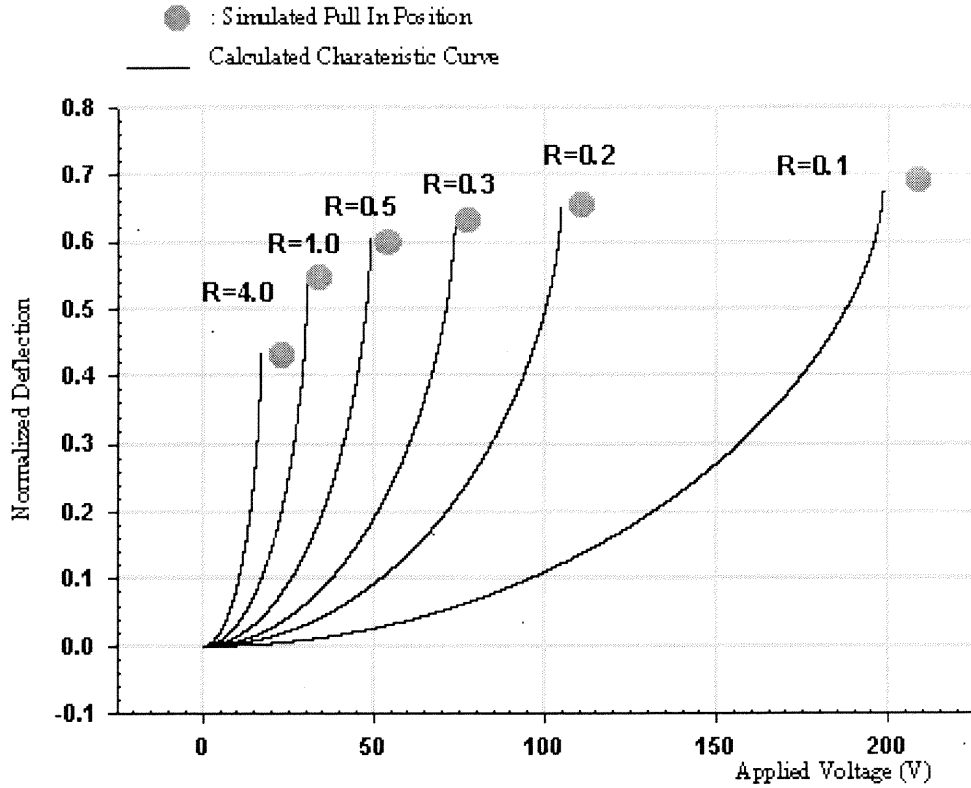


**Figure 2.17** Normalized Deflection vs. Applied Voltage for NC3 Torsion Mirror with Gap Depth=12um.

### 2.2.5 Simulation and Experiment on Charge Injection Method

As examples, two devices D3 and C3 are simulated using finite element method (FEM) software to verify their pull in positions and voltages, respectively. Though the two devices have different spring stiffness, the normalized pull-in position is found to be 0.44, consistent with the analytical results. Fig. 2.18 and 2.19 show FEM meshing for the two devices. Fig. 2.20 and 2.21 are simulated displacement profiles at the pull-in state.

Using the data in Fig. 2.22, the net oxide charge density is calculated to be  $\sim 6.2 \times 10^{10}/\text{cm}^2$  by C-V characteristics [34]. An empirical expression for repulsive electrostatic torque is curve fitted as the equation

$$M^{(R)}(\theta) = \frac{\epsilon_0 W (V + V_0)^2}{2} \left( \frac{L}{d} \right)^2 \left( 0.366 - 0.076\theta + 0.508\theta^2 + 2.23\theta^3 \right),$$

and for a D3 device. Other devices follow the same pattern with variable coefficients; this fact implies that the net oxide charge has a well-defined bias voltage dependence.  $V_0$  (12V for D3) is the bias voltage at which the mirror has zero deflection angle.

The simulated results, and the measured results without the effects of the net oxide charge present, are compared in Fig. 2.23. The travel range of D3 was increased from 44% to 62% at the cost of an increased bias voltage.

In summary, two passive feedback methods have been described which give increased travel range in electrostatic actuators but sacrifice bias voltage. These methods can be combined to optimize travel range for customized applications. Because of their simplicity, reproducibility and ease of manufacture, the methods may be preferred over other travel range extension methods in some electrostatic micro actuator applications, for example, variable capacitors of wide tunable range and large deflection micro mirror structures. Future work needs to be done to investigate the voltage-dependence of net oxide charge and its effects on repulsive electrostatic torque.

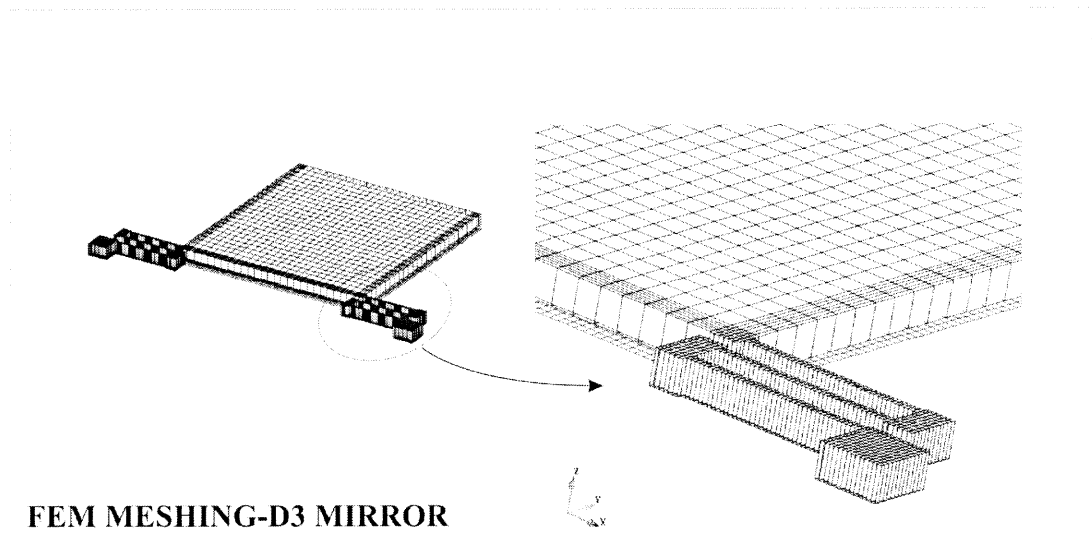


**Figure 2.18** Finite element meshing of D3 mirror, 7179 8-node block elements with 33409 nodes

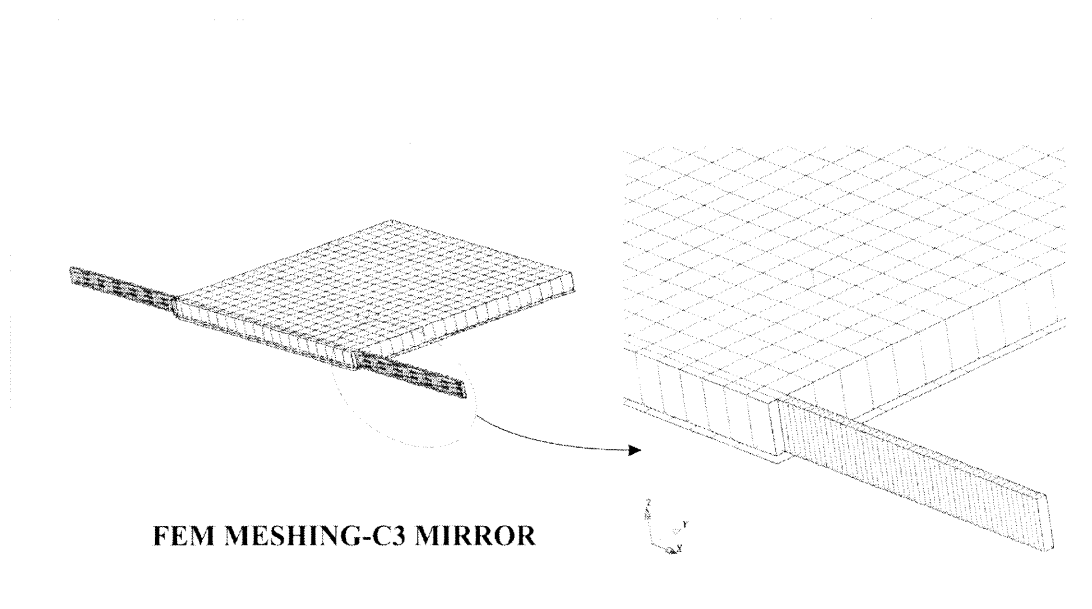


**Figure 2.19** Finite element meshing of C3 mirror, 940 8-node block elements with 6698 nodes

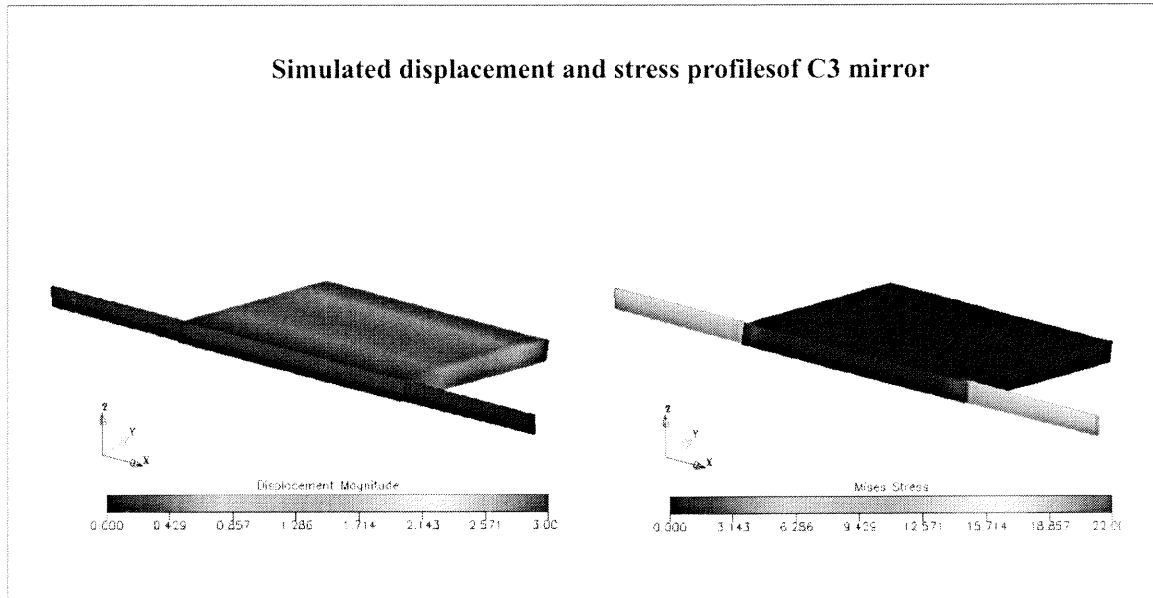


**Figure 2.20** Simulation of C3 device response to applied voltage



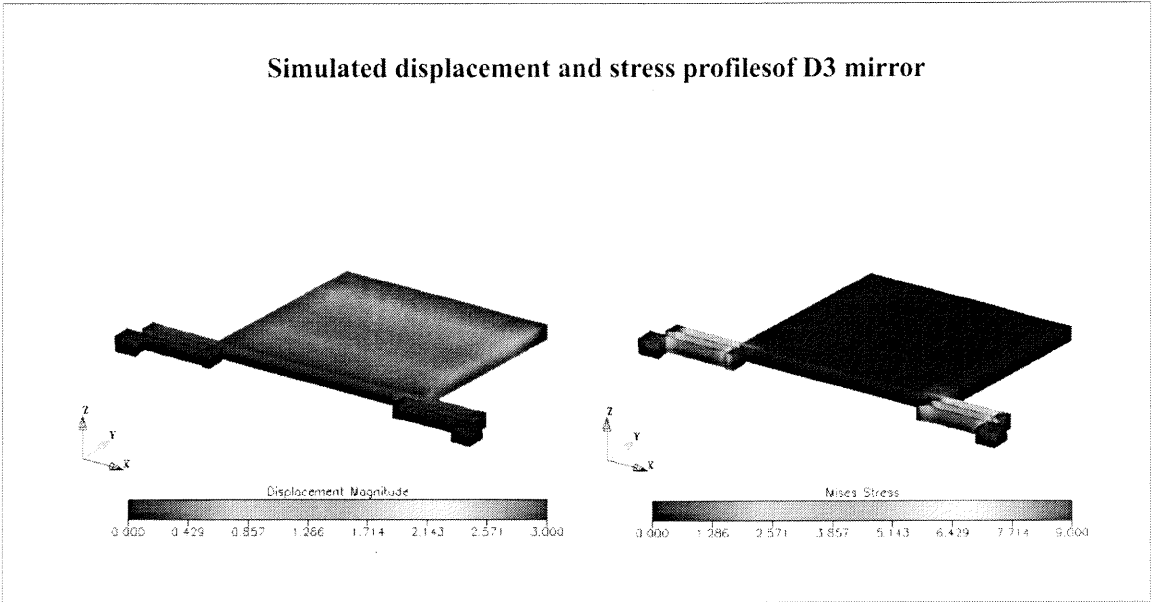


**Figure 2.21** Simulation of D3 device response to applied voltage

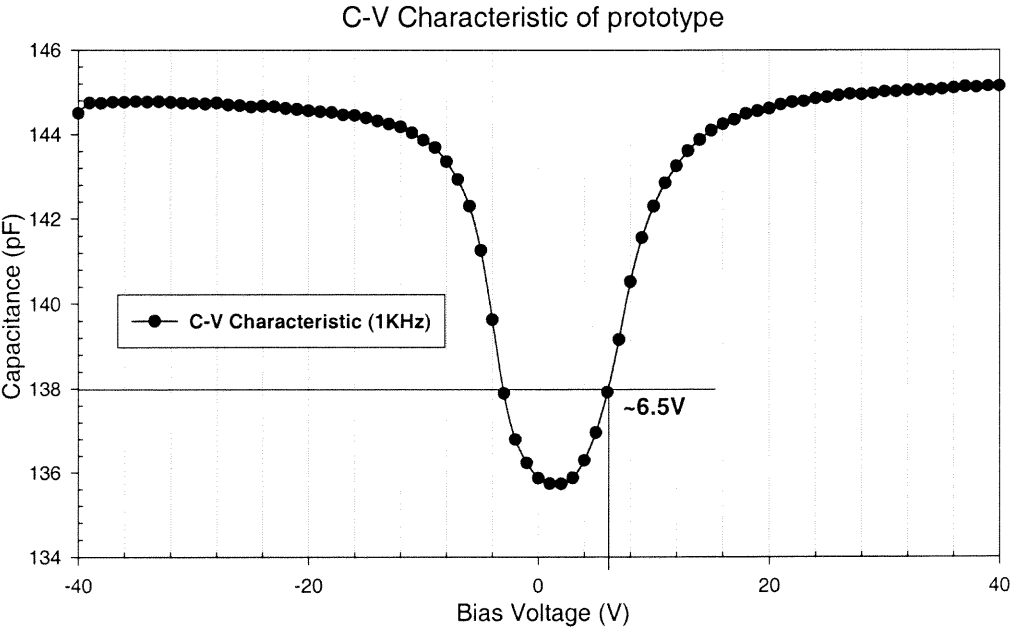


**Figure 2.22** C-V curve at 1KHz, indicating a 6.5V shift.

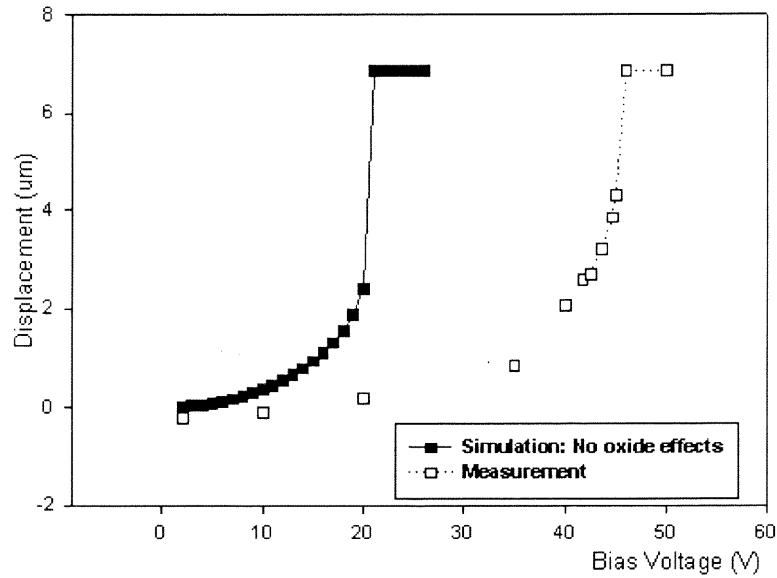


**Figure 2.23** The Measured Effects of Oxides on The Deflection Dependence on Bias Voltage for D3 Device.

## 2.3 Pull in Analysis of Complex Actuator Systems

### 2.3.1 Pull in summary from direct force analysis

Pull in analysis is important in that it determines the allowable tuning range of an electrostatic actuator. The traditional way to find the pull in data usually follows the following steps [26, 32, 54-56]:

- (1) Apply elastic theory to acquire the spring parameters of the movable actuator plate, then find the elastic restoring force with respect to the plate displacement.
- (2) Apply electrostatic Maxwell's equation to find the electric field throughout the actuator gap, then find the electrostatic attractive force with respect to the plate displacement.
- (3) Construct a force-balanced equation between elastic restoring force and electrostatic force with respect to the movable mirror plate.

- (4) Differentiate the force-balanced equation with respect to the displacement to obtain an equation for the pull in point.
- (5) Combine this equation with the original force-balanced equation to cancel the voltage term, then solve the equation to obtain the normalized pull in position which is independent of actuation voltage.
- (6) Insert the pull in position data back into the force-balanced equation to obtain the corresponding pull in voltage.

These routine steps are usually exhaustive, and sometimes to find the electrostatic attractive force can be very challenging, especially for actuator systems with irregular electrode shapes and sizes. In some cases, even the elastic restoring force is not easy to obtain, for example, for a deformable plate with strain stiffening. So the designer of electrostatic actuators encounters the puzzle of how to smoothly construct the force-balanced equation in a correct manner. The physics in actuator systems is relatively simple, but to get a definite solution, which should have an acceptable error level for engineering applications, is not always straightforward.

Analytical pull-in analysis has been carried out in the literature for just two simple actuator types, parallel plate actuators and rectangular torsion actuators. The pull-in analysis of the parallel plate actuator, which is the most popular example in MEMS textbooks, leads to a normalized pull-in displacement of  $1/3$  the initial gap depth, while for full-plate torsion actuators the normalized pull-in angle is about  $0.44$  of the full allowable angle. In both cases, no fringing field and strain stiffening effects have been considered. For partial plate torsion actuators, reference [26] provides numerical results. For torsion actuators, if electrode shapes are varied from a rectangular shape to other

geometries such as circular, elliptical, triangular, etc., the electrical field analysis based on the cylindrical symmetry of the wedged-shaped gap of the actuated rectangular torsion actuator no longer holds. For each of these cases, the designer has to start over from the basic Maxwell's electrostatic equation. Finite element analysis is an alternative way to treat the problem, but this requires expert-level know-how and enhanced computation resources. Designers may prefer an analytical method if it is straightforward to use and can provide results that can meet requirements for fast engineering design and prototyping.

### 2.3.2 Torsion actuators with general power function shape electrodes

The equation to describe a general power function is  $y = px^n$ , where  $p$  is a constant. The capacitance of the actuator system with a parabolic electrode is calculated as

$$C = 2\epsilon \int_0^L \frac{px^n dx}{d - (L - x)\theta}$$

When  $n = 1$ , the geometry of the electrode is a triangle. The capacitance is:

$$C = \frac{p\epsilon(-d + L\theta)\text{Log}[d] + (d - L\theta)\text{Log}[d - L\theta]}{\theta^2}$$

The pull in angle is found to be 0.542, which is independent of  $p$ .

When  $n = 2$  and  $n = 0.5$ , the geometry is a parabola, the capacitance is integrated respectively as:

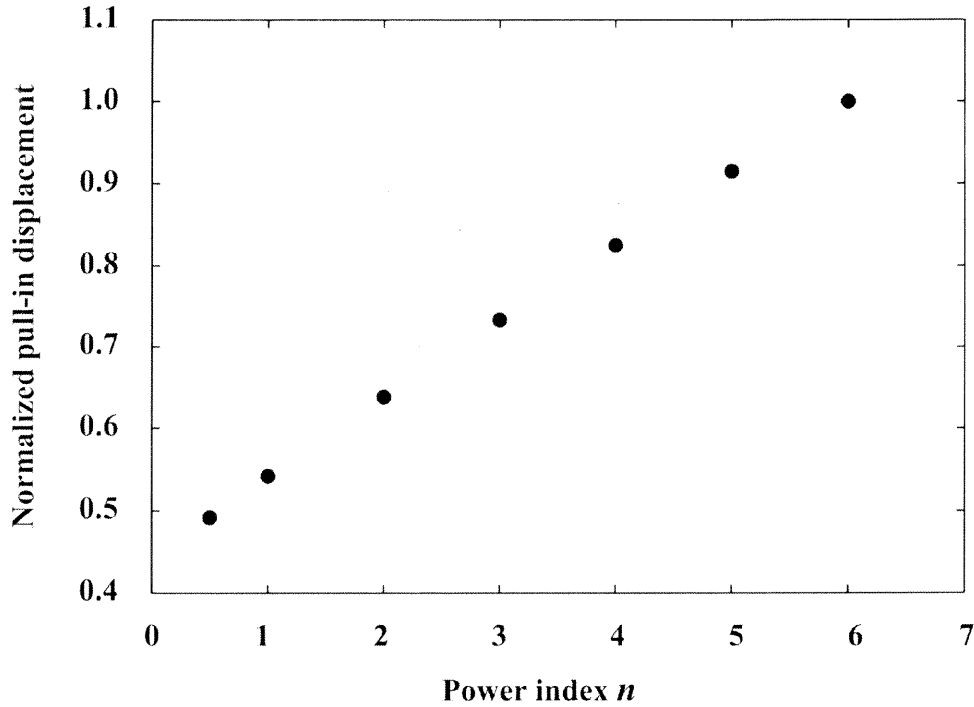


**Figure 2.24** The effect of power index on the normalized pull-in displacement.

$$C = \frac{p\varepsilon(L\theta(-2d + 3L\theta) + 2(d - L\theta)^2 \text{Log}[d] - 2(d - L\theta)^2 \text{Log}[d - L\theta])}{\theta^3}$$

$$C = \frac{4p\varepsilon(\sqrt{L\theta(d - L\theta)} + (-d + L\theta)\text{ArcTan}\left[\sqrt{\frac{L\theta}{d - L\theta}}\right])}{\theta^{3/2}\sqrt{d - L\theta}}$$

For  $n = 2$ ,  $\theta$  is found to be a constant of 0.638. For  $n = 0.5$ ,  $\theta$  is 0.492, a constant independent of  $p$  and the electrode length  $L$ . Generally, when  $n \in [0, \infty]$ , it has been shown that as  $n$  increases from 0.5 to 6,  $\theta$  linearly increases to full travel range. When  $n$  is higher than 6, the actuation can always reach full travel range [35]: The constant  $p$  of the power function does not affect the pull-in position.

### 2.3.3 The Effect of Strain Stiffening

As has been introduced in section 2.1, the capacitance-based approach can be applied to study the effect of spring stiffening on system pull in. Considering the 1D problem, equation (1) is written as

$$\frac{1}{2}V^2 \frac{dC}{dx} = K_1 X + K_3 X^3$$

The right side of the equation includes a non-linear elastic force term. The derivation is confined to the well-known Duffing's equation [36] from which time dependent forces are neglected to obtain the above quasi-static equation. The pull in point satisfies

$$\frac{1}{2}V^2 \frac{d^2 C}{dx^2} = K_1 + 3K_3 X^2.$$

After combining the two equations, the differential equation for pull in is obtained as

$$\left[ \frac{d^2 C}{dX^2} - \left( \frac{1}{1-f} \right) \frac{1}{X} \frac{dC}{dX} \right]_{X=X_{PIN}} = 0,$$

where  $f$  is defined as  $f\left(\frac{K_3}{K_1}, X\right) = \frac{2(K_3/K_1)X^2}{1 + 3(K_3/K_1)X^2}$ , i.e.  $0 < f < 2/3$ . The solutions of

the equation for different spring terms are shown in Fig. 2.25. It can be seen that a significant pull in jump occurs when the ratio of the cubic term over the linear term goes beyond  $\sim 20$  for a pure torsion actuator. The normalized pull in position value at ratio 20 is about 63%, and it increases asymptotically to about 65% for higher ratios.

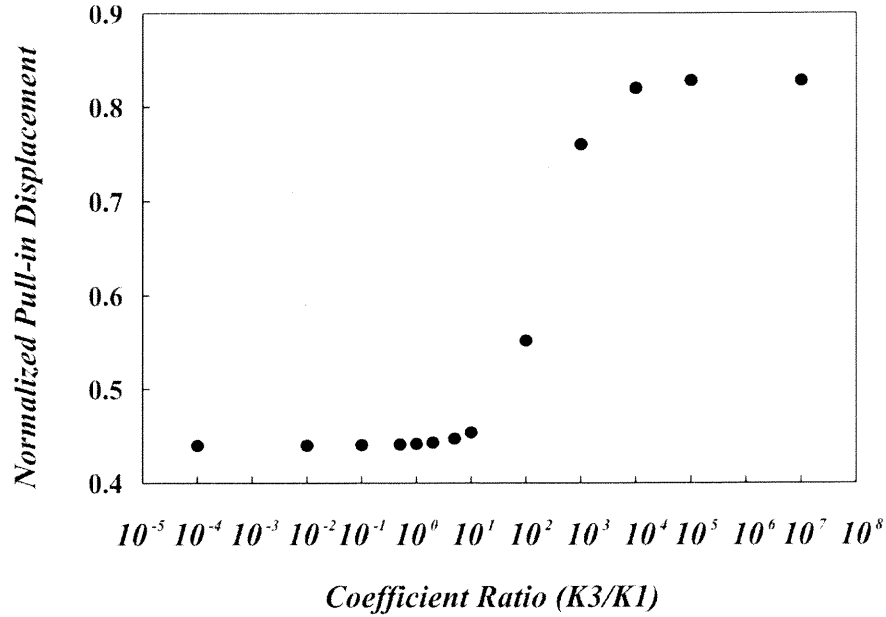


**Figure 2.25** The effect of stiffness coefficient ratio on the normalized pull-in displacement for a torsion actuator.

### 2.3.4 The Effect of Fringe Field Capacitance

Using the force-balanced method to investigate the effect of the fringing field capacitance on system pull in is difficult, while the capacitance approach provides a desirable shortcut to handle this problem. Two parallel plate capacitor systems are treated, parallel infinite plate and parallel plate disk capacitors. The former has a capacitance per unit length [37]

$$C = \frac{\epsilon_0 W}{D - x} \left[ 1 + \frac{2(D - x)}{\pi W} + \frac{2(D - x)}{\pi W} \log \left( \frac{\pi W}{D - x} \right) \right],$$

where  $D$  is the initial gap depth, and  $W$  is the plate width. Plugging the capacitance into the pull in position equation, a slight pull in shift from 33.3% to 34~35% is identified, depending on the aspect ratio of  $D/W$ . The pull in goes higher because of a comparatively slow changing rate of fringing field capacitance with respect to that of an ideal parallel plate capacitance.

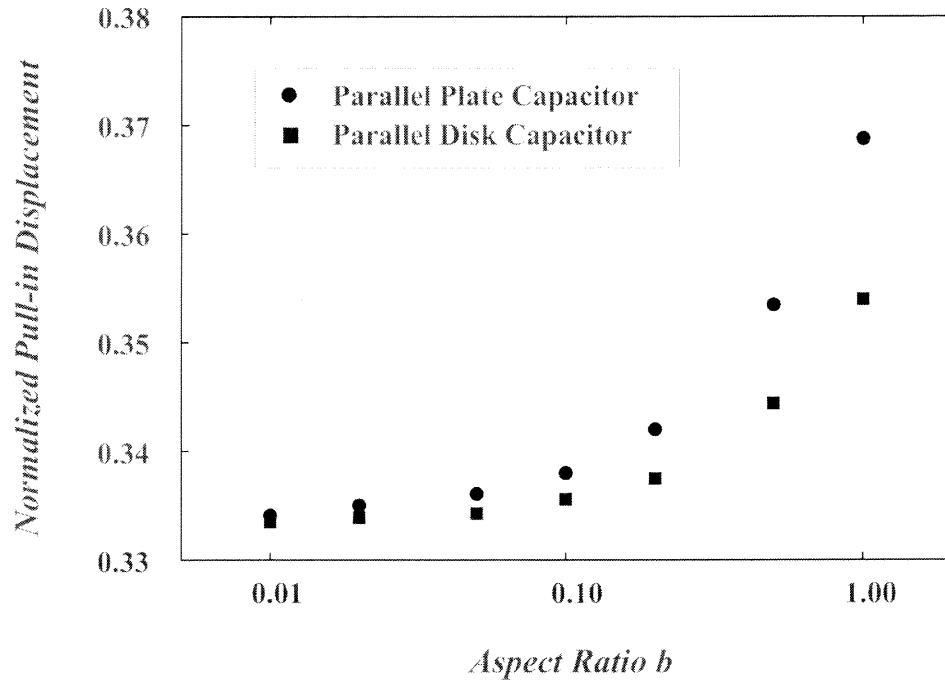


**Figure 2.26** The effect of fringing fields on system pull in.

For a parallel plate disk capacitor, the capacitance formula is given by

$$C = \frac{\epsilon_0 \pi R^2}{D - x} \left[ 1 + \frac{b - x/R}{\pi} \ln \left( \frac{16\pi}{b - x/R} - 1 \right) \right],$$

where  $b$  is defined as the aspect ratio of the disk capacitor,  $b = \frac{D}{R}$ . This capacitance formula is accurate for  $0.01 \leq b \leq 1.0$ . Most MEMS capacitor systems fall into this range due to the low voltage actuation requirement. The normalized pull in position with respect to this aspect ratio is given in Fig. 2.26. It can be seen that the system pull in has only a slight increase due to the effect of the fringing field capacitance.



## CHAPTER 3

### STUDY OF EXAMPLE DEVICE APPLICATIONS

The microelectromechanical systems (MEMS) mirror and mirror array have been used in a wide range of applications including transmission and switching for telecommunications, free space communications, displays, spatial light modulators, adaptive optics and printers and scanners. Particularly in telecommunications networks, the transition from time division multiplexing (TDM) to dense wavelength division multiplexing (DWDM) provides an application-rich environment for MEMS components and systems [39]. MEMS-based micro mirror technologies allow scalable, all-optical, high-speed networking systems to be constructed at low cost. Typical devices currently under research and development (R&D) include WDM add/drop switches [40], optical cross-connects (OXC) [41, 42], optical switches [43-45], variable optical attenuators (VOA) [46-48], WDM equalizers [49], optical filters [50], wavelength locks and stabilizers [51], to name a few. Most of these optical devices can be conveniently actuated by electrostatic force.

In this chapter, the proposed mirror design theory of Chapter 2 will be used to analyze and design micro mirror structures for VOA, OXC and wavelength filter applications. First the development of a large area, electrostatically actuated micro-mirrors is described for use as variable attenuators and switches in optical networking systems. The designed mirrors are fabricated by ultra thin silicon wafer bonding technology combined with deep reactive ion etching (DRIE). The ultra thin wafer bonding technology provides a fast prototyping method for the verification of mirror design. As an alternative to silicon fusion bonding, which requires high temperature

above 1000 degrees C, a low temperature silicon bonding method was developed using SU-8 as a bonding and spacer material. The SU-8 fabrication method was used to prototype a silicon mirror based Fabry-Perot interferometer with an electrostatic tuning function. For large deflection mirrors as required by OXC systems, the capacitance-based design theory provides a convenient approach to investigate the electrode shape effect on the pull in property of the mirror structures.

### **3.1 Variable Optical Attenuator**

#### **3.1.1 Introduction**

The current optical attenuator is designed as an adjustable optical power limiter wherein a reflective-metal-coated single crystal large micro mirror is rotated about its axis to produce voltage-controlled variable attenuation for the output light beam [50]. In order to achieve low insertion loss with typical beam divergences and system geometries, the reflective surfaces must be rather large (e.g.,  $\sim 700 \times 700 \mu\text{m}^2$ ). However, large flat mirrors cannot be easily fabricated using conventional polysilicon deposition and micromachining technology (e.g. MUMPs), because the composite mirror structure (e.g., Cr/Au on Si) constitutes a bimorph structure that is non-planar and deforms with variations in temperature. While it may be possible to work around these problems by careful design and stress engineering, a simpler and more manufacturable solution is to make the device insensitive to stress by using wafer bonded, stress-free, single-crystal silicon films. Hence, optical devices are fabricated using fusion bonding of single-crystal, ultra-thin silicon wafers to form large area, relatively thick (20-50 $\mu\text{m}$ ) mirrors which do not deform. Moreover, this approach allows the development of highly

reflective or wavelength-selective devices based on dielectric stacks, where the stresses would be more difficult to compensate. Hence, optical devices were fabricated using fusion bonding of single-crystal, ultra-thin silicon wafers to form large area, relatively thick ( $\geq 20\mu\text{m}$ ) mirrors which do not deform. In this thesis emphasis is placed on the MEMS design, fabrication and electro-mechanical characteristics of the large torsion mirror.

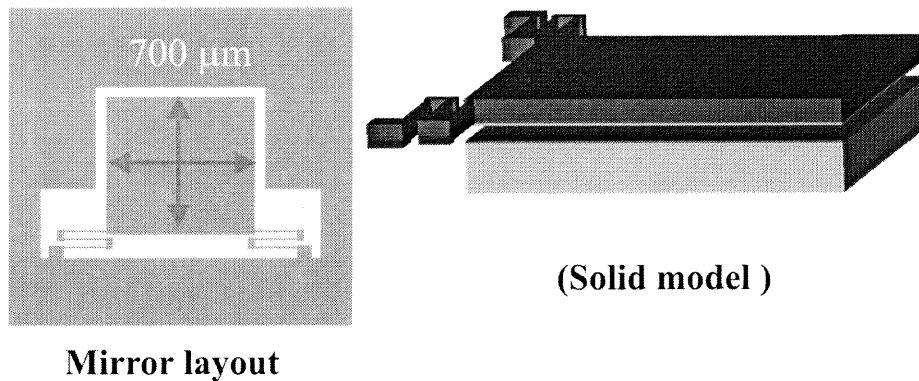


**Figure 3.1** Schematic of the large area torsion mirror used as an optical attenuator.

To move the optical input beam relative to the optical path so as to change coupling of light beams between the input port and the output port, the reflective element can be supported by a flexible suspension element comprising twin hinges. Each hinge is attached at one end to a fixed anchor and at its other end to the optical reflective element. The hinges are identical in length and flexibility and are spaced apart in the direction of displacement of the optical mirror. The twin hinges obviate the need for a precision sliding stage that is usually macro scale in size and expensive to integrate. Micromachined electrostatic torsion mirrors, that provide angular motion to reflect an input light beam to a desirable output direction, become a promising technical choice in

micro scale that can be driven by an external or integrated electronic source. A typical torsion mirror layout and solid view with a full-plate actuation scheme is illustrated in Fig. 3.1. The objective mirrors should have a reflective area no less than  $500 \times 500 \mu\text{m}^2$ , and the actuation should be in the range of 10~50V with a tunable deflection angle up to  $0.5^\circ$ . Using the capacitance-based design theory proposed (see chapter 2 on rectangular torsion mirror design), more than 16 prototype devices have been designed and simulated with various mirror areas (proof mass) and torsion spring dimensions.

### 3.1.2 The Effect of Gravity

After implementing these softer spring designs for the purpose of low voltage actuation, the proof mass of the mirror volume is no longer negligible. The effect of the relatively heavy proof mass is that it introduces a non-zero initial deflection. It can be shown that the initial deflection is proportional to the square of the mirror length, proportional to mirror mass, but is reciprocally proportional to the spring stiffness, as shown in Eq. 3.1.

$$\begin{aligned}
 K_t \theta &= Mg \cdot \frac{L_{\text{mirror}}}{2} \cos \theta \\
 \text{or : } K_t \frac{\Delta Z}{L_{\text{mirror}}} &= Mg \cdot \frac{L_{\text{mirror}}}{2} \\
 \therefore \Delta Z &= \frac{Mg \cdot L_{\text{mirror}}^2}{2K_t}
 \end{aligned} \tag{3.1}$$

The stiffness of the folded torsion springs can be written as

$$K_t = \frac{Gt_{\text{beam}} W_{\text{beam}}^3}{8L_{\text{beam}}} \left[ \frac{16}{3} - 3.36 \frac{W_{\text{beam}}}{t_{\text{beam}}} \left( 1 - \frac{W_{\text{beam}}^4}{12t_{\text{beam}}^4} \right) \right],$$

where  $t_{\text{beam}}$ ,  $W_{\text{beam}}$  and  $L_{\text{beam}}$  are the spring thickness, width and length, respectively. The mirror weight is  $Mg = \rho_{\text{Si}} g L_{\text{mirror}} W_{\text{mirror}} t_{\text{mirror}}$ . It also holds that  $t_{\text{beam}} = t_{\text{mirror}}$ . It is concluded

that the zero deflection effect due to the mirror gravity is most sensitive to spring width (Notice that the shorter side of the spring cross section should be plugged in with a cubic power index).

If a 50 $\mu\text{m}$  thick ultra thin silicon wafer is bonded to the substrate and the spring width defined by DRIE is 5 $\mu\text{m}$ , then the spring torque stiffness can be calculated as  $\sim 2.38 \times 10^5 \mu\text{N} \cdot \mu\text{m}$  for a net spring length of 1200 $\mu\text{m}$ . Then due to gravity, a 700 $\times$ 700 $\mu\text{m}^2$  mirror proof mass will have a zero deflection  $\sim 0.62 \mu\text{m}$ . Changing the mirror thickness from 50 $\mu\text{m}$  to 20 $\mu\text{m}$  would not make a substantial difference since gravity and stiffness are scaled in an identical way with respect to mirror thickness. The calculated result for zero deflection for this thickness is  $\sim 0.69 \mu\text{m}$ . The pull in voltages for these two mirror thickness cases are 8.2V and 13.4V, respectively.

To check how sensitive the gravitational deflection is to the length of the shorter side of the spring cross section, a 10 $\mu\text{m}$  spring structure with the same fold number and spring length are considered. It is easily shown that in this case the zero deflection due to gravity becomes 76nm and 86nm for mirror thickness of 50 $\mu\text{m}$  and 20 $\mu\text{m}$ , respectively. The pull-in voltages for these two mirror thickness cases are 23.2V and 31.9V, respectively.

The above calculation implies that although thinning the spring width can greatly reduce the actuation voltage, the approach introduces a non-negligible gravity-induced zero deflection. The softer spring design lowers the actuation voltage, lowers the resonant frequency of mirror structure and also introduces the gravitational deflection at zero bias. It should be mentioned that the gravitational deflection, in principle will not affect the normalized pull-in position, but it does affect the actuation voltage. Its effect on actuation

voltage can be approximated by modifying the initial distance from the mirror tip to the substrate. In summary, the softer spring configuration by thinning the spring cross section will have the actuation voltage reduced in a direct manner, and the actuation voltage can be further reduced by the gravitational initial gap depth modification in an indirect manner.

### 3.1.3 Fabrication by Ultra Thin Silicon Fusion Bonding (UTSFB) and Deep Reactive Etching (DRIE)

The major prototyping steps are illustrated in Fig. 3.2. First, bulk, anisotropic KOH etching was used to define cavities in 4-inch, low resistivity, (100) silicon substrate wafers, which were subsequently oxidized to a thickness of  $\sim 1\mu\text{m}$  for electrical isolation (see Fig. 3.2(A)). Ultra-thin, low resistivity silicon wafers from Virginia Semiconductor, Inc. of  $\sim 50\mu\text{m}$  thickness were oxidized and then fusion bonded to the thick substrate wafers in vacuum, forming sealed cavities (Fig. 3.2 (B)). The top wafer was subsequently patterned (Fig. 3.2 (C)), and the mirror and spring structures were formed by inductively coupled plasma deep reactive ion etching (DRIE) through to the underlying oxide. Finally, Cr/Au was deposited on the mirrors by physical vapor deposition (see Fig. 3.2 (D)).

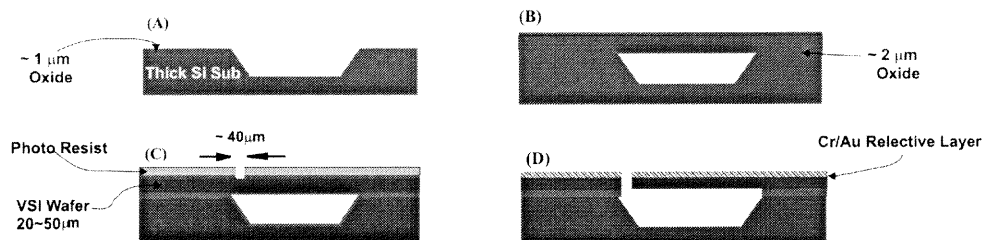


**Figure 3.2** Schematic of the fabrication sequence: (A) cavities are anisotropically etched into a standard thickness silicon wafer which is subsequently oxidized; (B) an ultra-thin silicon wafer is fusion bonded over the etched wafer, forming sealed cavities; (C) the mirror surface and springs are patterned into the top wafer for DRIE; (D) completed devices, with Cr/Au coating for high reflectivity.

The wafers were diced and mounted in 16 pin dual-in-line packages for testing. Sixteen prototype designs were fabricated, with various combinations of mirror sizes and spring designs. The mirror dimensions varied from 400 to 700  $\mu\text{m}$  and the springs from 5 to 10  $\mu\text{m}$ . Fig. 3.3(A) shows a scanning electron microscope (SEM) image of a typical device, showing the extremely large ( $700 \times 700 \mu\text{m}^2$ ) mirror surface and supporting springs. The entire mirror is suspended in space over the etched cavity, only supported at the two places where the serpentine springs join the surrounding region. Fig. 3.3 (B) and (C) show close-ups of the springs themselves.

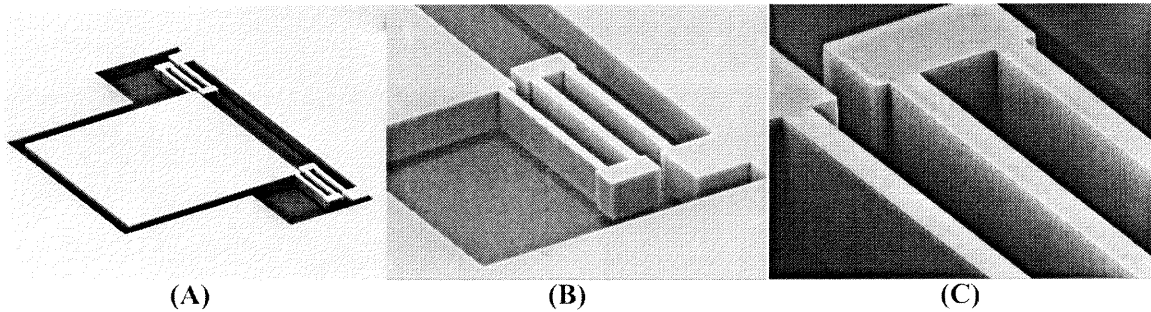


**Figure 3.3** (A) SEM Micrograph of one of the micromirror structures, and (B) and (C) close-up views of the springs formed by deep reactive ion etching. For scale, the top sections of the springs are 10 $\mu\text{m}$  wide.

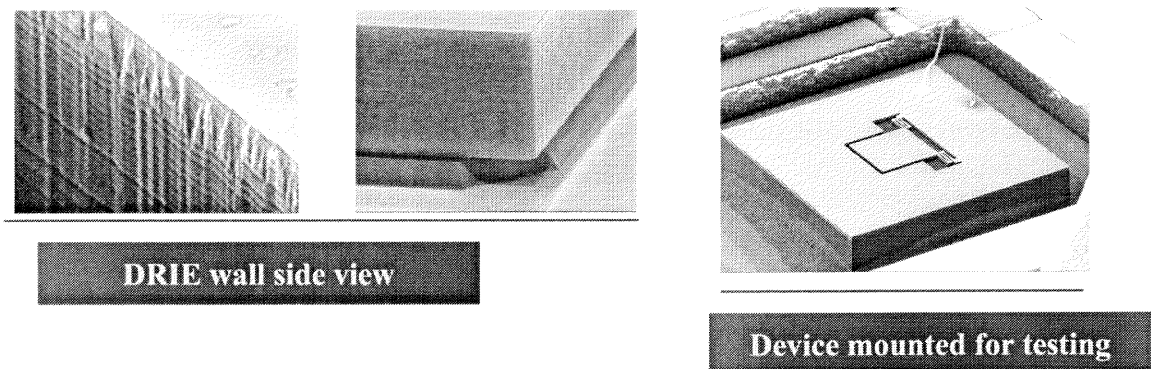


**Figure 3.4** SEM Micrograph of DRIE side walls of one of the micromirror structures, and mounting for quasi-static test.

The DC offset actuation of the device was characterized with a Wyko optical profilometer. With zero applied bias, the large movable mirror plate was essentially flat, having a very slight upward deflection of  $0.014^\circ$  to the wafer surface. At higher bias voltages, the mirror plates deflected downwards into the cavity. Fig. 3.5 is the profilometer image of the D3 device with an applied voltage of 55V. Fig. 3.6 (B) shows a typical depth profile along the deflection plane, indicating a downward deflection of  $\sim 7\mu\text{m}$  at the end of the mirror plate, corresponding to an angle of  $0.5^\circ$  to the wafer surface. Note that the mirror remains extremely flat; this is true of the entire mirror surface at all applied voltages, with some in excess of 100V at which the device goes far beyond its pull-in state.

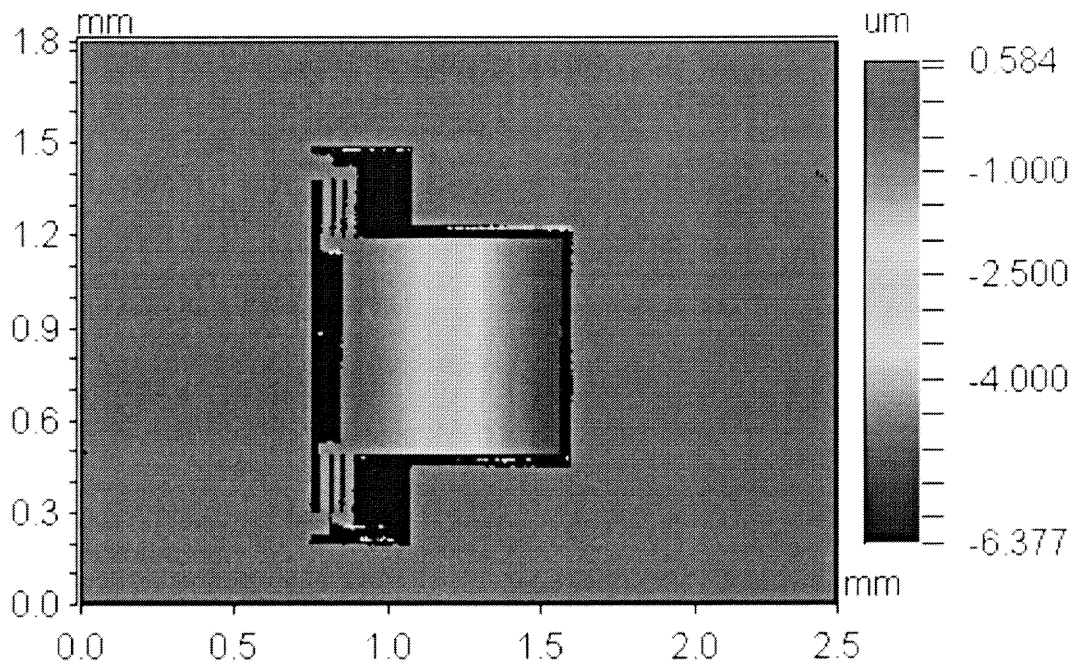


**Figure 3.5** Wyko profilometer data, showing mirror deflection at 55 volts. Profilometer image of the actuated device, confirming that the deflection is only along the symmetry axis. The deflection is  $\sim 7\mu\text{m}$  at the mirror tip at this applied voltage.



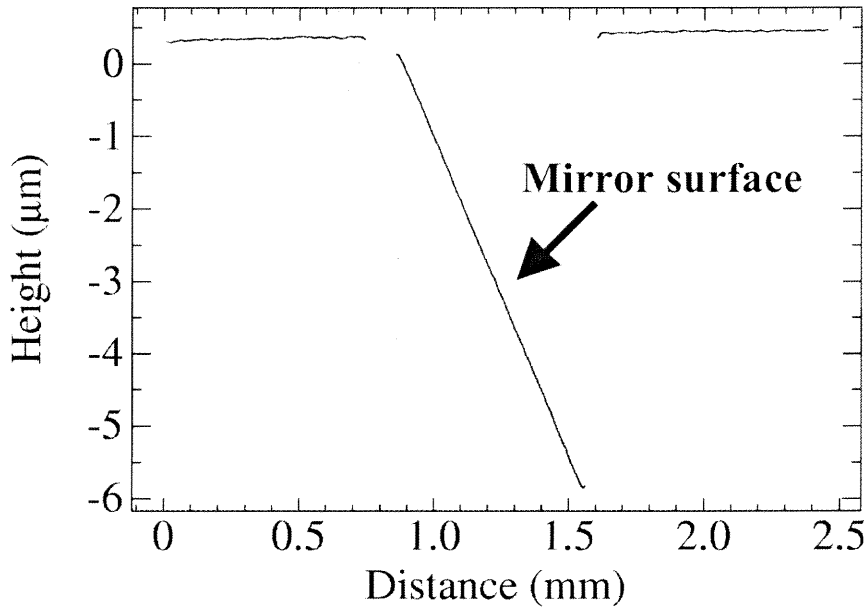


**Figure 3.6** Mirror displacement data extracted from Wyko profilometer along the mirror length confirming that the deflection is only along the symmetry axis and that the the mirror reflective surface is flat, even when the device is in its pull-in state.

### 3.1.4 The Effect of Trapped Charges

The mirror fabricated using the above mentioned process becomes a verification of the proposed travel range extension approach since the two inner surfaces of the cavity have identical oxide layers. As has been described in Chapter 2, the charge injection method for travel range extension, the repulsive Coulomb's force would cause the mirror plate to experience an upward deflection at zero bias voltage. This upward deflection in the fabricated mirror devices was observed, as shown in Fig. 3.7. Considering the effect of gravity (contributes  $\sim 76\text{nm}$ ), the tip deflection due to this electrical force will be larger than  $\sim 230\text{nm}$ . Due to the presence of the oxide charge in the inner cavity interfaces, the device is expected to regain its horizontal position at a certain applied voltage at which the charge induced by the bias source exactly compensates the oxide charge such that on one electrode, the effective charge density goes close to zero. Using the D3 mirror a 12V

threshold was measured for the mirror to lose its initial deflection, returning to the horizontal position.

Table 3.1 lists the dimensions for D3 and C3 devices. Device deflection was measured by 2D profiling using a WYKO optical profilometer. It can be seen (Fig. 3.7) that the device does exhibit a slight upward deflection at zero bias (about 200nm for D3 device). The deflection should not be attributed to residual stress due to the fabrication process used. 2D profiling at pull-in confirmed the  $6.96\mu\text{m}$  gap depth as shown in Fig. 3.5.

Without considering the repulsive interaction effect of positive fixed oxide charges, numerical approximations by expansion technique and simulation by commercial FEA software MemCad 4.6 [57] are used to find the dependence of deflection angle on bias voltage. Results are given as Fig. 2.20 and Fig. 2.21 where the pull-in voltage and largest stable deflection angle are found to be 25.2V, 0.440 (normalized angle) for the D3 device and 45.5V and 0.442 for the C3 device. The pull-in angle has only a small increase over 0.44 due to the influence of oxide capacitance at the cost of several volts bias voltage. The travel range cannot significantly be increased by just the oxide capacitance effect because the  $\sim 1\mu\text{m}$  oxide capacitance is much larger than the air gap capacitance. Therefore, even though the oxide capacitance is in series with the air gap capacitance, its effect on extending travel range is too small to be of value in a real application. As has been proposed in Chapter 2, in order to extend travel range using a series capacitor, the chosen value of the series capacitance should be comparable to the initial air gap capacitance.

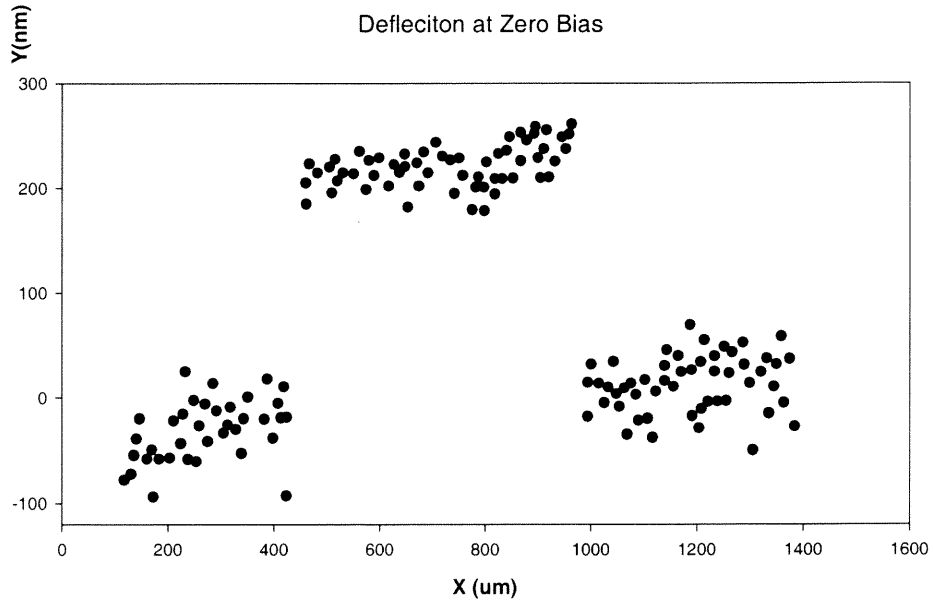


**Figure 3.7** Zero bias profiles of D3 device along the mirror length showing an upward deflection.

**Table 3.1** Summary of device parameters.

DIMENSIONS ( $\mu\text{m}$ )	D3	C3	OTHER PARAMETERS
$W_{\text{mirror}}$	700	600	$G=0.73 \times 10^5 \text{ MPa}$ $\epsilon_0=8.85 \times 10^{-12} \text{ F/m}$ $\epsilon_{\text{ox}}=3.85$ $\rho_f=9.5 \times 10^{10} / \text{cm}^2$ $t_{\text{ox}}=0.5 \mu\text{m}$
$L_{\text{mirror}}$	680	580	
$t_{\text{mirror}}$	48.6	48.6	
$d$	6.96	6.96	
$W_{\text{beam}}$	10	10	
$L_{\text{beam}}$	600	350	
$t_{\text{beam}}$	48.6	48.6	
Stiffness ( $\mu\text{N} \cdot \mu\text{m}$ )	$3.382 \times 10^6$	$4.428 \times 10^6$	

## 3.2 Fabry-Perot Wavelength Selector

### 3.2.1 Basic of Fabry-Perot Filter

In many optical applications, it is desirable to use a scanning Fabry-Perot interferometer, or etalon, to modulate the intensity of a narrow band of light, or to select single or multi wavelengths from broadband or multi-spectral light. Various MEMS based tunable laser implementations of Fabry-Perot interferometers have been investigated for the purposes of cost-effective miniaturization and batch fabrication [50]. The simplest configuration of a Fabry-Perot etalon consists of two parallel planes separated by an air gap  $D$ . The reflective surfaces are usually formed by metallic thin films of aluminum, silver or gold, or stacked dielectric films on the surfaces of plates. For MEMS devices, the enclosed air gap  $D$  generally varies in the nanometer to micrometer range if the movable plate is actuated electrostatically.

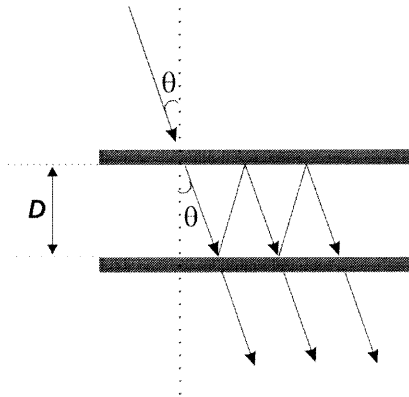


**Figure 3.8** A simple optical scheme of a Fabry-Perot filter.

As shown in Fig. 3.8, the Fabry-Perot etalon operates via multiple beam interference. When the difference in optical path length between the rays transmitted at successive reflections is such that the emerging waves are in the same phase, constructive

interference will occur and the Fabry-Perot will show a maximum in transmission. The phase difference between two successive rays is given by:

$$\delta = 2\pi \frac{2n'd \cos \theta}{\lambda}.$$

where  $\lambda$  = The wavelength of the radiation in vacuum (or air),

$d$  = The separation of the reflecting surfaces,

$n'$  = The index of refraction of the material between the reflecting surfaces,

$\theta$  = The angle of incidence, as shown in Fig. 2.33.

The transmission intensity distribution is [59]:

$$\frac{I^{(t)}}{I^{(i)}} = \frac{1}{1 + \frac{4R}{(1-R)^2} \sin^2(\delta/2)} = \frac{1}{1 + A \sin^2(\delta/2)}.$$

where,  $A = \frac{4R}{(1-R)^2}$ . The transmitted intensity reaches a maximum when  $\delta = 2m\pi$ , ( $m$  is

an integer) corresponding to  $m = \frac{2n'd \cos \theta}{\lambda_0}$  for a specific wavelength  $\lambda_0$ . If for  $m + 1$

and  $\lambda_0 - f$ ,  $(m+1)(\lambda_0 - f) = 2n'd \cos \theta$ , then,

$$f \approx \frac{\lambda_0}{m}.$$

Referred to as "*free spectral range*" (FSR), this parameter is frequently used to indicate how close two wavelengths must be to produce adjacent, same-order fringes.

Another important concept is the Full Width of Half Maximum (FWHM) of the transmission pass-band of the Fabry-Perot. Let  $\Delta\lambda_{FWHM}$  be the FWHM and the values of transmittance at  $\lambda_0 \pm \Delta\lambda_{FWHM}$  are half of that at  $\lambda_0$ . Because

$$\frac{2n'd \cos \theta}{\lambda_0} = m, \quad \text{and}$$

$$\begin{aligned} \delta &= 2\pi \cdot \frac{2n'd \cos \theta}{\lambda_0 \pm \frac{\Delta\lambda_{FWHM}}{2}} \approx 2\pi \cdot \frac{2n'd \cos \theta}{\lambda_0} \left( 1 \mp \frac{\Delta\lambda_{FWHM}}{2\lambda_0} \right) \\ &= 2\pi m \left( 1 \mp \frac{\Delta\lambda_{FWHM}}{2\lambda_0} \right), \end{aligned}$$

one can get:

$$\begin{aligned} \sin^2 \frac{\delta}{2} &= \sin^2 \left( m\pi \mp \frac{m\pi\Delta\lambda_{FWHM}}{2\lambda_0} \right) \\ &= \sin^2 \left( \frac{m\pi\Delta\lambda_{FWHM}}{2\lambda_0} \right) \\ &\approx \left( \frac{m\pi\Delta\lambda_{FWHM}}{2\lambda_0} \right)^2, \quad (\Delta\lambda_{FWHM} \ll \lambda_0). \end{aligned}$$

Half maximum of the pass-band means:

$$\frac{I^{(t)}}{I^{(i)}} = \frac{1}{1 + A \sin^2 \left( \frac{\delta}{2} \right)} = \frac{1}{2}.$$

$$\Rightarrow \quad \Delta\lambda_{FWHM} = \frac{2f}{\pi\sqrt{A}}.$$

$A = \frac{4R}{(1-R)^2}$  and  $f \approx \frac{\lambda_0}{m}$  is the free spectral range. Combining these equations will

give another important concept, finesse, the ratio of free spectral range and the FWHM:

$$Finesse = \frac{f}{\Delta\lambda_{FWHM}} = \frac{\pi\sqrt{A}}{2} = \frac{\pi\sqrt{R}}{1-R}.$$

*Finesse* describes the property of reflectivity of the surfaces. A relative low reflectivity  $R$  leads to a lower finesse or broader maxima spacing, while a higher reflectivity results in narrow maxima spacing and high finesse.

### 3.2.2 Mirror Plate Direct Actuation Scheme

The Fabry-Perot tunable interferometer of the present research contemplates as one of its principal objectives a comparatively low cost, miniaturized, high-speed, low-voltage actuated component. The research objective is to realize a miniaturized electrostatic tunable Fabry-Perot interferometer with millisecond switching time, and  $<100V$  actuation voltage. To meet the low cost requirement, wafer level processing is developed to enable high yield, low cost batch fabrication.

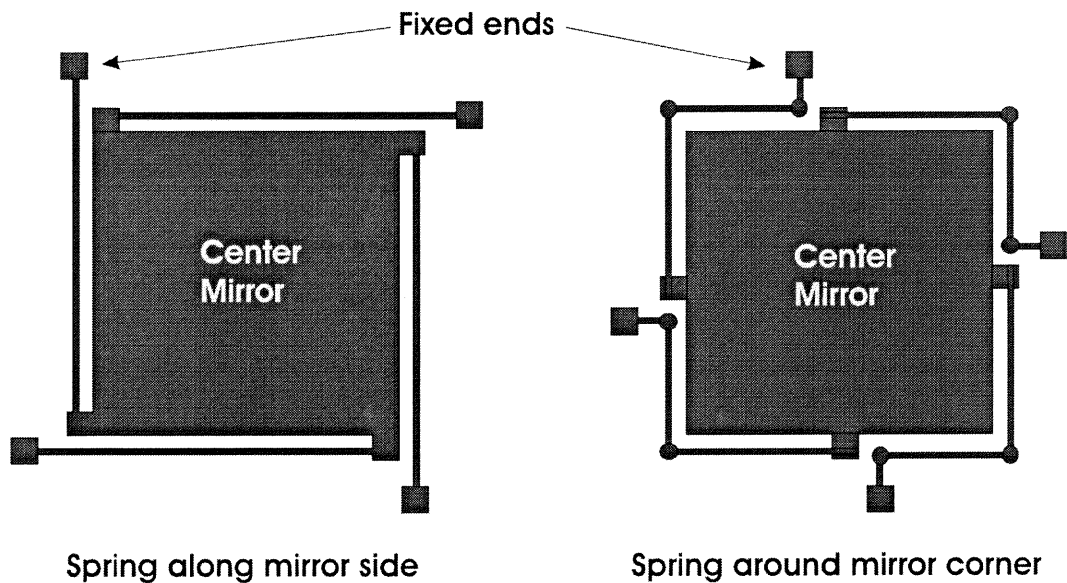


**Figure 3.9** Layout of two types of spring configurations.

Sixteen device layouts are designed and simulated to screen out device dimensions to meet the low voltage requirement. With mirror thickness predefined by

commercial availability, design focuses on the effects of various spring configurations. Softer stiffness is obtained by increasing folded spring number. A more subtle way to realize a softer elastic structure is found by changing the usual side-spring configuration to the corner-spring configuration. Fig. 3.9 illustrates the corner-spring compared to side-spring configuration, using a one fold spring around the square shaped center mirror. The spring softening obtained by using this corner-spring scheme can be visualized from Fig. 3.10. For example, a 3 folded side-spring structure has a net stiffness  $25\mu\text{N}/\mu\text{m}$  while for 3 folded corner-spring structure, the stiffness becomes  $18\mu\text{N}/\mu\text{m}$ . This reduced stiffness will introduce a roughly 15% reduction of the actuation voltage.

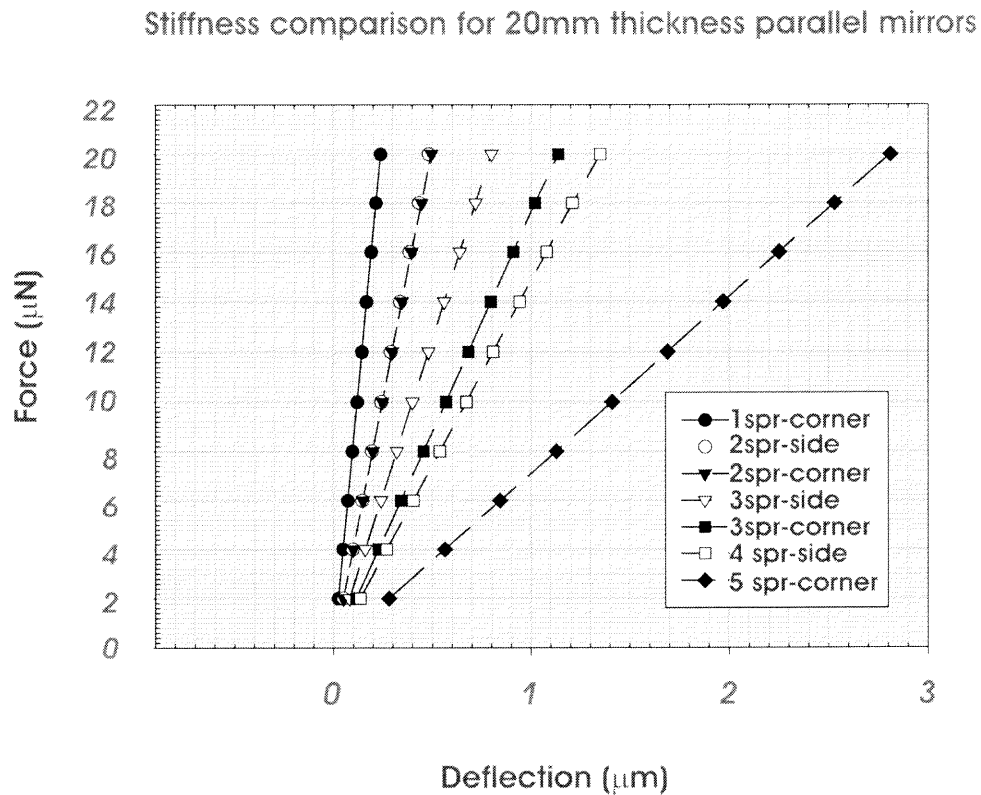


**Figure 3.10** Spring stiffness comparison for two types of spring configurations with various folded-spring numbers.



Good linearity of spring stiffness is obtained whatever the spring number and configurations are for the project-specified gap tuning range. Stiffness can be dramatically dropped by decreasing the mirror thickness, increasing the spring number, and changing the spring configuration. The mode spectra of the structure, including mode shapes and orders, display a variation due to changes in spring configuration, as can be seen in Fig. 3.11. Spring configuration is a critical design factor, because it not only softens the spring constant for out of plane motion or actuation mode, but also changes the pattern of mode shapes. The 1<sup>st</sup> natural frequency of the softest simulated mirror structure, i.e. a 5 spring-cornered mirror, is  $\sim 1.8\text{KHz}$ , satisfying the *ms* switching time requirement.

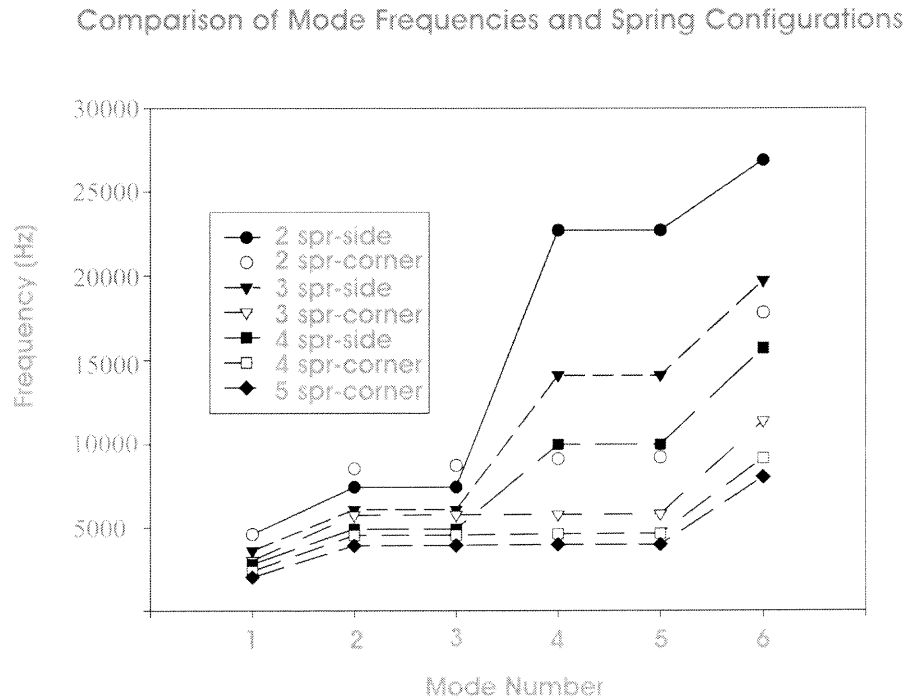


**Figure 3.11** Comparison of mode frequencies and spring configurations. “2 spr-side” and “2 spr-corner” represent two springs along each side or corner of the square mirror, respectively, etc.

The electrostatic and elastic coupled simulation of this 4-spring structure gives  $2.76\mu\text{m}$  piston-only displacement in the vertical (z axis) direction, providing sufficient phase modulation for a  $1.55\mu\text{m}$  input beam. It should be mentioned that at this characteristic center wavelength for optical telecommunications, only 50V is required for current bulk silicon devices to achieve a full  $2\pi$  phase modulation. It is expected that with the technology development of ultra-thin silicon wafer fabrication and with the shrinkage of feature size in deep reactive ion etching, the thinning of silicon wafer thickness and spring width will provide a way to achieve full wavelength phase modulation at a standard CMOS voltage.

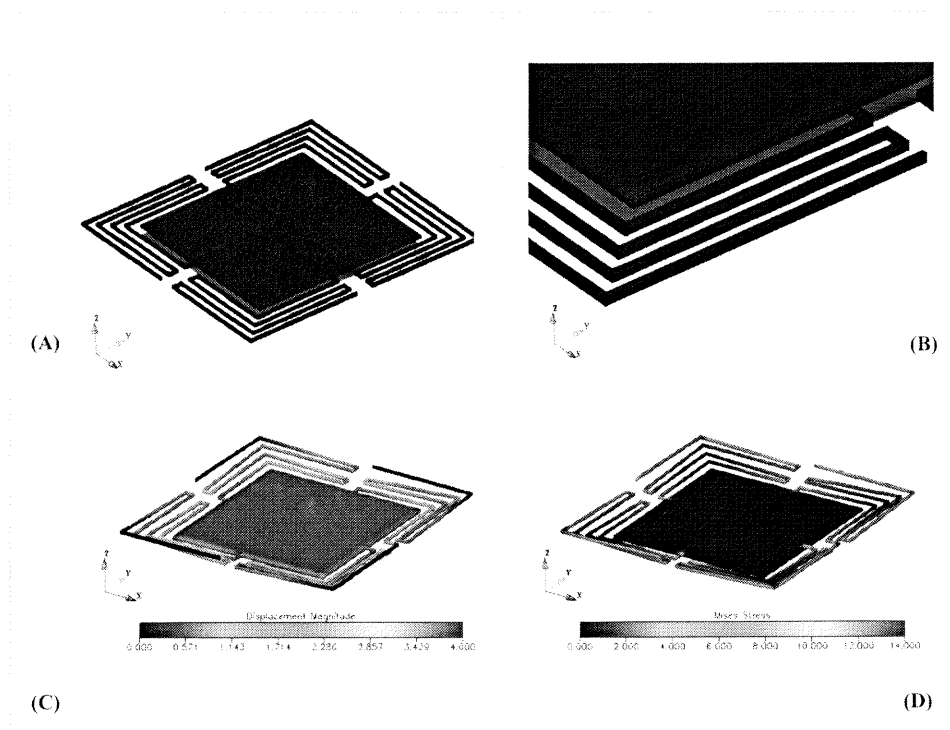


**Figure 3.12** (A) Finite element meshing of the mirror structure, meshing uses 3200 8-node block elements with 14395 nodes. (B) The graph shows the meshing of the elastic folded springs, and this high stress area needs fine meshing. (C) The graph illustrates the mirror behavior under 100V bias electrostatic load, showing a maximum displacement of  $2.76\mu\text{m}$  in the z direction. The system capacitance at this deflection is  $0.289\text{pF}$  and the force in the z-direction is  $F_z=8.44\mu\text{N}$ . (D) The graph shows the Mises stress distribution through the mirror and spring structure, and high stress density occurs at mirror-to-spring and spring-to-fixed bank junctions as expected.

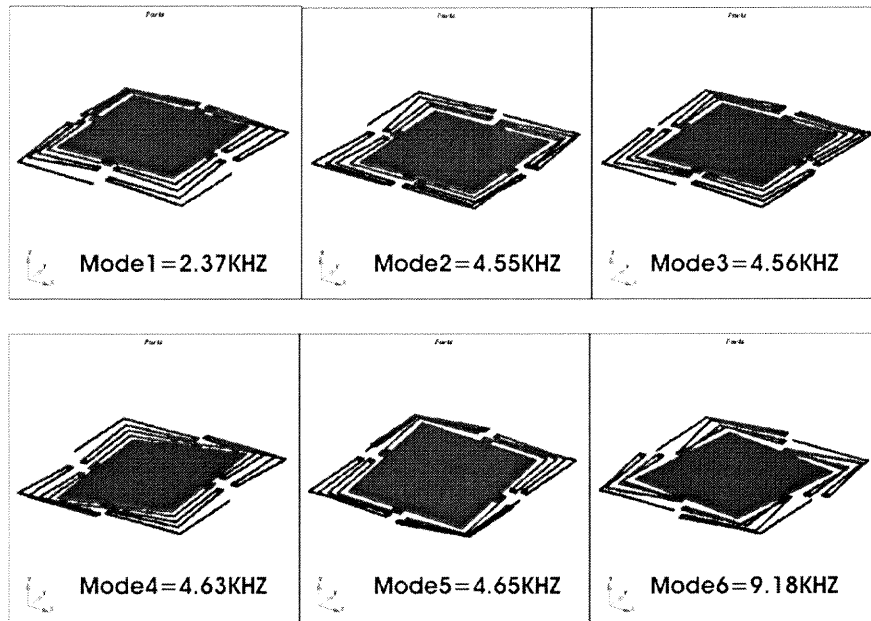


**Figure 3.13** Graph of the first 6 mode shapes of "4 spr-corner" device shows the lowest frequency at vertical bending mode, and the cornered spring configuration introduces torsion modes at higher order.

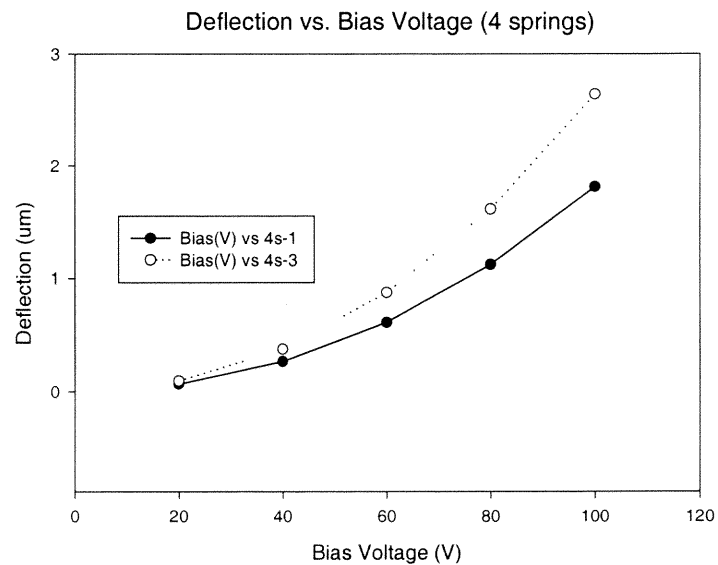


**Figure 3.14** The graph is electrostatic response of "4 spring-corner" device showing  $\sim 0.78\mu\text{m}$  piston-only deflection at  $\sim 50\text{V}$ , which corresponds to a full wavelength phase shift.

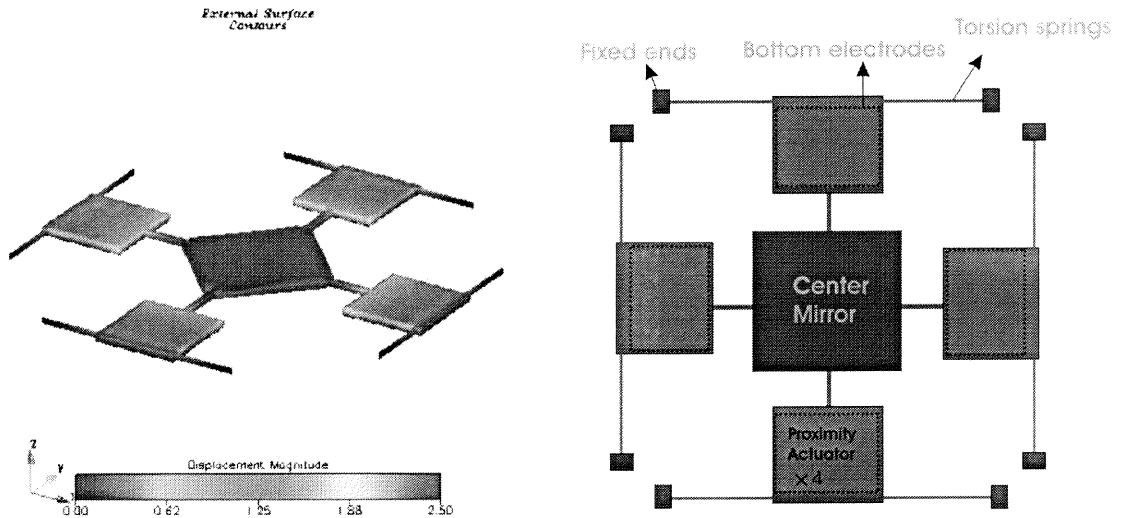


**Figure 3.15** Electrostatic response of “4 spring-corner” device showing a full wavelength phase shift at  $\sim 50\text{V}$ .

### 3.2.3 Mirror Tuning with Proximity Actuators

As shown in Fig. 3.15, the center movable mirror of the interferometer is not directly involved in the electrostatic actuation process, allowing significant optical coating design freedom. The four actuators are mechanically joined with the center mirror in such a way that the actuator displacement is transferred to the center mirror, or roughly speaking, the center mirror samples the tip deflection of the four torsion actuators. It should be noted that for small amplitude actuation, the four actuators are operating in a pure torsion mode, as can be illustrated by the shape graph of the loaded spring in Fig. 3.16.

A detailed visualization is illustrated as Fig. 3.16. The proximity actuators can assume two major roles: 1) control the motion of the center mirror if one voltage supply is applied to all of them; 2) adjust the parallelism and gap uniformity of the center mirror for optimized optical performance if two or more voltage sources are applied to the actuators. The downside of the 2<sup>nd</sup> function is that it needs multiple power supplies, and to do real-time adjustment, gap depth sensing may have to be integrated into the structure

to enable closed-loop control. It is suggested that for high accuracy light wavelength maneuvering, this embodiment can be used.

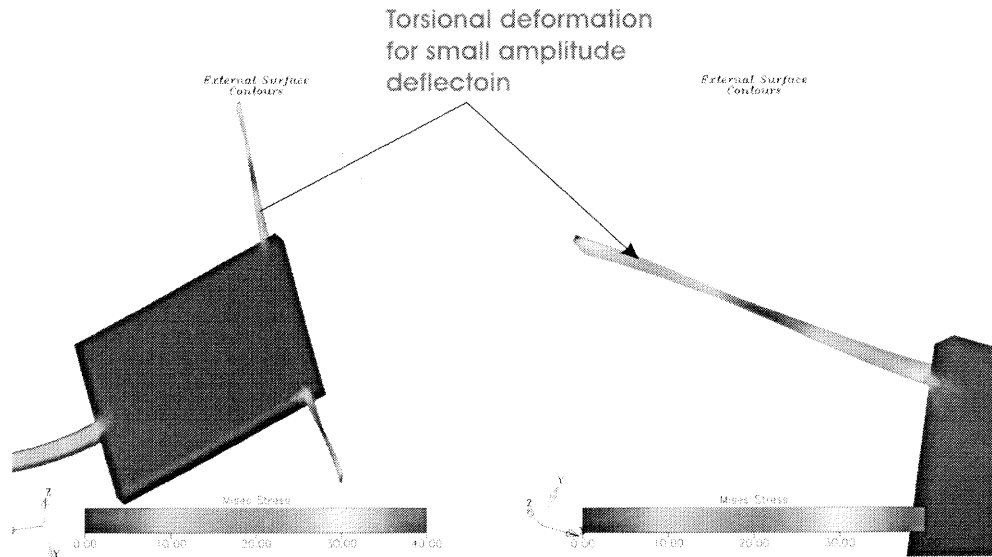


**Figure 3.16** Shape graph of the springs under electrostatic load for small amplitude deflection. The springs are mainly working in torsion mode such that the system pull in is increase from 1/3 to ~44%, which implies that further reduction of actuation voltage is possible by decrease the air gap depth of the actuators.

An extra advantage of using this actuation scheme is that the torsion actuator usually has a larger travel range as have been investigated in chapter 2, such that the driving efficiency of actuation voltage is relatively higher than the parallel plate actuator. This comparison is possible because to realize a real parallel plate using micromachining technology, considering the feature size and tolerance of fabrication, at least three suspending springs have to be mechanically linked to the movable mirror plate, while the torsion mirror usually needs only two springs to suspend the mirror plate. Roughly speaking, given the same air gap depth and identical effective actuation area, and the same spring thickness, width and length, the actuation voltage for a torsion actuator to achieve a certain tip deflection is comparatively smaller than that of the parallel plate actuator. The higher pull-in position of the torsion actuator enables a smaller gap depth,

given that an identical deflection is needed for light modulation. Gap depth reduction is the most sensitive and effective way to obtain low actuation voltage.

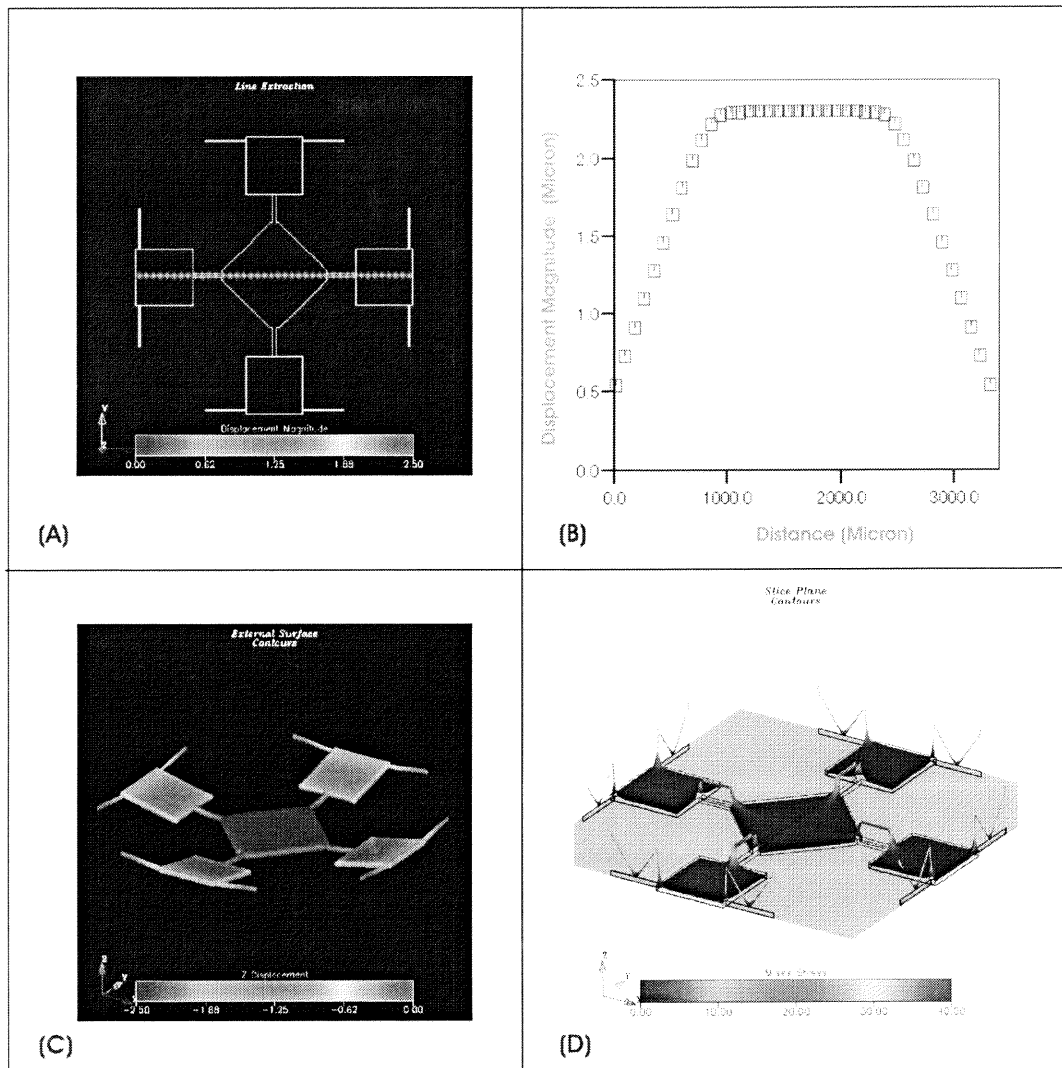


**Figure 3.17** (A) Sampling of the electrostatic actuated mirror, purple balls indicate sampling points. (B) The graph shows the deflection profile extracted from sampling points displayed in (A). (C) The graph illustrates the mirror behavior under 80V bias electrostatic load, showing a maximum displacement magnitude of 2.3  $\mu\text{m}$  in z direction. This maximum deflection is uniform across the whole area of the center mirror. (D) The graph shows the Mise stress distribution through the mirror and spring structure. The four beams at four corners of the center square mirror are operating at bending mode, and the springs linking 4 actuator plates to fixed ends are taking zigzag shape, implying that these springs are working mainly in the torsion mode.

### 3.2.4 Fast Prototyping by Silicon Wafer Bonding using SU-8 as Spacer

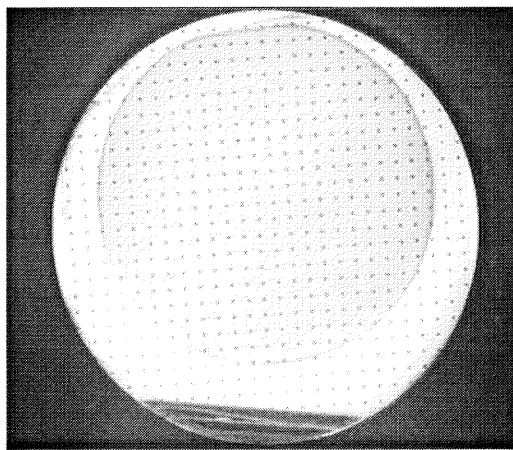
The above design investigation for electrostatic micro mirrors indicates the feasibility of the micro mirror technology by ultra-thin silicon wafer bonding and deep reactive etching technologies. The current section will discuss the technical availability of fabrication. In developing the fabrication processing steps, emphasis is on finding a fast prototyping process for the purpose of device concept verification.

To realize the Fabry-Perot tunable interferometer of the present research, a mirror flatness within  $\lambda/4$  or better is desirable, and non-parallel micromirror deformation has to be minimized. Deep reactive ion etching of bonded ultra-thin silicon wafers provides a technical option. The required flat mirror surface is obtained by using commercially available double-side polished silicon wafers, so no chemical mechanical polishing (CMP) is needed, enabling a cost effective fabrication. The low voltage requirement is met by deep reactive ion etching the ultra-thin wafer to produce the soft-spring-suspended mirror plate. Considering that wet-etching will roughen the optical reflection surface, an epoxy material SU-8 is uniquely adopted as a bonding layer and a spacer so that the original flatness and smoothness of the polished silicon surface is retained for optimized optical performance and operation.

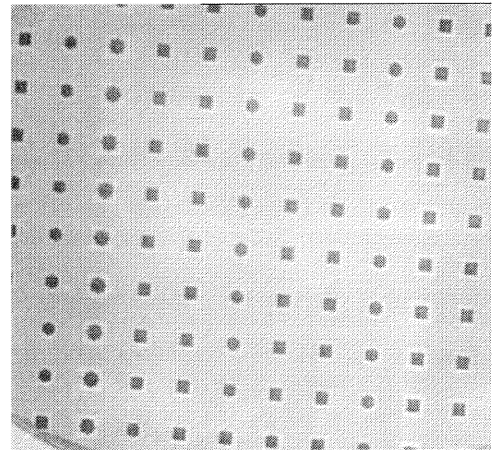
The SU-8 is a negative, epoxy-type, near-UV photoresist (365 nm). This photoresist can be as thick as 2 mm and aspect ratios up to 25 have been demonstrated with a standard UV-lithography [60-62]. The bondability was investigated by bonding a blank ultra-thin wafer onto a patterned SU-8 layer using a commercial (EVI) bonding machine. An external pressure load is applied uniformly on the wafer top after the bonding chamber is evacuated. Fig. 3.18 shows a sandwiched structure that is formed

using this bonding operation. The processing flow that includes using SU-8 as the interferometer spacer is sketched as Fig. 3.19. Major fabrication steps include 1) evaporation of optical coating stacks on both silicon wafers, 2) applying the SU-8 layer and patterning the mirror cavity, 3) wafer bonding, 4) metalization and 5) DRIE.

One of the keys to successful wafer bonding is the flatness and cleanliness of the wafer surfaces. Fig. 3.18(A) shows that the 3" ultra-thin wafer is well bonded to the SU-8 structure. Fig. 3.18(B) shows a close-up view of a region of the bonded wafers, confirming the good alignment and bonding between the well-defined structures and the silicon wafer as desired.



(A)



(B)

**Figure 3.18** (A) Patterned 3" ultra-thin Silicon wafer (50  $\mu\text{m}$ ) bonded to a patterned 4" Substrate having SU-8 structures. (B) Close-up of a region showing good alignment and bonding [63].

By successful bonding an ultra-thin silicon wafer to the patterned SU-8 structure, a novel method was demonstrated which can be used for a variety of optical MEMS applications. The success of the experiment confirms that SU-8 can be used as a spacer and a bonding medium. This encouraging result will most certainly help the MEMS research community seeking new low cost material to develop their prototypes and



processes.

The developed ultra-thin silicon wafer bonding approach using SU-8 as the bonding interface layer has enabled the fast prototyping of our tunable Farby-Perot interferometer. The combination of this approach with deep reactive ion etching technology leads to a fast prototyping method of electrostatic mirrors, as shown in Fig. 3.19. The parallel movable plate micro mirrors using the direct actuation scheme have been successfully prototyped. Fig. 3.20 shows a parallel mirror profile .

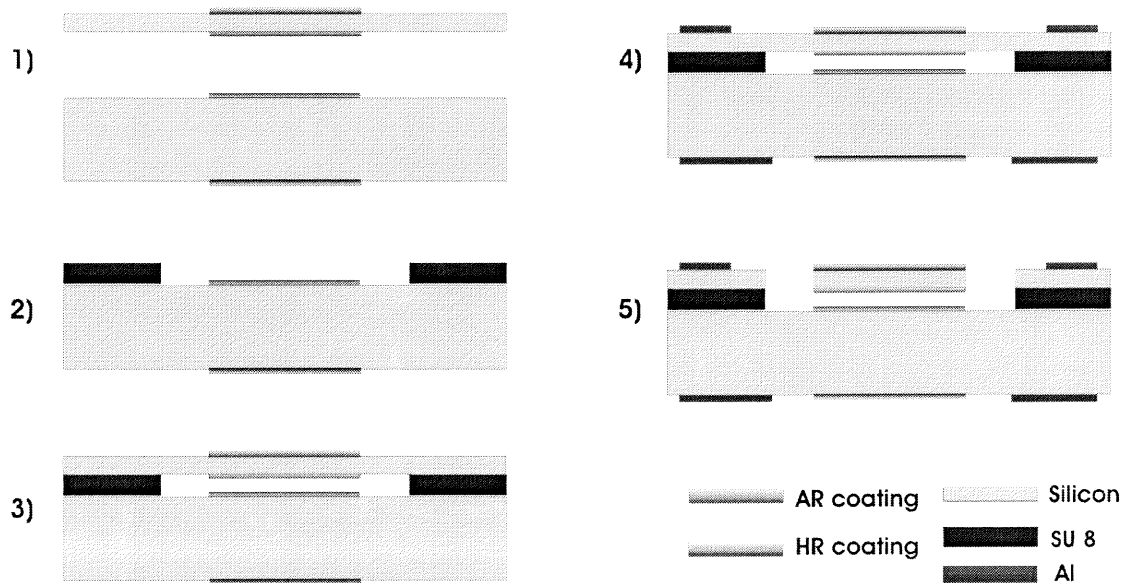
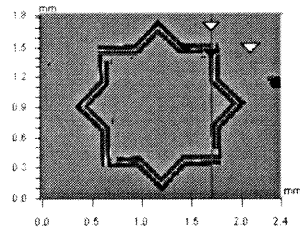


**Figure 3.19** Cross sectional view of mirror device fabricated through 5 major processing steps.

Veeco



X	1.70	-	-	mm
Y	1.44	-	-	mm
Ht	-61.36	-	-	um
Dist	-	-	-	mm
Angle	-	-	-	°

Title:

Note:

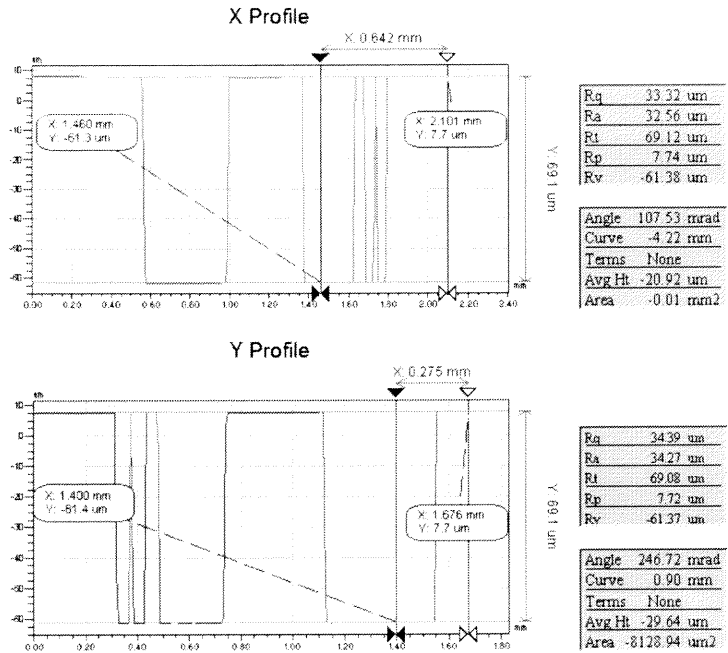


**Figure 3.20** Surface profile of a fabricated mirror structure using SU-8 as mirror spacer and bonding interface layer. [63].

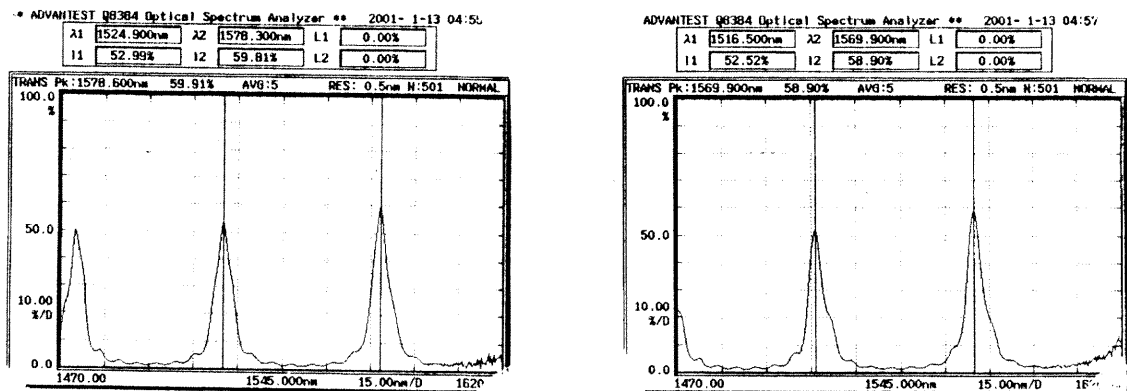


**Figure 3.21** Graph illustrating the optical performance at transmission mode for 0V and 40V biases [64]

### Tuning Behavior of FP Interferometer Device

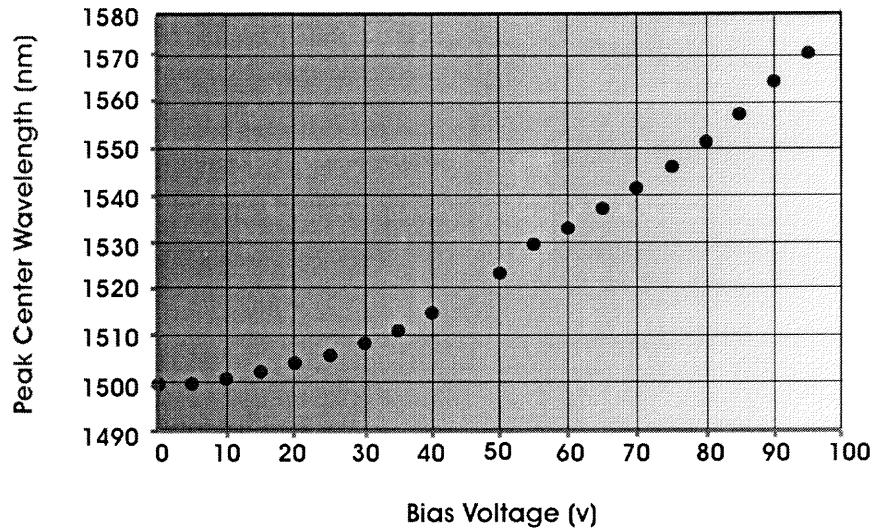


**Figure 3.22** Graph illustrating the optical performance at transmission mode from 0V to 100V biases for a mirror using 5 folded spring suspension.

### 3.3 Analysis of High Angular Deflection Torsion Mirror with Shaped Electrodes

The micromachined optical cross connect (OXC) is believed to be one of the most crucial and promising candidates to enable all optical DWDM networks [42]. MEMS optical switching has been demonstrated in the free-space scheme [41,43] by using microactuated free-rotating mirrors. These mirrors are presented in the form of an array or fabric that is monolithically integrated onto a silicon chip by means of surface micromachining fabrication techniques. The optical inputs from N fibers are collimated and directed to the mirror array, and then switched to the desired output port by the actuated rotation of a selected mirror. A successful optical cross connect mirror array has been fabricated using the MCNC MUMP's (multiuser MEMS process) fabrication process [65]. The core element of the optical cross connect sub-system is the micro free-standing mirror which is actuated electrostatically. To achieve the beam steering required by the sub-system, not only high angular motion of the 2-D mirror member has to be

analyzed, but also the reliability of the mirror material has to be improved. In this thesis, the proposed capacitance based theory are developed for mirror design and optimization. Various electrode shapes are investigated to for the purpose of providing extra design freedom. For mirror reliability, bulk micromachining of bonded ultra thin silicon wafers is proposed to be used to realize the single crystal micro mirrors. This improvement from polysilicon mirrors in MUMP's to single crystal silicon mirrors in silicon fusion bonding technology may benefit the mirror reliability when operated to steer beams.

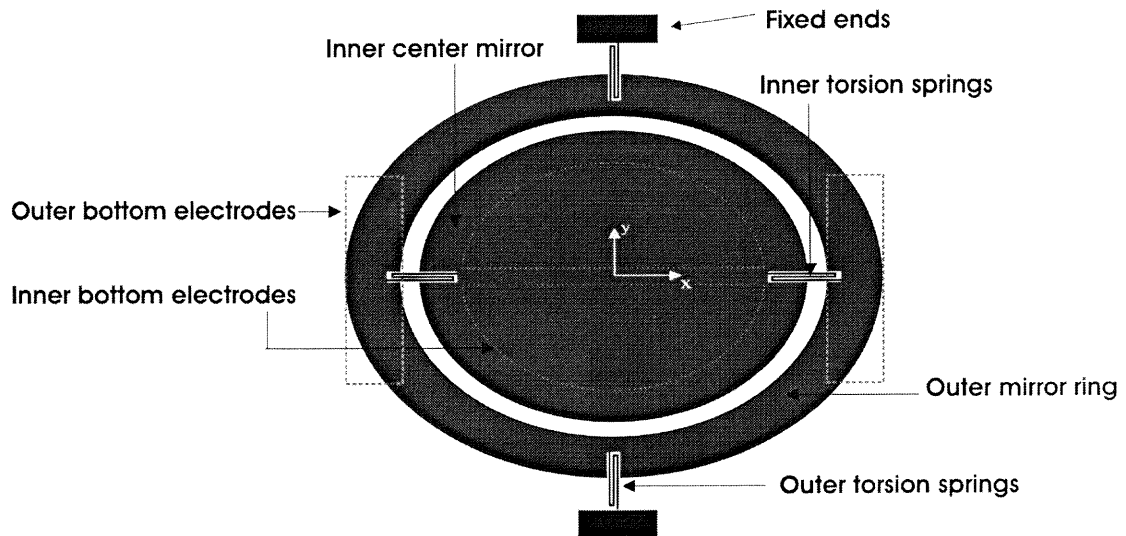


**Figure 3.23** Graph shows the typical layout of an 2D mirror with two rotational stages along the x and y axis, respectively. The mirror shape is investigated as elliptic and assumed to have a larger area than the bottom electrodes so that the actuation properties will mainly be determined by the shapes and sizes of the bottom electrodes.

The layout of a typical 2D single mirror is shown in Fig. 3.23 in which the inner center mirror is suspended by two inner torsion springs and the outer ring, supported also by another set of torsion springs (outer torsion springs), is used to rotate the center mirror about another axis (y axis). The two rotational stages of the center mirror are along the x and y axes, respectively. The mirror is investigated as an elliptic shape and assumed to have a larger area than the bottom electrode so that the mirror actuation curve is determined by the shape and size of the bottom electrode. The outer electrodes are placed

at the far end of the spring structure to reduce the actuation voltage for the y-rotation stage to an acceptable level. It should be noted that the designer is able to move outer electrodes closer to the outer springs in order to increase the travel range, but this would sacrifice the actuation voltage.

It would be necessary to study the static behavior of the circular shaped actuated mirror since it is widely used in optical MEMS systems. As has been illustrated in Chapter 2, as a special case of elliptical electrodes, the circular-shaped full-plate actuated mirror will have a normalized pull in of 48.3%, slightly larger than that using rectangular mirror plates (44%). A technical research issue is to investigate the effect of other electrode shapes on the pull in to find the most driving-voltage-efficient actuation scheme.

Now consider the effects of inner bottom electrode on the actuation characteristics of the center mirror. The actuator capacitances of various electrode shapes are plugged into the capacitive equations to find the pull in solution for the center mirror. For the full actuation scheme in which the bottom electrode and upper electrode on the half mirror plate have the same physical area, the pull in solutions for elliptical, hyperbolic and parabolic shaped electrodes have been obtained.

For the elliptical-shaped electrostatic torsion actuator, the shape of a full electrode can be described as:

$$\begin{aligned}x &= a \cos t \\y &= b \sin t\end{aligned}$$

where  $a$  and  $b$  are the semi major axis and semi minor axis, respectively, and  $t \in (-\pi/2, \pi/2)$ . The capacitance of the system is therefore:

$$C = 2\varepsilon \int_0^a \frac{y dx}{d - x\theta} = 2\varepsilon \int_{\pi/2}^0 \frac{b \sin t (-a \sin t) dt}{d - a \cos t \bullet \theta} = 2\varepsilon \int_0^{\pi/2} \frac{ab \sin^2 t}{d - a\theta \cos t} dt$$

The integrated result of the capacitance is

$$C = \left( \frac{2b\varepsilon \left( (0.5d\pi + a\theta)\sqrt{-d^2 + a^2\theta^2} + (2d^2 - 2a^2\theta^2) \text{ArcTanh} \left[ \frac{d + a\theta}{\sqrt{-d^2 + a^2\theta^2}} \right] \right)}{a\theta^2 \sqrt{-d^2 + a^2\theta^2}} \right)$$

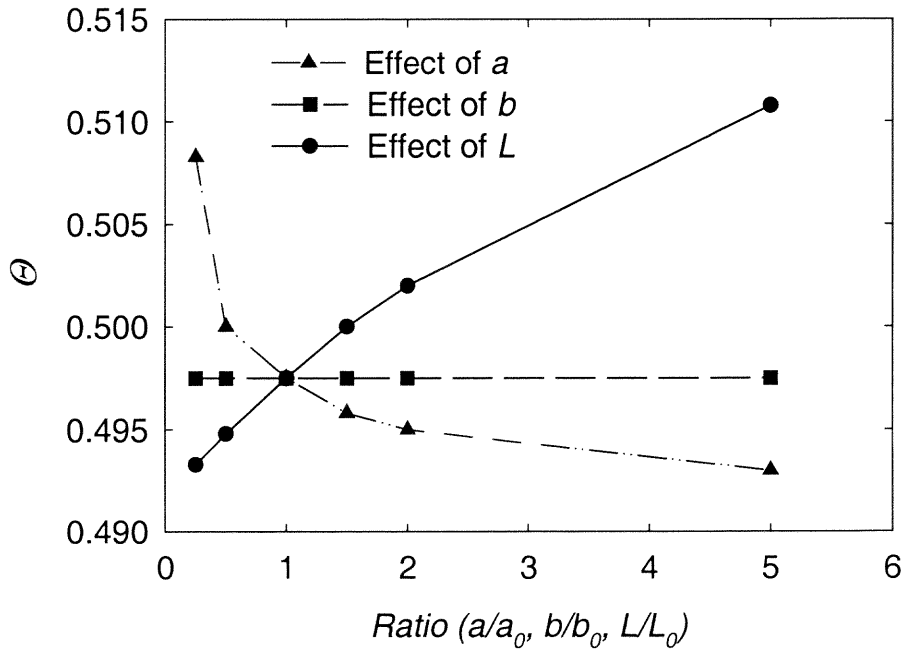


**Figure 3.24** Solution of unitless pull in position  $\theta$  of full hyperbolic electrode actuation under different ratios of  $a/a_0$ ,  $b/b_0$  and  $L/L_0$ .  $a_0$ ,  $b_0$  and  $L_0$  are reference semi axis and electrode length.

After applying the pull in equation to determine the pull in angle,  $\theta_{pin}$ , the unitless pull in angle,  $\Theta$ , and the actuation curve, it can be shown that for full elliptical electrodes,  $\Theta$  is 0.4833, which is independent of the semi-major axis  $a$  and semi-minor axis  $b$ , as shown in Fig. 3.25. For hyperbolic electrodes, the equations describing a hyperbola are

$$x = a / \cos t$$

$$y = b \tan t$$

where  $a$  and  $b$  are the semi-major axis and semi-minor axis, respectively. The capacitance of this actuator can be written as:

$$C = 2\epsilon \int_a^{a+L} \frac{y dx}{\left[ d - \left[ L - \left( \frac{a}{\cos t} - a \right) \right] \right] \theta} = 2\epsilon \int_0^\alpha \frac{ab \tan^2 t / \cos t}{d - \left[ L - a \left( \frac{1}{\cos t} - 1 \right) \right] \theta} dt$$

where  $\alpha = \text{Arc cos} \left[ \frac{a}{a+L} \right]$ . The integral of the capacitance expression can be obtained

using MATHEMATICA software, and the unitless pull-in angle,  $\Theta$  is plotted as Fig. 3.24. It shows that the semi axes  $a$ ,  $b$  and the electrode length  $L$  do affect the pull-in position. As  $a/a_0$  increases from 0.125 to 5,  $\Theta$  decreases from 0.508 to 0.493. And as  $L/L_0$  increases from 0.125 to 5, the pull-in position increases from 0.493 to 0.511.

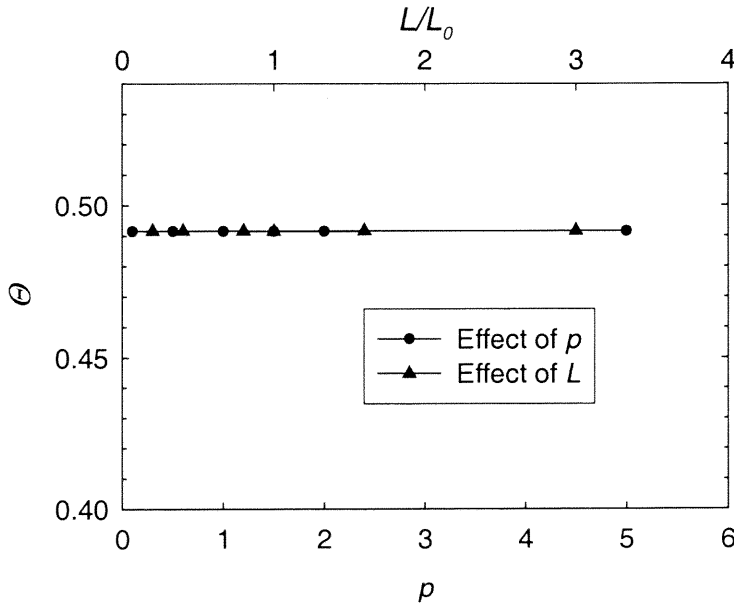


**Figure 3.25.** Effect of constant  $p$  and electrode length  $L$  on unitless pull in position  $\Theta$  of full parabolic electrode ( $y^2 = px$ ) actuation.  $L_0$  is the reference electrode length.

Now consider the effects of partial electrode actuation on system pull in. Partial electrode actuation refers to the actuation in which the length of the bottom electrode only covers part of electrode on the half center mirror, as shown in Fig 3.26.

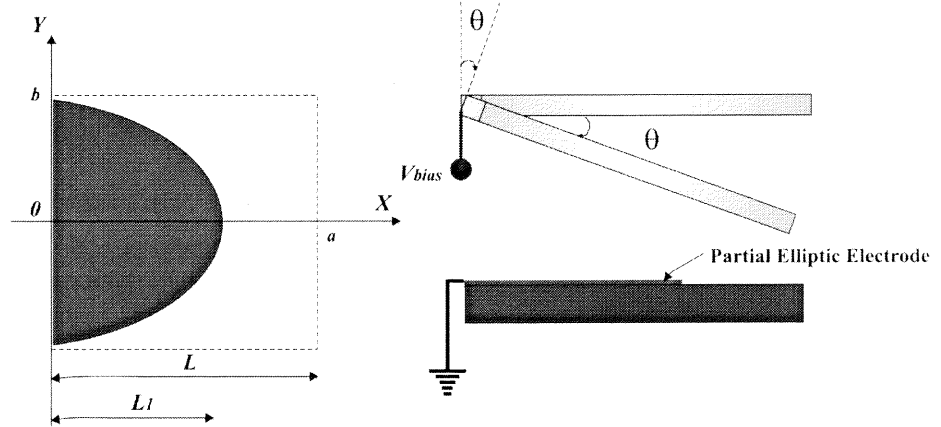


**Figure 3.26** Partial actuation scheme of elliptic-shaped electrode.

The effective area to evaluate the capacitance is only the electrode area if the fringe effect is negligible. For partial elliptical electrodes, the capacitance of this actuator system can be integrated by:

$$C = 2\epsilon \left[ \int_{\beta}^{\pi/2} \frac{ab \sin^2 t}{d - a\theta \cos t} dt + \int_0^{L_1} \frac{bx \sqrt{1 - \left(\frac{L_1}{a}\right)^2}}{L_1(d - x\theta)} dx \right]$$

where  $\beta = \text{Arc cos}(L_1 / a)$ . The unitless pull-in angle  $\Theta$  obtained is shown in Fig. 3.27. and the unitless pull in angle,  $\Theta$ , simulated by MEMCAD 4.8 is plotted also in Fig. 3.27. A circular electrode with radius of  $200\mu\text{m}$ ,  $d = 12\mu\text{m}$  is chosen as the base case and the  $\gamma$  value is changed from 0.43 to 1. Fig. 3.27 shows that the analysis and simulation results are in good agreement. The highest difference is about 3%.



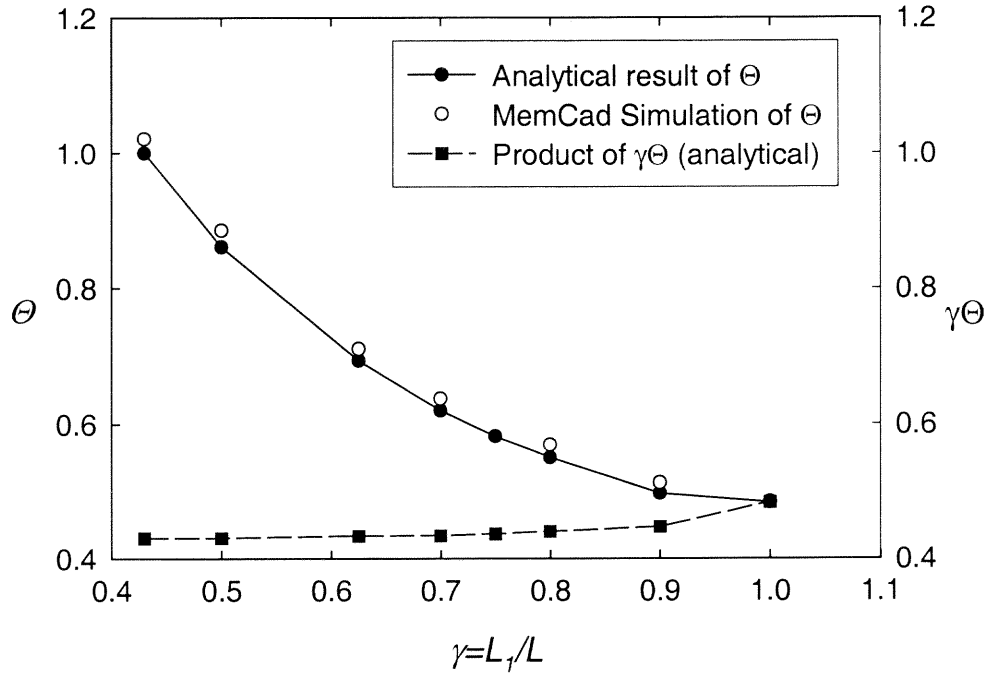


**Figure 3.27** Analytical unitless pull in position  $\Theta$  of cantilever rectangular torsion actuators with electrode located at the end near spring

Similarly for partial hyperbolic electrodes, the capacitance can be written as:

$$C = 2\epsilon \int_{\beta}^{\alpha} \frac{ab \tan^2 t / \cos t}{d - \left[ L - a \left( \frac{1}{\cos t} - 1 \right) \right] \theta} dt$$

where  $\alpha = \text{Arc cos} \left[ \frac{a}{a + L - L_1} \right]$ ,  $\beta = \text{Arc cos} \left[ \frac{a}{a + L} \right]$ . Applying the pull in equation

reveals that as  $L_1/L$  decreases from 1.0 to 0.448, the product of  $\gamma \Theta$  decreases from 0.497 to 0.448 as shown in Fig. 3.28, implying that this actuator could reach full travel range without pull in.

The above results show that the center mirror under partial actuation could achieve full travel range. However, the price is a sacrifice of applied voltage.

These results, obtained from applying various electrode shape and size schemes to

the capacitance-based equations, form a database of the electrostatic torsion mirrors for high angular deflection applications, though they are originally targeted for OXC mirror designs. Table 3.2 gives a summary of these pull-in solutions. It is strongly recommended here that future work be focused on identifying and comparing the efficiency of the driving voltage for these shaped-electrode actuation schemes.

**Table 3.2** Pull-summary of shaped electrode actuation scheme.

		$\Theta$	$\gamma\Theta$
Rectangular torsion		0.44	0.44
Elliptical torsion		0.4833	0.4833~0.43
Hyperbolic torsion		0.493~0.508	0.497~0.448
$y = px^n$	$n=0.5$	0.492	0.492~0.447
	$n=1$	0.5416	0.542~0.455
	$n=2$	0.558	0.638~0.475
	$n=6$	0.433	N/A

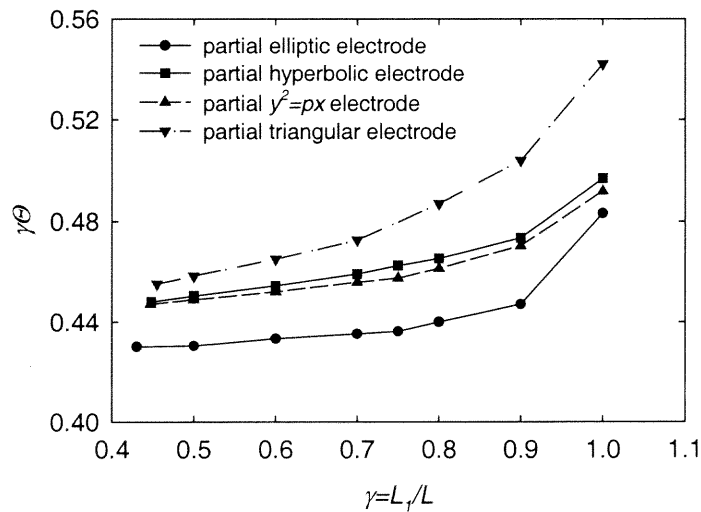


**Figure 3.28** Analytical unitless pull in position  $\Theta$  of partial elliptic, hyperbolic, triangular and parabolic ( $y^2 = px$ ) results.

### 3.4 Device Concept of Resonant Beam True Mass Flow Sensor

#### 3.4.1 Introduction

The performance of Coriolis mass flow sensors is independent of flow profiles and properties such as composition, pressure, temperature, flow density, viscosity and homogeneity. Conventional Coriolis mass flow sensors have been developed for liquid and gas applications but they are expensive in cost, and deficient in manipulating micro fluids due to their large volumes. The first micromachined Coriolis mass flow sensor has been prototyped with no integrated vibration pickup [66]. The state of the art of micromachined Coriolis mass flow sensor research is to commercially realize high sensitivity, high stability true mass flow measurement with an on-chip integrated signal conditioning circuit.

The objective of the current research is to preliminarily design a high-sensitivity Coriolis mass flow sensors for gas and liquid applications. Three types of Coriolis mass flow sensors are classified by signal detection and read-out techniques: piezoresistive, capacitive and resonant beam, while the innovative aspect of current thesis work lies on the innovative use of a resonant beam as the vibration pick-up for the Coriolis force, and hence the mass flow rate measurement. This innovation is initiated by focusing on a feasibility study which is detailed as device concept (section 3.5.1), mode analysis (section 3.5.2) and resonant beam-to-string transform (section 3.5.3).

A resonant beam Coriolis mass flow sensor involves three vibrations. The 1<sup>st</sup> vibration is actuated externally with the lowest tube torsion resonant frequency depending on flow density. The 2<sup>nd</sup> vibration, introduced by the Coriolis force, is an induced bending mode, and the Coriolis force is given by  $F_C = -2M_f \vec{V}_f \times \vec{\omega}_1$  where

$M_f \vec{V}_f$  is the mass flow momentum and  $\bar{\omega}_1$  is the angular frequency of the 1<sup>st</sup> torsion vibration. Periodic  $\bar{\omega}_1$  leads to a periodic Coriolis force imposed in the orthogonal direction of 1<sup>st</sup> vibration, causing the elastic structure to undergo a 2<sup>nd</sup> vibration which, orthogonal to the 1<sup>st</sup> one, is operating in bending mode of the tube structure. The measurement of mass flow now becomes the measurement of the peak amplitude of the 2<sup>nd</sup> vibration. As shown in Fig. 3.29, the beam of the 3<sup>rd</sup> vibration is fixed with both ends on the tubes, sampling the displacement of the 2<sup>nd</sup> vibration. As a result, the beam is periodically stretched or compressed. The resonant frequency of the beam under this periodic strain will have a periodic shift so that the detection of this frequency shift becomes the measurement of the 2<sup>nd</sup> vibration amplitude, hence a measurement of the mass flow.

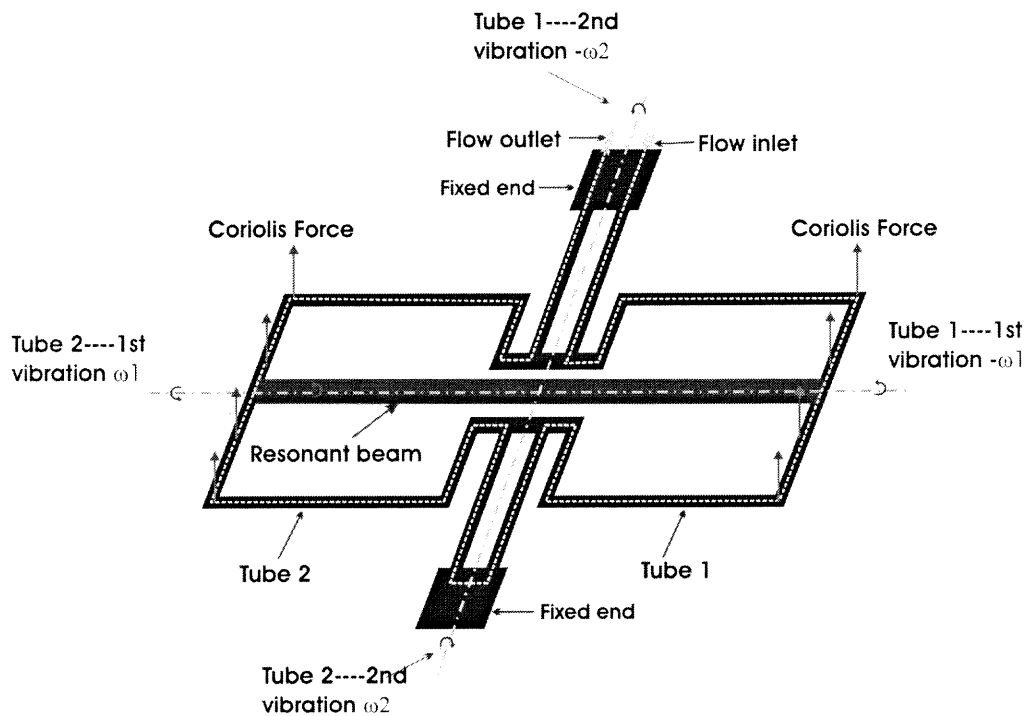
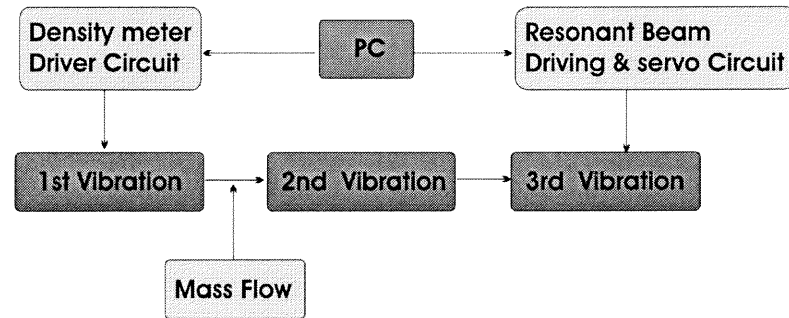


**Figure 3.29** A schematic graph showing the operational principle of mass flow measurement using resonant beam vibration pick-up scheme.

As explained above, Fig. 3.29 indicates the principle of device operation. Fig. 3.30 is a block schematic showing the device operation under motional fluid load and external driving signal loads, while Fig. 3.31 is a 3D solid view of the device showing the fabrication layers and electrode configurations.



### System Schematic of Resonant Sensors

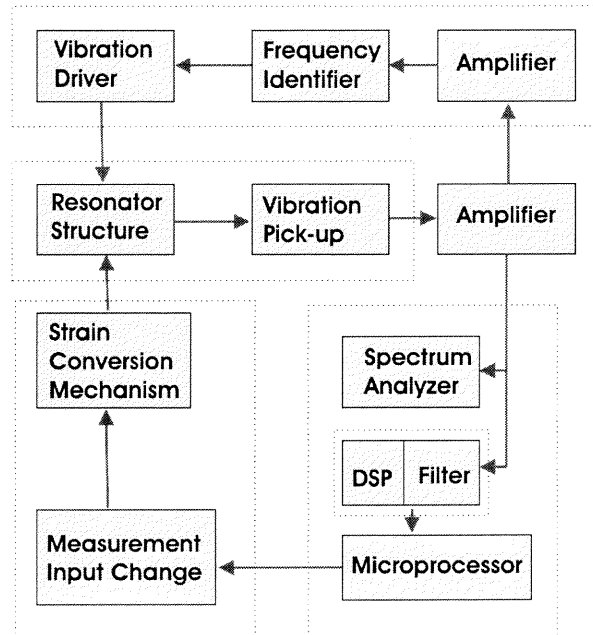


**Figure 3.30** A block diagram illustrating the relationship among the three vibrations of the device.

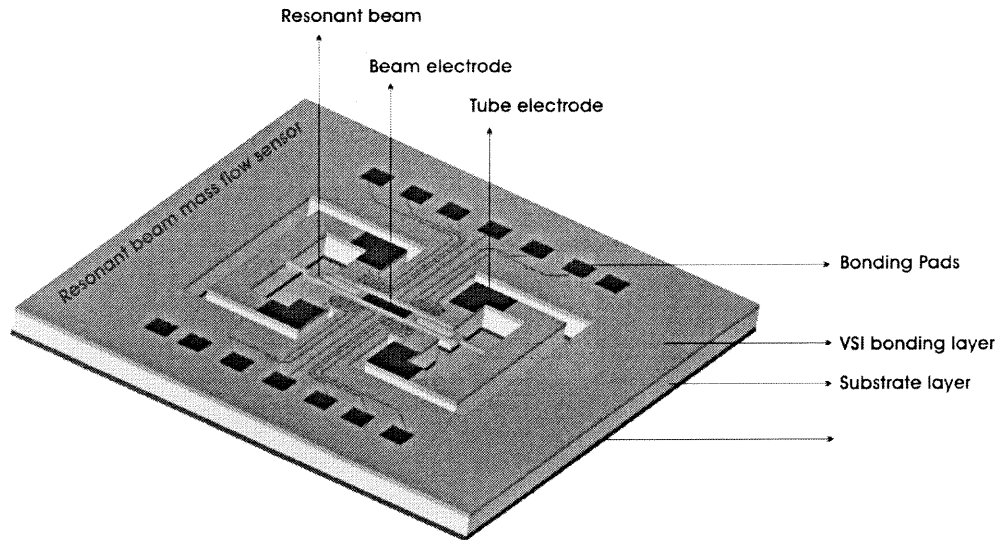


**Figure 3.31** A 3D solid view of the device showing the fabrication layers and electrode configurations.

### 3.4.2 Mode Analysis

Emphasis is put on double-loop structures since this configuration increases the quality factor of the sensor by enabling an energy conversion between the two single loops and minimizing energy dissipation to the supporting structure. The mode dependence on device size is investigated. In-phase bending (mode2) and out-phase torsion (mode5) are complementary vibrations and are used as the 1<sup>st</sup> and 2<sup>nd</sup> vibrations of the sensor respectively. Out-phase bending (mode1) and in-phase torsion (mode6) are also complementary.

It shows in Fig. 3.32 that the mode shapes of the 9 lowest orthogonal vibrations, with natural frequencies shown in Fig. 3.33 for six different device sizes.

The device operation prefers complementary vibrations (mode2 and mode5) in the view of energy conversion. The 1<sup>st</sup> vibration is actuated electrostatically, and when flow is present in the tube, the periodic Coriolis force leads to the 2<sup>nd</sup> vibration of the system. The information of mass flow is enclosed in the peak amplitude of the 2<sup>nd</sup> vibration and

its effective actuation demands frequency matching between the two complementary modes. Our simulations show that the ratio ( $\omega_2/\omega_5$ ) ranges from 0.58 to 0.75. Design optimization is being undertaken currently to increase frequency ratio to above 0.9.

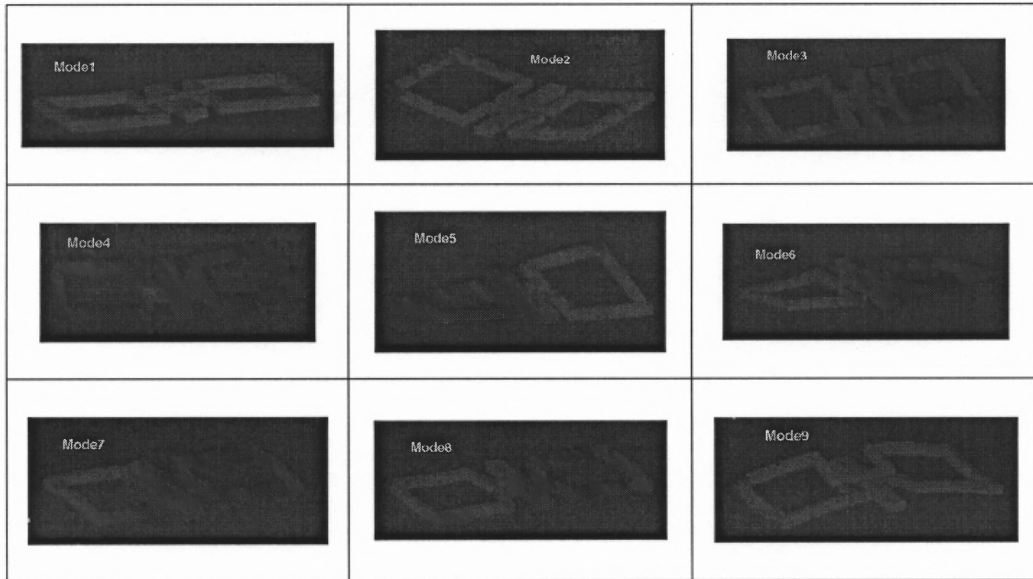


**Figure 3.32** Mode shapes for the double-loop structure

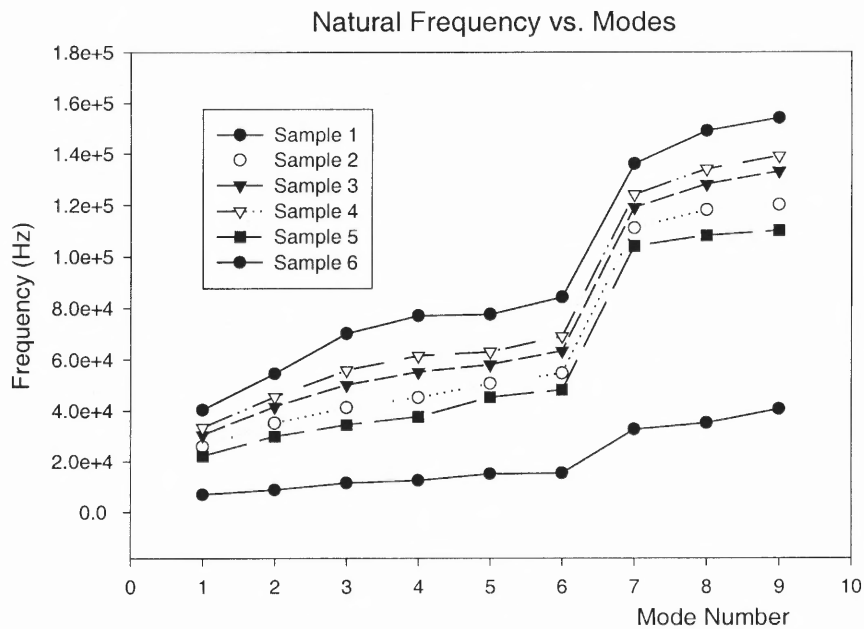


**Figure 3.33** Natural frequency vs. mode number for double loop structures with various dimensional sizes.

Both vibrations have density dependence (or mass dependence), so the device can be used as density meter [67, 68, 69]. The simulated frequency dependence on density is given in Fig. 3.34 and Table 3.3.

**Table 3.3** Mode frequency dependence on material density being measured (Device Sample 6)

Density (Kg/m <sup>3</sup> )	Mode 1	Mode 2	Mode 3	Mode 4	Mode 5	Mode 6
0	6937.4	8790.3	11496.0	12490.0	15079.9	15447.6
500	6332.9	8024.4	10494.0	11402.0	13766.0	14101.7
1000	5863.2	7429.1	9715.9	10556.0	12744.9	13055.6
1100	5781.2	7325.2	9580.0	10408.0	12566.7	12873.0
1200	5702.5	7225.6	9449.6	10266.9	12395.7	12697.9
1300	5627.0	7129.9	9324.5	10130.9	12231.5	12529.7

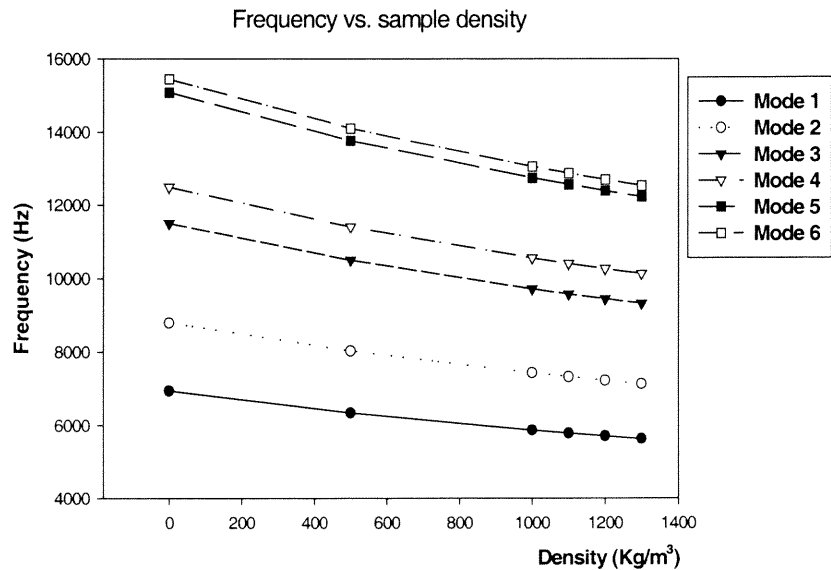


**Figure 3.34** Mode frequency dependence on material density being measured (Device Sample 6)



### 3.4.3 Beam-to-String Transform

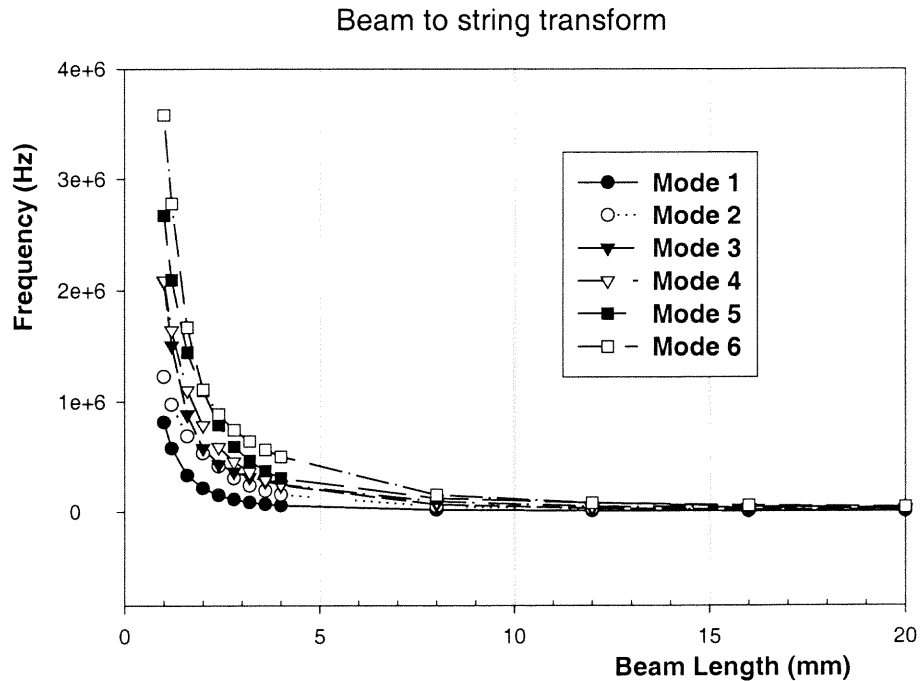


**Figure 3.35** The mode frequency variation due to changes of beam length.

The peak amplitude of the Coriolis force-induced 2<sup>nd</sup> vibration can be detected by the resonant beam method. The resonant beam is electrostatically actuated to vibrate in its lowest mode. The Coriolis-induced periodic motion causes the beam to be compressed and stretched periodically. This periodic strain changes the natural frequency of the beam. By detecting the frequency change, structure strain due to the 2<sup>nd</sup> vibration is obtained.

The double loop structure designed for the current mass flow measurement is comparably larger than ordinary MEMS devices so the incorporated resonant beam has larger dimensions. A critical design factor in using a resonant beam as a strain gage is the

large frequency difference between structure vibrations and beam vibration, otherwise the beam vibration will be coupled with structure vibrations, introducing systematic measurement error. Simulation effort was undertaken to find the beam frequency dependence on dimensions. Fig. 3.35 shows curves for a simulated beam (width=500 $\mu\text{m}$ , thickness=100 $\mu\text{m}$ ), the beam length changes from 1000~20000 $\mu\text{m}$ . The beam to string transform is obvious. The linear section (Length > 5mm) is the string region.

## CHAPTER 4

### CONCLUSIONS AND DISCUSSION

This thesis work includes three parts:

(1) Capacitance-based quasi-static analytical theory

A generalized theory and method are proposed through capacitance-based differential equations for the static analysis and design of electrostatic micro actuators. The advantage in using the capacitance-based approach is that it avoids the complicated force analysis and is most suitable for the analysis of complex micro actuator systems in which the usual force method is not straightforward. The resulting general displacement and voltage parameters are normalized with respect to their pull in values, yielding a general unitless structural equation valid for electrostatic actuators. A design theory is developed, based on the capacitance approach, and has been used to examine various actuators to determine pull in solutions and actuation curves. Using the capacitance-based approach, system pull in is investigated for the first time for non-deformable microactuators with variously shaped-electrodes and a range of fill factors. The approach is also used to provide explorations of the effect of fringing field capacitance, analysis of actuator systems with non-constant spring stiffness, and investigation of actuator systems with multiple capacitor elements.

A database is constructed for many actuation schemes that can be used as a guideline for the designers of electrostatic actuators. For full elliptical electrodes,  $\Theta$  is 0.4833, independent of the semi-major axis  $a$  and semi-minor axis  $b$ . For Torsion actuators with general power function shaped electrodes (generally described using the

function  $y = px^n$ ), the pull in angle is found to be 0.542 for  $n=1$ . If  $n = 2$ ,  $\Theta$  is found to be a constant of 0.638, and if  $n = 0.5$ ,  $\Theta$  is 0.492. These pull in constants are independent of  $p$  and electrode length of  $L$ . When  $n \in [0, \infty]$ , it has been shown that as  $n$  increases from 0.5 to 6,  $\Theta$  linearly increases to full travel range. The constant  $p$  of the power function does not affect the pull-in position. For hyperbolic electrodes, the semi major and minor axes,  $a$  and  $b$ , and the electrode length  $L$  do affect the pull-in position. As  $a/a_0$  increases from 0.125 to 5,  $\Theta$  decreases from 0.508 to 0.493. And as  $L/L_0$  increases from 0.125 to 5, the pull-in position increases from 0.493 to 0.511. For partial actuation using these variously shaped electrodes, the relation  $\gamma\Theta = \text{Const}$  is given for all cases, providing a design reference. Including the effects of fringing fields leads to a slight increase in the pull in displacement. Including a nonlinear spring stiffening term shows that pull in displacement may be greatly increased when that term is dominant.

It is suggested that future work should be focused on comparing the driving efficiency of these different actuation schemes, so that designers will be able to choose the most driving-voltage effective scheme for a specified application. Additional future work should focus on applying the capacitance based theory to solve deformable actuator systems in a more systematic manner in order to construct design guidelines or a database for membrane-based and clamped beam-based actuators. These deformable systems will play an increasingly important role in innovative optical MEMS systems.

## (2) Methods for travel range extension

The two passive methods have been proposed in this thesis to introduce negative feedback and extend actuator travel range directly in the *electrostatic* domain. These methods are passive in that no external closed loop feedback control is employed. The

first method utilizes a series capacitor to modulate the effective actuation voltage across the variable capacitor. The resulting voltage across the actuator exhibits a maximum value at a specific applied bias, beyond which it begins to drop even though the charge density keeps increasing to give an increased electrostatic torque. The effect of this decreasing voltage is to delay the increase of electrostatic torque so that the restoring elastic torque can balance it at an expanded travel range. Two typical micro mirror structures: out-of-plane vertical and torsion mirrors, are used to verify this concept. The mathematical analysis of the series capacitor loop model has been presented, and simulation results obtained using the CoSolver feature of Memcad<sup>TM</sup> software have been compared with analytical results with good agreement.

The second method utilizes negative feedback due to coulombic repulsion between the net oxide charges that exist in two oxide layers placed between the actuator electrodes. An extra repulsive electrostatic torque is superimposed on the attractive electrostatic torque to retard the increasing rate of the total electrostatic torque in such a manner that a negative feedback mechanism is introduced into the actuator structure that enables the elastic torque of spring structure to balance the electrostatic torque at an expanded travel range up to 62% of full scale deflection. This increased travel range occurs at the expense of an increased bias voltage.

The travel range extension methods using geometrically shaped electrode with different fill factors can be clearly identified as a result of this thesis. These methods, together with mechanically elastic approaches such as strain-stiffening, should be systematically investigated in future work so that a driving efficiency implementation scheme can be built as an electrostatic design guide.

### (3) Fast design and prototyping of novel OMEMS devices

Three state-of-the-art application systems: variable optical attenuators (VOA), high angular torsion mirror systems for the optical cross connect fabric (OXC) and electrostatic tunable wavelength selecting devices are designed using the proposed design theory, and finite element analysis simulation is used for design verifications. Variable optical attenuator (VOA) and electrostatic tunable wavelength selection devices are built using fast prototyping ultra thin wafer bonding and deep reactive etching (DRIE) technologies. Both silicon wet-etching and SU-8 patterning are investigated for the formation of mirror gaps. Mechanical testing and partial device characterization in the optical domain is provided for these devices, revealing that the designed mirrors, after being fabricated by the ultra thin silicon wafer bonding technology, can operate in an expected manner. These fast prototyped devices have been used to identify design rules for optimized optical performance. Future work should include testing the prototyped devices and investigating failure mechanisms.

Finally, as a demonstration that the actuator design approach developed in this thesis can be applied to systems other than micromirrors, the approach is used to design an innovative true mass flow sensor using an electrostatic resonant beam as the sensing element. For this novel device, future work includes using ultra thin wafer bonding technology, combined with deep reactive ion etching technology, to fabricate the device, and testing it in a microfluidic manipulation platform to compare its performance with the predictions of this thesis.

## APPENDIX

### PUBLICATIONS AND MANUSCRIPTS

Attached are some of my previous papers that contain more detail and depth information about some topics in this thesis.

Xingtao Wu, Richard A Brown, Smitha Mathews and K.R. Farmer,  
“The Effects of Oxide on the Travel Range Extension of Electrostatic Micro Mirror”, OMEMS 2000, IEEE, pp.198-199.

Xingtao Wu, ZhiXiong Xiao, Jiang Zhe and K.R. Farmer,  
“Two Passive Methods to Extend the Travel Range of Electrostatic Micro Actuators”,  
Technical Proceedings of the MSM 2001 International Conference on Modeling and Simulation on Microsystems, pp. 342-346, Hilton Head Island, March 21-24, 2001.

Xingtao Wu, Jiang Zhe, Jingshan Wang, Jin Cheng, Vijay Modi, and K. R. Farmer,  
“A generalized capacitance-based model for the quasi-static description of electrostatic micro-actuators”, Submitted to IEEE Transaction on Journal of MEMS

S. K. Sampath, L. St. Clair, Xingtao Wu, D. V. Ivanov, Q. Wang, C. Ghosh and K. R. Farmer,  
“Rapid MEMS Prototyping using SU-8, Wafer Bonding and Deep Reactive Ion Etching”, Proceedings of 13<sup>th</sup> Conference of UGIM, June, 2001, pp.158-161.

Zhixiong Xiao, Xingtao Wu, Wuyong Peng and K. R. Farmer,  
“An Angle Based Design Approach for Rectangular Electrostatic Torsion Actuators”,  
accepted by IEEE Transaction on Journal of MEMS.

## **EXTENDING THE TRAVEL RANGE OF ELECTROSTATIC MICRO-MIRRORS USING INSULATOR COATED ELECTRODES**

Xing-tao Wu, Richard A. Brown, Smitha Mathews and K. R. Farmer

Microelectronics Research Center, New Jersey Institute of  
Technology  
University Heights, Newark, NJ, 07102-1982, USA

***Abstract*—** The use of oxide coated inner surfaces in full-plate, electrostatically actuated silicon micro-mirrors is investigated. At the expense of increased applied bias, oxide charge and capacitance combine to expand the travel range of the mirrors before snap-down.



# EXTENDING THE TRAVEL RANGE OF ELECTROSTATIC MICRO-MIRRORS USING INSULATOR COATED ELECTRODES

Xing-tao Wu, Richard A. Brown, Smitha Mathews and K. R. Farmer

Microelectronics Research Center, New Jersey Institute of Technology  
UNIVERSITY HEIGHTS, NEWARK, NJ, 07102-1982, USA

## 1. Introduction

Micromachined, electrostatically actuated mirrors can be used as variable attenuators, modulators and switches in optical networking systems [1,2]. Fundamental issues such as the trade-off between extended travel range and low pull-in voltage need to be addressed in order to provide increased design freedom for customized applications. In theory, the maximum travel range before snap-down for full-plate electrostatic actuators is 44% of the full-scale deflection[3]. Leveraged bending and strain stiffening have been examined to extend this range [4].

This paper reports the effects of using silicon dioxide coated inner surfaces in electrostatic micro-actuators. The oxide capacitance acts as a voltage divider, lowering the effective actuation voltage across the gap of the mirror structure, *i.e.*, increasing the total bias required to attain a particular deflection. Also, oxide charge on each electrode acts in parallel with the electrostatic attraction, in the case of similarly charged electrodes decreasing the effective actuation voltage, but increasing the travel range before snap-down. In addition, the oxide functions to inhibit both stiction and electrode shorting at snap-down.

Figure 1 shows our torsion micro-mirror schematically.

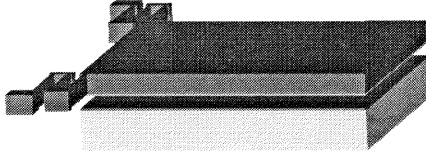


**Figure 1.** Silicon micro-mirror structure with a top cantilever held by two three-beam torsion springs, and a full plate bottom electrode. Springs with one, two and three beams have been fabricated. The inner surfaces of each electrode are coated with silicon dioxide and the top surface with Cr/Au. Dimensions are listed in Table 1 for one-beam (C3) and three-beam (D3) mirrors.

## 2. Device Analysis

In the region of stable operation and in the absence of oxide coated inner surfaces, the moment equation  $M(\theta) = K_\theta \theta$  determines the balance between electrostatic and elastic restoring torques. This equation is solved to find the actuation voltage dependence of deflection angle. Considering the effects of the added oxide layers, the equation becomes:

$$\sigma^2 \cdot M^{(A)}(\theta) - M^{(R)}(\theta) = K_\theta \theta \quad (1)$$

where  $M^{(A)}(\theta)$  and  $M^{(R)}(\theta)$  are electrostatic attractive and repulsive torque respectively, and  $\sigma$  is a modification factor due to the oxide capacitance:

$$\sigma = \frac{2d - L\theta}{2d - L\theta + \left( \frac{4t_{ox}}{\epsilon_{ox}} \right)} \quad (2)$$

The pull-in angle and voltage are determined using

equation 3, since the two intersection points of the spring and electrostatic equations coincide at pull-in:

$$\left( \theta \cdot \frac{d[\sigma^2 \cdot M^{(A)}(\theta)]}{d\theta} - \sigma^2 \cdot M^{(A)}(\theta) \right) - \left( \theta \cdot \frac{dM^{(R)}(\theta)}{d\theta} - M^{(R)}(\theta) \right) = 0 \quad (3)$$

Numerical approximation by expansion techniques and finite element analysis simulation are used to find the solutions for equations 1 and 3.

## 3. Fabrication and Dimension Verification

Bulk, anisotropic etching (with KOH) was used to form cavities in 4-inch, n-type, low resistivity ( $\sim 0.001$ - $0.01$  ohm-cm),  $\langle 100 \rangle$  silicon substrate wafers. Both the substrate wafers and ultra-thin, low resistivity ( $\sim 1$ - $10$  ohm-cm) silicon wafers,  $\sim 75$   $\mu\text{m}$  thick, were wet oxidized in the same furnace to a thickness of  $\sim 1$   $\mu\text{m}$ . Pairs of wafers were mated in vacuum, then annealed in oxygen to fusion bond the oxide layers and form sealed cavities. The ultra-thin top wafer was subsequently thinned by wet etching to  $\sim 50$   $\mu\text{m}$ , then patterned, allowing the mirror and spring structures to be formed by inductively coupled plasma deep reactive ion etching through to the underlying oxide. Finally,  $\sim 100$  nm of Cr/Au was deposited on the mirrors by physical vapor deposition. An array of mirror patterns was created, with mirror dimensions ranging from 400 to 700  $\mu\text{m}$  and spring widths from 5 to 10  $\mu\text{m}$ . Figure 2 shows SEM images of a completed device (D3) [2].

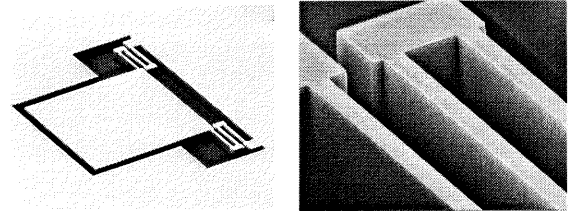


**Figure 2.** SEM images of a fabricated micro-mirror device (D3).

Table 1 lists the dimensions for the two mirror sizes used in this investigation, D3 and C3. Accurate dimensions were determined using optical profilometry.

DIMENSIONS ( $\mu\text{m}$ )	D3 (3-beam springs)	C3 (1-beam springs)	OTHER PARAMETERS
$W_{\text{mirror}}$	700	600	$G=0.73 \times 10^5 \text{ MPa}$
$L_{\text{mirror}}$	680	580	$\epsilon_0=8.85 \times 10^{-12} \text{ F/m}$
$t_{\text{mirror}}$	48.6	48.6	$\epsilon_{\text{ox}}=3.85$
$d_{\text{gap}}$	6.96	6.96	$Q_{\text{ox}}=6 \times 10^{10} \text{ /cm}^2$
$W_{\text{beam}}$	10	10	$t_{\text{ox}}=1.0 \mu\text{m}$
$L_{\text{beam}}$	$3 \times 200$	$1 \times 350$	
$t_{\text{beam}}$	48.6	48.6	
Stiffness ( $\mu\text{N}/\mu\text{m}$ )	$3.382 \times 10^6$	$4.428 \times 10^6$	

Table 1. Summary of mirror parameters.

It can be seen in Figure 3a that the device has a small upward deflection at zero bias (a maximum of  $\sim 200$  nm for the D3 device). Because of the thick top silicon electrode,

this deflection cannot be attributed to stress from the Cr/Au deposition. Optical profilometry at pull-in confirms a 6.96  $\mu\text{m}$  gap depth as shown in Figure 3b.

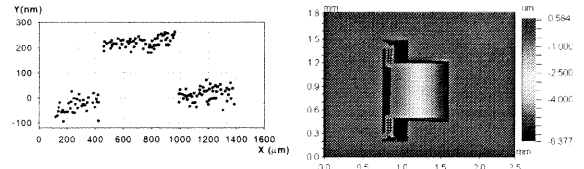


**Figure 3(a).** Maximum deflection at zero bias. **Figure 3(b).** WYKO optical profile of a D3 device at pull-in,  $V_{\text{bias}}=55\text{V}$ , indicating good flatness of the mirror surface.

## 4. Net Oxide Charge

The introduction of net oxide charge into an otherwise charge free system will cause a parallel shift of the capacitance-voltage,  $C-V_G$ , curve by an amount  $-Q/C_{ox}$ . As shown in Figure 4, a  $C-V$  curve measured at 1 KHz shows a positive flat band voltage shift, indicating a net negative oxide charge. This is typically expected of wet oxides with the usual water-related traps. The  $C-V$  was measured on  $3\text{mm} \times 3\text{mm}$  chips. The resulting capacitance is the parallel sum of the mirror capacitance, which has  $2\text{ }\mu\text{m}$  of oxide dielectric and a  $6.96\text{ }\mu\text{m}$  air gap at  $\sim 0\text{ V}$ , and the capacitance of the surrounding chip area, which has a  $2\text{ }\mu\text{m}$  oxide dielectric without an air gap. This parallel sum is essentially the capacitance of the surrounding chip area alone, but it nonetheless provides a measure of the quality of the oxide between the mirrors since the oxide in both regions is the same. The net charge in these oxides is easily controllable by temperature and oxidation ambient conditions. From the data, the net oxide charge density is calculated from the flat band shift to be  $\sim 3 \times 10^{10}/\text{cm}^2$  per oxide, in good agreement with the charge required to cause the initial deflection shown in Figure 3a,  $\sim 1 \times 10^{10}/\text{cm}^2$ .

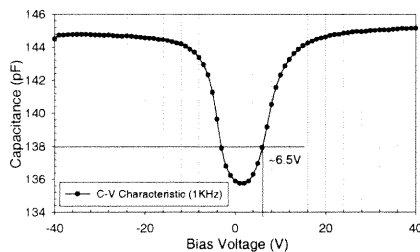


**Figure 4.**  $C-V$  curve at 1KHz, indicating a 6.5V shift.

## 5. Simulation and Experimental Results

Numerical approximation by the expansion technique and finite element analysis simulation using commercial MemCad 4.6 software were used to find the dependence of deflection angle on bias voltage. The resulting pull-in variations are listed in Table 2.

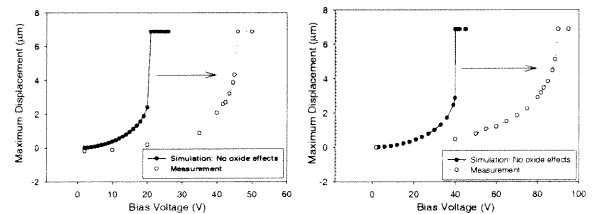
	Calc.	Sim.	Calc. (only cap. effect)	Exp (both effects)
D3: $V_{\text{pin}}$ (V)	22.7	20.9	25.2	46
D3: angle ( $^\circ$ )	0.44	0.44	0.45	0.62
C3: $V_{\text{pin}}$ (V)	40.8	39.8	44.7	88.5
C3: angle ( $^\circ$ )	0.44	0.44	0.45	0.62

Table 2. Pull-in variation due to oxide effects. Columns 2 and 3 are calculation and simulation results without considering the effects of oxide, column 4 is the calculated results considering only the added effect of oxide capacitance, and column 5 is the measured

results considering both the added effect of oxide capacitance and the net oxide charge.

Table 2 demonstrates the influence of oxide in extending the travel range beyond its 44% theoretical limit in the absence of oxide. Without oxide, the MemCad simulated pull-in voltages are 20.9V and 39.8V for D3 and C3 devices respectively, showing good agreement with analytically calculated pull-in voltages, 22.7V and 40.8V. In column three, note that the pull-in angle is only slightly increased over 44% due to the influence of oxide capacitance, at the cost of several volts of applied bias. We conclude that the travel range cannot be significantly increased by the oxide capacitance effect alone. However, with a net oxide charge present, the repulsive force is inversely related to the deflection angle and the resultant repulsive torque can increase dramatically with increased deflection angle.

The simulated results for electrodes without an oxide, and the measured results including the effects due to the presence of the oxide, are compared in Figure 5. The travel range of both D3 and C3 devices was increased from 44% to 62% at the cost of roughly doubling the applied bias voltage. A similar trade-off is seen for alternative travel range extension methods.



**Figure 5.** Effects of net oxide charge on the displacement of D3 and C3 micro-mirror devices.

## 6. Conclusions

The oxide capacitance reduces the effective bias voltage of narrow gap electrostatic micro-mirrors with only a slight increase in deflection angle while the existence of net oxide charge leads to extended travel range (from 44% to 62% for full plate micro torsion mirrors). These effects reveal a new approach for travel range extension of electrostatic micro-actuators. Because of its simplicity, reproducibility and ease of manufacture, as well as benefits of decreased stiction and inhibited electrode shorting, using insulating coating layers may be preferred over other travel range extension methods in many applications.

The authors acknowledge financial support for this work from the NJ MEMS Initiative sponsored through the NJ Commission on Science and Technology.

## 7. References

- [1] N. Jackman et al., "Optical Cross-Connects for Optical Networking," *Bell Labs Tech. J.*, pp. 262-281, Jan.-Mar. 1999.
- [2] R. Brown et al., "Micromachined, Electrostatically-Actuated Optical Modulators Fabricated by Fusion Bonding of Single-Crystal, Ultra-Thin Silicon Wafers," *Proc. of the 5th Int. Symp. on Semiconductor Wafer Bonding*, Honolulu, Hawaii, October 17-22, 1999, to be published.
- [3] O. Degani et al., "Pull-In Study of an Electrostatic Torsion Microactuator," *Journal of Microelectromechanical Systems*, Vol. 7, No. 4, pp. 373-379, 1998.
- [4] Hung et al., "Extending the Travel Range of Analog-Tuned Electrostatic Actuators," *Journal of Microelectromechanical Systems*, Vol. 8, No. 4, pp. 497-505, 1999.

# Modeling and Simulation on Two Passive Feedback Methods to Obtain Large Travel Range of Electrostatic Micro Mirrors

XingTao Wu, ZhiXiong Xiao and K. R. Farmer

New Jersey Institute of Technology, Microelectronics Research Center  
Newark, NJ, 07012, USA, [xxw3135@njit.edu](mailto:xxw3135@njit.edu)

## ABSTRACT

This paper demonstrates two passive feedback methods to obtain increased travel range in electrostatic micro actuators directly in the *electrostatic* domain. The first method is modeled as a series capacitor loop in which an integrated fixed capacitor is utilized as a voltage divider to control the effective actuation voltage across the variable capacitor/actuator, and the resulting increased travel ranges are obtained up to 100% and ~70% full scale for vertical Z micro actuators and torsion full-plate micro actuators, respectively. The second method utilizes negative feedback due to Coulombic repulsion force between the net oxide charges that exist in two oxide layers placed between the actuator electrodes, and the resulting travel range is found to be 62% for a fabricated three-spring device.

**Keywords:** Electrostatic Micro Mirror, Electrostatic Micro Actuator, Travel Range, Series Capacitor Loop, Pull In.

## 1 INTRODUCTION

Large travel range is especially important in emerging optical micro mirror and variable capacitor applications. In theory, the maximum travel range before pull in is 33.33% for full-plate vertical out-of-plane electrostatic actuators and 44.04% for torsion electrostatic actuators [1]. Generally, in order to extend an actuator's travel range before snap down, a negative feedback mechanism is required. *Mechanical* approaches such as leveraged bending and strain stiffening have been examined previously [2]. The two methods described here introduce negative feedback and extend the travel range directly in the *electrostatic* domain. These methods are passive in that no external closed loop feedback control is employed.

The first method utilizes a series capacitor to modulate the effective actuation voltage across the variable capacitor. The resulting voltage across the actuator exhibits a maximum value at a specific applied bias, beyond which it begins to drop even though the charge density keeps increasing to give an increased electrostatic torque. The effect of this decreasing voltage is to delay the increase of electrostatic torque so that the restoring elastic torque can balance it at an expanded travel range. Two typical micro

mirror structures: out-of-plane vertical and torsion, are used to verify this concept. In this paper we will first present the mathematical analysis of the series capacitor loop model, then simulation results obtained using the CoSolver feature of Memcad<sup>TM</sup> software are compared with analytical results with good agreement.

The second method utilizes negative feedback due to coulombic repulsion between the net oxide charges that exist in two oxide layers placed between the actuator electrodes. The net oxide charge is modeled to be immobile and located within 25Å of the Si-SiO<sub>2</sub> interface, without electrical communication with the Si. The C-V characteristics of the fabricated torsion mirror structure show a negative net oxide charge density of magnitude 10<sup>10-12</sup>/cm<sup>2</sup>. The repulsive interaction will occur significantly when oxides layers are in close proximity (e.g. d=6.96µm for example device). In addition, the fixed charge density is comparable to the surface charge density (10<sup>9-12</sup>/cm<sup>2</sup>) due to applied bias voltage from 1V to 200V for our prototype device. Therefore an extra repulsive electrostatic torque is superimposed on the attractive electrostatic torque to retard the increasing rate of the total electrostatic torque in such a manner that a negative feedback mechanism is introduced into the actuator structure that enables the elastic torque of spring structure to balance the electrostatic torque at an expanded travel range up to 62% of full scale deflection. This increased travel range occurs at the expense of an increased bias voltage. It should be mentioned that the oxide layers also serve as a voltage divider in the prototype structure, but this effect is not dominant.

## 2 MODELING AND ANALYSIS FOR METHOD 1

As modeled in Figure 1, the first method utilizes an integrated fixed series capacitor as a voltage divider to modulate the effective voltage across the variable capacitor /actuator. Applying Newton's second law to the 1-D actuator system gives the structural equation (1). Differentiating with respect to x, multiplying by x and subtracting equation 1 gives the pull-in equation (2).

$$\frac{1}{2} \frac{dC}{dx} V^2 = Kx \quad (1)$$

$$\frac{d^2 C}{dx_{PIN}^2} - \frac{1}{x_{PIN}} \frac{dC}{dx_{PIN}} = 0 \quad (2)$$

where  $C$  is the overall capacitance of the actuator system and  $K$  and  $x$  are the generalized spring stiffness and the change of generalized displacement, respectively.

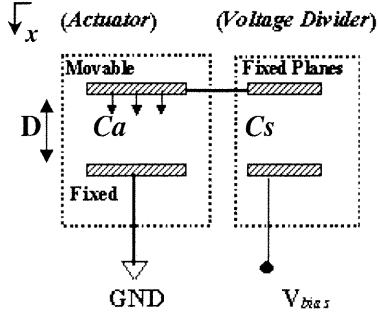


Figure 1: Circuit of Series Capacitor Loop

The static characteristics of an arbitrary electrostatic micro actuator are determined by the 1<sup>st</sup> and 2<sup>nd</sup> derivatives of the overall capacitance of the actuator system with respect to  $x$ , and the design of an actuator system is simply the design of its overall capacitance. For most applications, there are analytical expression or empirical approximation for the overall capacitance that enable designers to obtain quick characteristics for the static behavior of an electrostatic micro actuator by utilizing the above equations. Now we address the obtainable large travel range for two popular electrostatic micro mirror structures.

## 2.1 Vertical Z Actuator

In the vertical Z actuator, the movable plate is rigid and suspended by a folded spring structure. We assume that no deformation occurs on the movable electrode plate during actuation as illustrated in figure 2. Also, we consider the case of full plate actuation.

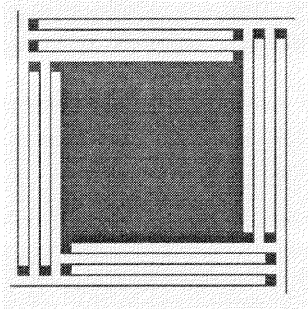


Figure 2: Vertical Z Mirror 2-D layout View

Referring to figure 1, we define the capacitance ratio  $\alpha = C_{a0}/C_s$  (where  $C_{a0}$  is  $C_a$  at  $x=0$ ), then  $C_s$  takes the form:  $C_s = \alpha^{-1} C_{a0} = \alpha^{-1} (\epsilon_0 A/D)$ . Considering this integrated capacitance, the net capacitance of the actuator system satisfies the relation  $C^{-1} = C_a^{-1} + C_s^{-1}$ . The overall capacitance  $C$  can be shown to be:

$$C = \frac{\epsilon_0 A}{(1 + \alpha)D - x} \quad (3)$$

Plugging the 1<sup>st</sup> and 2<sup>nd</sup> order derivatives of equation (3) into equation (1) and (2), the structural and pull in equations are obtained as:

$$\frac{\epsilon_0 A V^2}{2[(1 + \alpha)D - x]^2} = Kx \quad (4)$$

$$\frac{2}{[(1 + \alpha)D - x_{PIN}]} - \frac{1}{x_{PIN}} = 0 \quad (5)$$

The travel range is solved to be:

$$TR = \frac{x_{PIN}}{D} = \frac{1}{3}(1 + \alpha) \quad (6)$$

Thus the effect of the incorporated capacitance is equivalent to a gap depth extension from  $D$  to  $(1 + \alpha)D$ . The travel range of the new system becomes  $1/3$  multiplied by  $(1 + \alpha)$ , always larger than that of a single capacitor system for  $\alpha \neq 0$ . A ratio  $\alpha = 2$  leads to 100% gap depth travel range, where the series capacitance is equal to half of the zero deflection  $C_{a0}$  value.

The corresponding pull in voltage is obtained as:

$$V_{PIN} = \sqrt{\frac{8KD^3}{27\epsilon_0 A}} (1 + \alpha)^{3/2} \quad (7)$$

Equation (7) indicates that the increased travel range is obtained at sacrifice of actuation voltage by a factor of  $(1 + \alpha)^{3/2}$ . Equations (6) at  $\alpha = 0$  lead to the well-known  $1/3$  travel range for a single capacitor vertical z-actuator.

## 2.2 Cantilever Torsion Actuator

For the wedge shaped capacitance of the actuator shown schematically in figure 3 and considering the single active wedge-like capacitance:

$$C_a = \frac{\epsilon_0 W}{\theta} \ln \frac{D}{D - L\theta} \quad (8)$$

where  $W$  and  $L$  are the mirror width and length respectively,  $D$  is initial gap depth and  $\theta$  is the angle of tilt under bias voltage. In this system the introduction of a series capacitor leads to the ratio  $\alpha(\theta)$  such that  $[\alpha(\theta)^{-1} - 1] = C_a(\theta)/C_s$ . The overall capacitance  $C$  of the torsion actuator system can be easily expressed as:  $C = C_a(\theta) \cdot \alpha(\theta)$ . For this system, the structural and pull-in equations become:

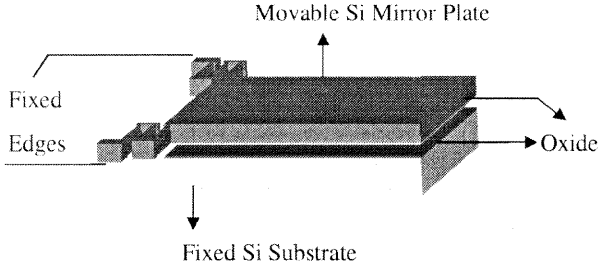


Figure 3: Torsion Micro Mirror with Oxides

$$\frac{1}{2} (C'_a \alpha + C_a \alpha') V^2 = K_\theta \theta \quad (9)$$

$$\left[ (C''_a \alpha + 2C'_a \alpha' + C_a \alpha'') - \frac{1}{\theta} (C'_a \alpha + C_a \alpha') \right]_{\theta_{PIN}} = 0 \quad (10)$$

The complexity of the capacitance expression requires numerical iteration in order to solve equations (9) and (10). Section 4 will provide a comparison between these solutions and FEA simulation results. It can be shown that for the example device NC3, the travel range increases up to 70% of the full scale.

### 3 ANALYSIS OF METHOD 2

For the torsion actuator of figure 3, the structural equation is:

$$M^{(A)}(\theta) - M^{(R)}(\theta) = K_\theta \theta \quad (11)$$

$M^{(A)}(\theta)$  and  $M^{(R)}(\theta)$  are the electrostatic attractive and repulsive torques respectively. The pull-in angle and bias voltage are determined by solving equation (6):

$$\left( \theta \cdot \frac{dM^{(A)}(\theta)}{d\theta} - M^{(A)}(\theta) \right) - \left( \theta \cdot \frac{dM^{(R)}(\theta)}{d\theta} - M^{(R)}(\theta) \right) = 0 \quad (12)$$

Numerical approximation by expansion techniques and FEA simulation can be used to find the solutions for equation (11) and (12).

## 4 SIMULATIONS AND CALCULATIONS FOR METHOD 1

### 4.1 Vertical Z Actuator

For vertical bending actuators, as shown in figure 4, the resultant voltage across the actuator exhibits a maximum value at a specific applied bias, beyond which it begins to drop. It can be seen from this calculation that the maximum effective voltage occurs exactly at the original pull in position if no series capacitor were presented. Although the charge density on the movable plate always increases with the bias voltage, the voltage across the air gap does not increase beyond the maximum value because of the rapid capacitance increase of variable capacitor.

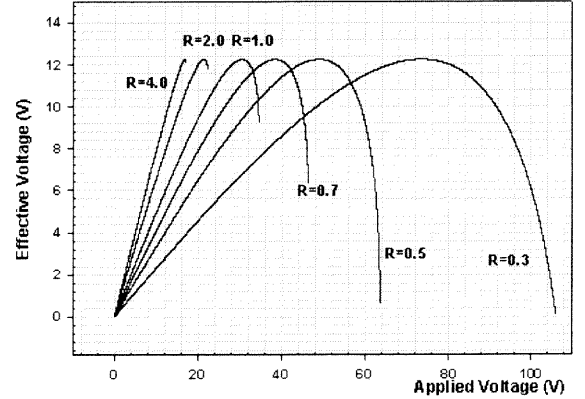


Figure 4: Effective Actuation Voltage vs. Applied Bias Voltage for Different Capacitance Ratio ( $R=C_s/C_{a0}$ ) for Vertical Z Actuator

The effect of this decreasing voltage is to delay the increase of electrostatic torque so that the restoring elastic torque can balance it at an expanded travel range. Numerical analysis shows that at the expense of increased applied voltage, the series capacitor can expand the travel range to 100% full scale for out-of-plane vertical full-plate micro actuators. The extended travel range (vertical (VC1) devices) is illustrated in Figures 5 showing the travel range extension results for different ratios of the series to initial actuator capacitance.

In figure 5,  $R$  is the reciprocal of the pre-defined capacitance ratio  $\alpha$ . The theoretical analysis results agree very well with simulated results. If  $R$  is chosen smaller than 0.5, the full-scale travel range can be achieved.

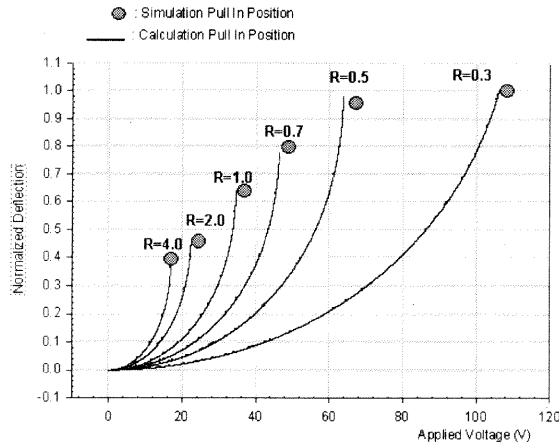


Figure 5: Normalized Deflection vs. Applied Voltage for Different Capacitance Ratios. Vertical Z Actuator VC1 with Gap Depth=4um

## 4.2 Cantilever Torsion Actuator

A torsion mirror (NC3) as illustrated in figure 3, neglecting the effects of oxides, is simulated with different capacitance ratios. Figure 6 shows the comparison of iteration and simulation results, where R is equal to  $C_s/C_a0$ . These results are found to be in good agreement.

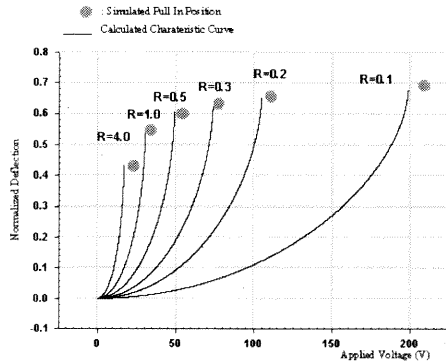


Figure 6: Normalized Deflection vs. Applied Voltage for NC3 Torsion Mirror with Gap Depth=12um.

## 5 SIMULATION VS EXPERIMENT COMPRISON FOR METHOD 2

The net oxide charge density is calculated to be  $\sim 6.2 \times 10^{10}/\text{cm}^2$  by C-V characteristics [3]. An empirical expression for repulsive electrostatic torque is curve fitted as equation (7) for a D3 device. This expression is given in equation (13). Other devices follow the same pattern with variable coefficients; this fact implies that the net oxide charge has well-defined bias voltage dependence.  $V_0$  (12V for D3) is the bias voltage at which the mirror has zero deflection angle.

$$M^{(R)}(\theta) = \frac{\epsilon_0 W (V + V_0)^2}{2} \left( \frac{L}{d} \right)^2 \left( 0.366 - 0.076\theta + 0.508\theta^2 + 2.23\theta^3 \right) \quad (13)$$

The simulated results, and the measured results without the effects of the net oxide charge present, are compared in figure (7). The travel range of D3 was increased from 44% to 62% at the cost of an increased bias voltage.

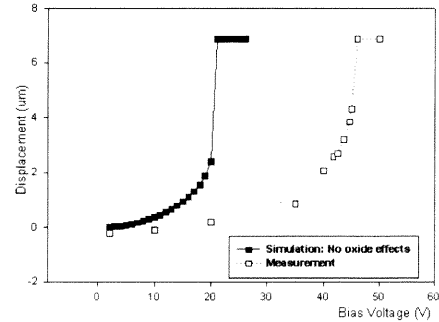


Figure 7: The Measured Effects of Oxides on The Deflection Dependence on Bias Voltage for D3 Device.

## 6 CONCLUSIONS

Two passive feedback methods have been described which give increased travel range in electrostatic actuators but sacrifice bias voltage. These methods can be combined to optimize travel range for customized applications. Because of their simplicity, reproducibility and ease of manufacture, the methods may be preferred over other travel range extension methods in some electrostatic micro actuator applications, for example, variable capacitors of wide tunable range and large deflection micro mirror structures. Future work needs to be done to investigate the voltage-dependence of net oxide charge and its effects on repulsive electrostatic torque.

This work was supported in part by the New Jersey Commission on Science and Technology through the NJ MEMS Initiative, and by the National Foundation through grand number DMR-9871272.

## REFERENCES

- [1] Ofir Degani, et al., JMEMS, Vol. 7, No. 4, pp. 373-379, 1998.
- [2] Elmer S. Hung, et al., JMEMS, Vol. 8, No. 4, pp. 497-505, 1999.
- [3] X.T Wu, et al., OMEMS'2000 Conference Proceeding, IEEE, pp. 151-152.

## A generalized capacitance-based model for electrostatic micro-actuators

Xingtao Wu<sup>1</sup>, Jiang Zhe<sup>2</sup>, Jingshan Wang<sup>1</sup>, Jin Cheng<sup>2</sup>, Vijay Modi<sup>2</sup>, and K. R. Farmer<sup>1</sup>

<sup>1</sup> Department of Physics, New Jersey Institute of Technology, Newark, NJ, 07102-1982

<sup>2</sup> Department of Mechanical Engineering, Columbia University, NY 10027

### Abstract

We develop a generalized capacitance-based model for the DC or quasi-static behavior of an arbitrary electrostatic micro-actuator system. The model leads to a two-variable, unitless equation to describe the response of one degree-of-freedom actuators to an applied bias. In this approach, the problem is reduced to one of determining an expression for the system capacitance, which significantly simplifies the modeling process over the traditional force-based method. The usefulness of the capacitance-based method is illustrated by analyzing several actuator structures, including typical devices, complex designs and the effects of fringing fields.

### Introduction

Electrostatic micro-actuators are small variable capacitor structures that exhibit mechanical motion in response to an applied voltage. During stable operation, the electrical force between plates is balanced by an elastic restoring force that is a function of the design and materials of the structure. In many important microelectromechanical systems (MEMS) applications, such as micro-mirrors or etalons, electrostatic actuation is favored over other more complex or higher power options such as thermal, magnetic or shape memory processes. The modeling of electrostatic actuator systems has attracted considerable attention in the literature for a wide variety of actuator types [1-9]. These include actuators with various electrode shapes [4] and sizes [5], and designs that employ the use of strain stiffening [6], residual stresses [7], and series capacitors [3,9]. Usually the models take a force-based approach to calculate the static device behavior by considering the balance between the elastic restoring force and the attractive electrical force. This approach typically leads to a structural equation that predicts the actuator position as a function of applied voltage, and defines the stable, low voltage region of operation prior to runaway or pull-in, where the nonlinear electrostatic force overcomes the typically linear restoring force. For classical designs, such as full-plate piston and torsion actuators with one fixed and one movable plate separated by an air gap, pull-in is found to occur when the plate displacement, as a fraction of the maximum displacement (either the original gap depth or the maximum tilt angle), is 0.33 and 0.44, respectively [1-2].

In contrast to the approach where the electrostatic force is formulated directly for each design, which can be challenging for complex systems, in this paper we develop a single, general, capacitance-based model that can be applied to the design of virtually any electrostatic actuator system. In our approach, the problem becomes one of determining an expression for the system capacitance, which can significantly simplify the modeling process. After first deriving a set of capacitance-based differential equations to describe the system, we formulate a general, unitless equation which is valid for one degree-of-freedom electrostatic micro-actuators. Using this theory, we describe a sequence of steps that can be followed in designing electrostatic micro-actuators quickly, without going through exhaustive force analysis. To demonstrate the usefulness of this approach, the process is applied to the analysis of several example actuator structures.

### Theory and Method

An electrostatic actuator can be modeled as a variable capacitor suspended by elastic springs as shown in Figure 1. The equations to describe this system are derived under the assumption that the spring stiffness components,  $K_i$  ( $i=1,2,3$ ), are constants and independent of the actuated strain.

Applying conservation of energy to the electro-mechanical system and differentiating with respect to displacement components,  $x_i$ , results in a structural equation in the force domain given by:

$$\frac{1}{2} \left[ \frac{\partial C}{\partial x_1} \quad \frac{\partial C}{\partial x_2} \quad \frac{\partial C}{\partial x_3} \right] V^2 = [x_1 \quad x_2 \quad x_3] \cdot \begin{bmatrix} K_1 & 0 & 0 \\ 0 & K_2 & 0 \\ 0 & 0 & K_3 \end{bmatrix}, \quad (1)$$

where  $C$  is the variable actuator capacitance, and  $K_i$  and  $x_i$  are orthogonal spring stiffness and displacement components, respectively. Multiplying by  $x_i$  on both sides of Eq. (1), and differentiating with respect to  $x_i$ , leads to the pull-in equation for the structure when evaluated at the pull-in displacement position:

$$\left[ \frac{\partial^2 C}{\partial [x_i]^2} - \frac{1}{x_i} \frac{\partial C}{\partial x_i} \right]_{x_i = x_{i,PIN}} = 0. \quad (2)$$

Hence the pull in voltage can be derived as:

$$V_{i,PIN} = \sqrt{\frac{2K_i}{\left( \frac{\partial^2 C}{\partial [x_i]^2} \right)_{x_i = x_{i,PIN}}}}. \quad (3)$$

The above three equations govern the static behavior of electrostatic micro-actuators. From these equations, the displacement dependence on applied bias voltage can be obtained using Eq. (1), and pull-in displacement and voltage can be obtained using Eqs. (2) and (3), respectively.

The static characteristics of an arbitrary electrostatic micro-actuator are determined by the 1<sup>st</sup> and 2<sup>nd</sup> derivatives of the overall capacitance of the actuator system with respect to displacement. Therefore, the design of an actuator system is actually a design of the derivatives of the system capacitance. From the pull-in equations, it can also be concluded that pull-in displacement has no spring stiffness dependence, and the stiffness only contributes to the pull-in voltage. These equations are also valid for actuator systems with multiple capacitors, such as the previously reported travel range extension work using series capacitors[3,9], or complex devices such as one discussed later in this paper, which are modeled using multiple capacitor components. In these cases, one needs to consider overall system capacitance instead of the single, variable capacitance.

In many applications, the actuator system is engineered to be a one degree-of-freedom (1 DOF) system. For such a system we can rewrite Eq. (1) at pull-in as:

$$\frac{1}{2} \frac{dC}{dx} \Big|_{x_{PIN}} V_{PIN}^2 = Kx_{PIN}. \quad (4)$$

When combined with the general structural equation, spring parameters are eliminated from the equation, and we are left with a two-variable, unitless equation to describe the motion of a 1 DOF actuator:

$$\Lambda \cdot U^2 = 1, \quad (5)$$

where,  $\Lambda$  is defined as  $\Lambda \left( \frac{x}{x_{PIN}} \right) = \frac{\frac{1}{x} \frac{dC}{dx}}{\left[ \frac{1}{x} \frac{dC}{dx} \right]_{x=x_{PIN}}}$ , and  $U = \frac{V}{V_{PIN}}$ .

The unitless actuation response equation, Eq. (5), is valid for 1 DOF electrostatic actuator systems. For a given design, if an analytical expression is used for the capacitance, the actuation curve can easily be obtained using the design flow shown in Fig. 2. In the figure, the device dimensions, the spring stiffness or elasticity parameters, and an expression for the device capacitance are to be set by the designer. Then the pull-in displacement is calculated using Eq. 2, the pull-in voltage is calculated using Eq. 3 and the actuation curve is determined using Eq. 5. This approach enables designers to obtain characteristics of an electrostatic micro-actuator quickly without going through exhaustive force analysis.

## Applications

### 1. Parallel piston and rectangular cantilever torsion actuators

As an example application, we consider a parallel rigid plate capacitor system where the capacitance expression is simply  $C = \frac{\epsilon_0 A}{(D - x)}$ , where  $A$  is the plate area and  $D$  is the initial gap depth. Solving the pull-in

equations leads to  $x_{PIN} = \frac{1}{3}D$  and  $V_{PIN} = \sqrt{\frac{8KD^3}{27\epsilon_0 A}}$ . By defining  $X = \frac{x}{x_{PIN}}$ , the unitless response

equation is obtained as  $2U = X \cdot \left( \frac{3}{\sqrt{X}} - \sqrt{X} \right)$ . Here the two normalized parameters, voltage and displacement, are deliberately arranged on different sides of the equation. To provide a numerical example for



this design, if the initial gap depth is 3  $\mu\text{m}$  and the pull-in voltage is calculated to be 12 V, then for 0.1  $\mu\text{m}$  displacement, a 5.5 V actuation voltage is required. Another simple but enlightening example is the rectangular full-plate torsion actuator, for which capacitance is given by  $C = \frac{\epsilon_0 A}{L\theta} \ln \frac{D}{D - L\theta}$ , where A is the area of the plate, L is the electrode length,  $\theta$  is the actuator deflection angle, and D is the initial gap depth. In this case the pull-in deflection angle is calculated to be  $\theta_{PIN} \approx 0.44 \cdot \tan^{-1}(D/L)$ , and the corresponding pull-in voltage is

$$V_{PIN} \approx \sqrt{\frac{0.83K_\theta D^3}{\epsilon_0 L^3 W}}, \text{ where } K_\theta \text{ is the torsion spring stiffness, and } W \text{ is the electrode width. The unitless}$$

response equation for this case is  $4.84U^2 = X^3 \left[ \frac{0.44X}{1 - 0.44X} + \ln(1 - 0.44X) \right]^{-1}$ , where  $X = \frac{\theta}{\theta_{PIN}}$ , which

agrees with the normalized equation obtained using a force analysis method.[8] Figure 3 shows a comparison of the two unitless actuation curves obtained for the piston and torsion spring cantilever actuator examples. These generalized results indicate that torsion and piston devices experience actuation and approach pull-in at virtually the same rate.

## 2. Torsion actuator with rigid center boss

The capacitance-based analysis method has avoided the complicated force analysis and is particularly suitable for the study of complex micro-actuator systems in which the usual force-balance approach is not straightforward. To demonstrate this, the capacitance of a double-clamped, rigid beam actuator system with a center boss is approximated, and the pull-in dependence on the length ratio of the two capacitor types is determined. As shown schematically in Figure 4, the boss is viewed as a rigid body during actuation and the rigid rotational sections are viewed as forming wedge-shaped capacitors. This is a valid assumption for a small amplitude actuation, where the rotational sections are expected to operate in a pure torsion mode. In this case, the two deflected beam sections have an angled profile, and the net capacitance for these sections is given by

$$C_1 = \frac{\epsilon_0 W L_1}{z} \ln \frac{D}{D - z}, \text{ where } z \text{ is the center deflection of the beam, } D \text{ is the initial gap depth, and } W \text{ and } L_1 \text{ are}$$

the beam width and length parameters, respectively. By adding a parallel plate capacitor  $C_2 = \frac{\epsilon_0 W L_2}{D - z}$  for the

boss region of length  $L_2$ , the overall capacitance of the actuator system is:

$$C = \frac{\epsilon_0 W L_1}{z} \ln \frac{D}{D - z} + \frac{\epsilon_0 W L_2}{D - z}. \quad (6)$$

Fringing effects are ignored in this approximation. As shown in Figure 5, the pull-in displacement is calculated to be between 0.33 and 0.44 of the initial gap depth, depending on the two length parameters  $L_1$  and  $L_2$ , ( $L = L_1 + L_2$ ).

## 3. Series capacitor method to extend travel range

Another application example is the analysis of the series capacitor method to extend the travel range of electrostatic actuators[3,9]. In this case, the overall capacitance of the system should be used, satisfying the relation  $C^{-1} = C_a^{-1} + C_s^{-1}$ , where  $C_a$  is the variable actuator capacitance and  $C_s$  is the fixed series capacitance. Taking  $\alpha$  to be the capacitance ratio at zero bias,  $C_s/C_a$ , the pull-in displacement is solved to be

$$x_{PIN} = \frac{1}{3}(1 + \alpha)D. \text{ Thus adding the series capacitance is equivalent to extending the gap depth from } D \text{ to}$$

$(1 + \alpha)D$ . The unitless actuation equation takes the same form as that of a single parallel plate capacitor system. The extended travel range effect is illustrated in Figure 6 for a full plate, piston-type actuator[9]. Notice that at the expense of increased bias voltage, travel range is extended from 33% of the initial gap depth for  $\alpha = 0$  (i.e., no series capacitor) to full travel with no pull-in for  $\alpha > 2$ . As shown in the figure, the calculated pull-in points compare favorably with values determined using MEMCAD 4.8 finite element analysis simulation.

#### 4. Cantilever torsion actuators with power function shaped electrodes

The capacitance equations provide a shortcut method for investigating actuators with various electrode shapes and sizes. As an example, we consider torsion actuators with a general power function shaped bottom electrode as sketched in Figure 7. In the figure, the rectangular, upper plate proof mass is suspended by pure torsion springs, and the bottom electrode is defined by a shape function  $y(x)$ . The initial gap between the two plates is  $D$ ,  $\theta$  is the deflection angle, and  $L$  is the plate length. Neglecting fringing field effects, the general capacitance expression is written as:

$$C = \int_0^L \left( \frac{2\epsilon_0 x^n}{D - (L - x)\theta} \right) dx \quad (7)$$

Pull-in results are calculated for capacitor expressions with various values of  $n$ . The corresponding electrode shapes are illustrated in the inset in Figure 8.

When  $n = 1$ , the geometry of the electrode is a triangle. The capacitance is:

$$C = \frac{\epsilon_0 (-D + L\theta) \text{Log}[D] + (D - L\theta) \text{Log}[D - L\theta]}{\theta^2} \quad (8)$$

The normalized pull-in angle, *i.e.*, as a fraction of the maximum tilt angle, is found to be 0.542.

When  $n = 2$  and  $n = 0.5$ , the geometry is a parabola. The capacitance is integrated as:

$$C = \frac{\epsilon_0 (L\theta(-2D + 3L\theta) + 2(D - L\theta)^2 \text{Log}[D] - 2(D - L\theta)^2 \text{Log}[D - L\theta])}{\theta^3} \quad (n = 2) \quad (9)$$

and

$$C = \frac{4p\epsilon(\sqrt{L\theta(D - L\theta)} + (-D + L\theta) \text{ArcTan}\left[\sqrt{\frac{L\theta}{D - L\theta}}\right])}{\theta^{3/2} \sqrt{D - L\theta}} \quad (n = 0.5) \quad (10)$$

The normalized pull-in angle is found to be 0.492 for  $n = 0.5$  and 0.638 for  $n = 2$ , in both cases constants, independent of the electrode length.

Generally, when  $n \in [0, \infty]$ , the capacitance is integrated as

$$C = \frac{2pL^{1+n} \epsilon F_{21}[1 + n, 1, 2 + n, \frac{L\theta}{-D + L\theta}]}{(1 + n)(D - L\theta)}, \quad (11)$$

where

$$F_{21}(a, b, c, z) = \sum_{k=0}^{\infty} \frac{(a)_k (b)_k z^k}{(c)_k k!}, \quad (12)$$

and the function  $(a)_k$  is defined as the product of  $(a)(a+1)\dots(a+k)$ . Using this general expression, the effect of the power  $n$  on the normalized pull-in angle is shown in Figure 8. As  $n$  increases, the normalized pull-in angle increases linearly to full travel range with no pull-in when  $n$  is higher than 6. The increasing travel range with  $n$  is a surprising finding for buried electrodes that are as long as the upper, movable plate.

#### 5. Fringing field effects on the static behavior of microactuators

Using the capacitance-based approach it become easy to investigate the effect of fringing fields on system pull-in. This is illustrated using two piston actuator examples: 1) very long plates of width much smaller than length,  $W \ll L$ , and 2) circular disks of radius  $R$ . Assuming that the separation between electrodes is small and that fringing effects are negligible, the capacitance for these systems is given by  $C_{plate}/L = \epsilon/b$  and  $C_{disk} = \epsilon\pi R/b$ . Here  $b$  is the aspect ratio defined as  $b = D/W$  and  $b = D/R$  for the plate and disk capacitor systems, respectively. Including fringing and actuator motion, these expressions become[10]:

$$\frac{C_{plate}}{L} = \frac{\epsilon_0 W}{D - x} \left[ 1 + \frac{2(D - x)}{\pi W} + \frac{2(D - x)}{\pi W} \log\left(\frac{\pi W}{D - x}\right) \right] \quad (13)$$

and

$$C_{\text{disk}} = \frac{\epsilon_0 \pi R^2}{D-x} \left[ 1 + \frac{D-x}{\pi R} \ln \left( \frac{16\pi R}{D-x} - 1 \right) \right], \quad (14)$$

where  $D$  is the initial gap between the two plates and  $x$  is the deflection. Using these expressions, Figure 9 shows the calculated effects of fringing on the pull-in displacement for the two types of parallel plate actuators. In typical MEMS devices, the aspect ratio  $b$  is between 0.01 and 1. Figure 9 shows that as  $b$  increases from 0.01 to 1, the effect of fringing fields is to increase system travel range from 33.33% to 36.88%, and from 33.33% to 35.4% for long parallel-plate and disk actuators, respectively. While this may be a surprising result, a similar theoretical finding has recently been published for a specific design [11].

## 6. The effect of spring stiffening on system pull-in

The capacitance-based approach can be applied to study the effect of spring stiffening on system pull-in. In this case, neglecting time-dependent forces, the 1 DOF problem becomes:

$$\frac{1}{2} \frac{dC}{dx} V^2 = K_1 x + K_3 x^3, \quad (15)$$

where the right side of the equation includes a non-linear elastic force term due to spring stiffening. In this model, the pull-in expression in Eq. 2 becomes

$$\left[ \frac{d^2 C}{dx^2} - \left( \frac{1}{1-f} \right) \frac{1}{x} \frac{dC}{dx} \right]_{x=x_{PIN}} = 0, \quad (16)$$

where  $f$  is defined as  $f\left(\frac{K_3}{K_1}, x\right) = \frac{2(K_3/K_1)x^2}{1 + 3(K_3/K_1)x^2}$ . Figure 10 illustrates the effect of spring stiffening on

system pull-in for a rectangular cantilever torsion actuator. For low values of  $K_3/K_1$ , where the nonlinear spring stiffening is negligible, the normalized pull-in angle is 0.44, as expected. A significant increase in travel range is obtained when the ratio of the cubic term over the linear term  $K_3/K_1$  goes beyond 20. At a practical range of 50 to 80, the normalized pull-in angle is about 0.5 to 0.54, but it asymptotically approaches ~0.83 for higher values of  $K_3/K_1$ .

## Conclusions

In conclusion, we have developed a general, capacitance-based model that can be applied to the design of a wide range of electrostatic micro-actuators. In this approach, the problem is reduced to one of determining an expression for the system capacitance, which can significantly simplify the modeling process over the traditional force-based method. To demonstrate the usefulness of this approach, the process has been applied to the analysis of parallel plate piston actuators, rectangular cantilever torsion actuators, a beam actuator with a rigid center boss, travel range extension using series capacitors, power function shaped cantilever torsion actuators, devices with significant fringing fields, and the effects of non-linear spring stiffening. Expected results are confirmed for the classical devices such as piston and torsion actuators. Also, a clear understanding is provided for the pull-in behavior of the complex beam actuator, the travel range extension using series capacitors and the effects of spring stiffening. Finally, two new findings are reported: increased travel range due to fringing effects and the possibility of full travel without pull-in using power function shaped, full plate electrodes.

## Acknowledgement

This work was supported in part by the New Jersey Commission on Science and Technology through the NJ MEMS Initiative, and by the National Foundation through grant numbers DMR-9871272 and ECS-9624798.

## REFERENCES

1. R. Puers and D. Lapadatu, "Electrostatic forces and their effects on capacitive mechanical sensors," *Sensors and Actuators A*, vol. 56, pp. 203-210, 1996.
2. Ofir Degani, Eran Socher, Ariel Lipson, Tomer Leitner, Dan J. Setter, Shmuel Kaldor and Yael Nemirovsky, "Pull-in study of an electrostatic torsion microactuator," *J. Microelectromech. Syst.*, vol. 7, pp. 373-379, 1998.
3. E. K. Chan and R. W. Dutton, "Electrostatic micromechanical actuator with extended range of travel," *J. Microelectromech. Syst.*, vol. 9, pp. 321-328, 2000.

4. R. Legtenberg, J. Gilbert and S. D. Senturia, "Electrostatic curved electrode actuators," *J. Microelectromech. Syst.*, vol. 6, pp. 257-265, 1997.
5. Olivier Francais and Isabelle Dufour, "Enhancement of elementary displaced volume with electrostatically actuated diaphragms: application to electrostatic micropumps," *J. Micromech. Microeng.*, vol. 10, pp. 282-287, 2000.
6. E. S. Hung and S. D. Senturia, "Extending the Travel Range of Analog-Tuned Electrostatic Actuators," *J. Microelectromech. Syst.*, vol. 8, pp. 497-505, 1999.
7. P. M. Osterberg and S. D. Senturia, "M-TEST: A test chip for MEMS material property measurement using electrostatically actuated test structures," *J. Microelectromech. Syst.*, vol. 6, pp. 107-118, 1997.
8. Z. X. Xiao, X. T. Wu, W. Y. Peng and K. R. Farmer, "An Angle Based Design Approach for Rectangular Electrostatic Torsion Actuators," *J. Microelectromech. Syst.*, accepted to be published, December 2001.
9. X.T. Wu, Z. Xiao, J. Zhe and K. R. Farmer, "Modeling and Simulation of Two Passive Feedback Methods to Obtain Large Travel Range of Electrostatic Micro Mirrors," *Proc. 4<sup>th</sup> Int. Conf. Modeling and Simulation of Microsystems*, Hilton Head, SC, March 19-21, 2001, pp. 382-385.
10. G. Kirchhoff, Zur theorie des kondensators, Monatsb. Akad. Wiss. Berlin, pp. 144-162.
11. G. Li, N.R. Aluru, "Linear, nonlinear and mixed-regime analysis of electrostatic MEMS," *Sensors and Actuators A*, vol. 91, pp. 278-291, 2001.

## FIGURE CAPTIONS

FIG. 1. A model of a 3D electrostatic actuator system in which a movable plate has three orthogonal displacement components,  $x_i$ , and three orthogonal elastic components,  $K_i$ . The actuator is driven by an applied bias,  $V_B$ .

FIG. 2. Design flow for an arbitrary 1 DOF actuator system.

FIG. 3. Comparison of two unitless actuation curves obtained for piston and torsion spring cantilever actuator examples.

FIG. 4. Schematic of a beam actuator with a rigid center boss. The boss is viewed as a rigid body during actuation, and the deformed sections are taken to have an angled profile for small gap depths and displacements.

FIG. 5. Pull-in dependence on the ratio of the deformed region length to boss length for the center boss actuator example of Figure 4.

FIG. 6. Normalized deflection versus applied voltage for different capacitance ratios for a full-plate piston-type actuator. The open circles mark the calculated pull-in points.

FIG. 7. A schematic view of a cantilever torsion actuator with an arbitrary power function shaped electrode.

FIG. 8. The effect of the power function index  $n$  on the normalized pull-in angle. The inset illustrates the electrode shapes corresponding to various values of  $n$ .

FIG. 9. The effect of fringing fields on the normalized pull-in displacement of parallel plate actuator systems of various aspect ratio,  $b$ .

FIG. 10. The effect of spring stiffening on the normalized pull-in angle of a torsion cantilever actuator.

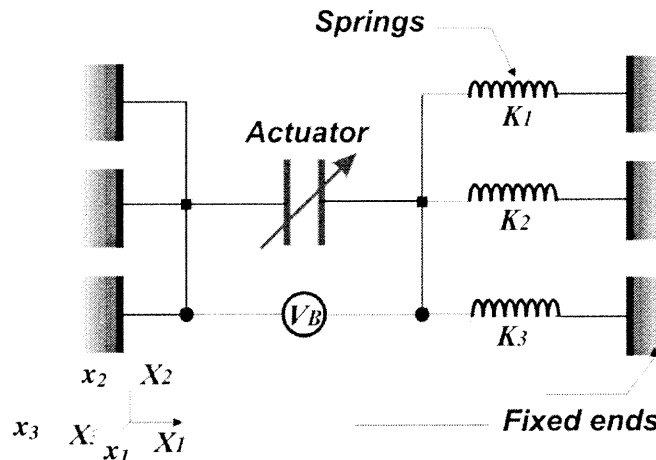


Figure 1

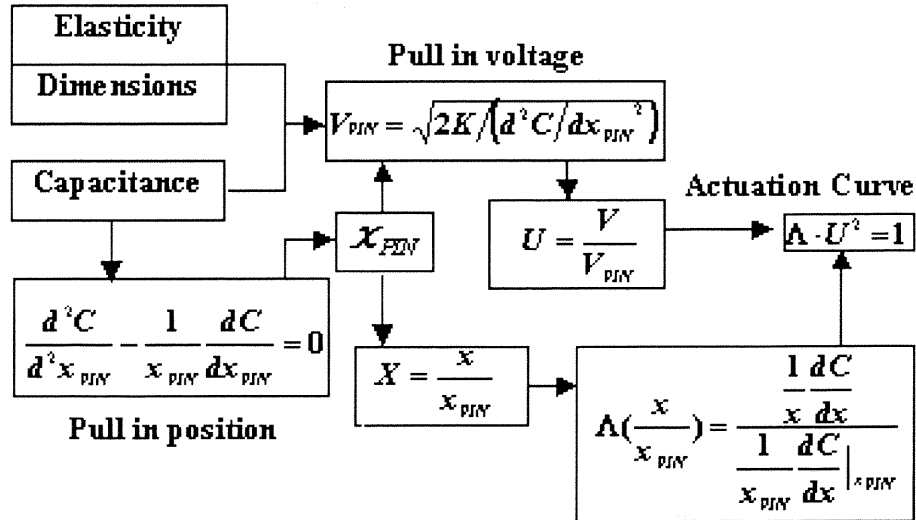


Figure 2

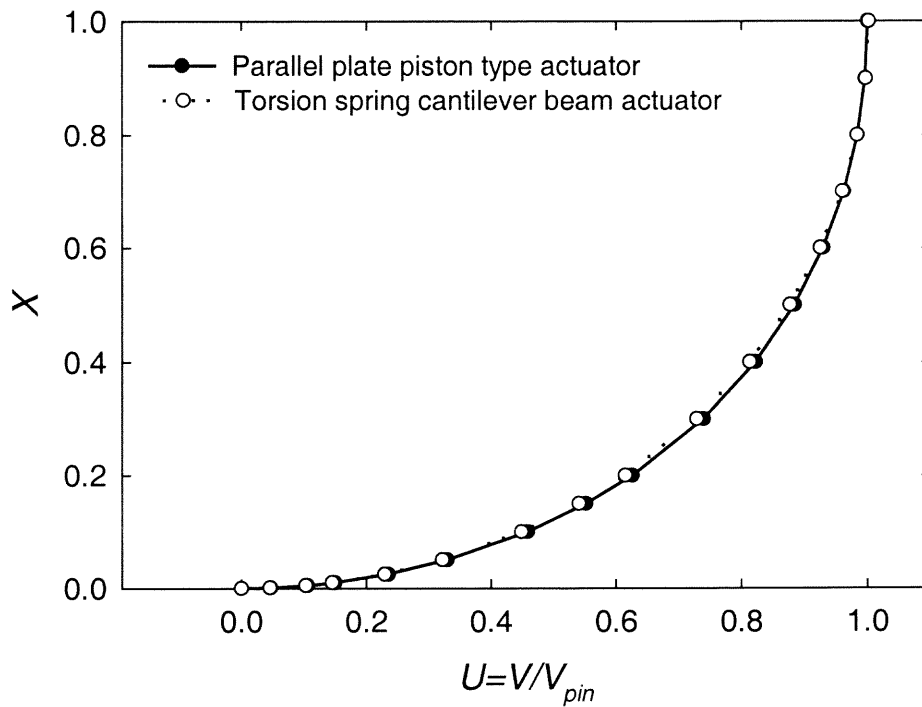
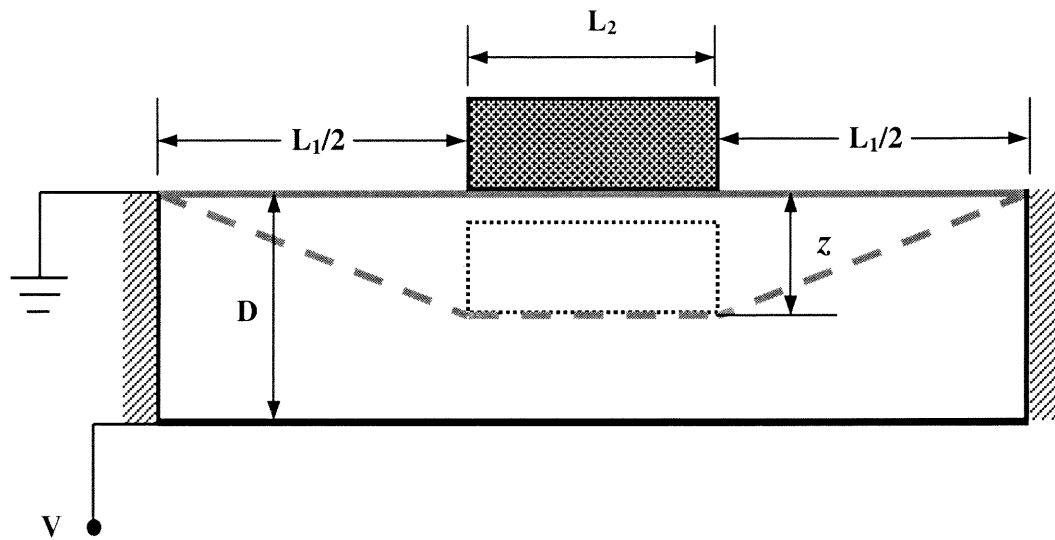
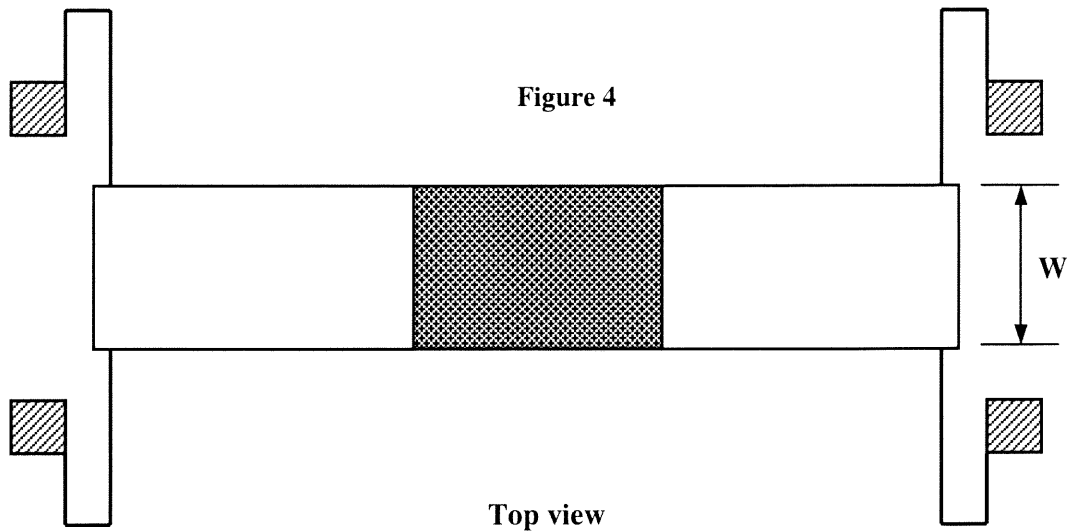


Figure 3



Side view of the beam actuator



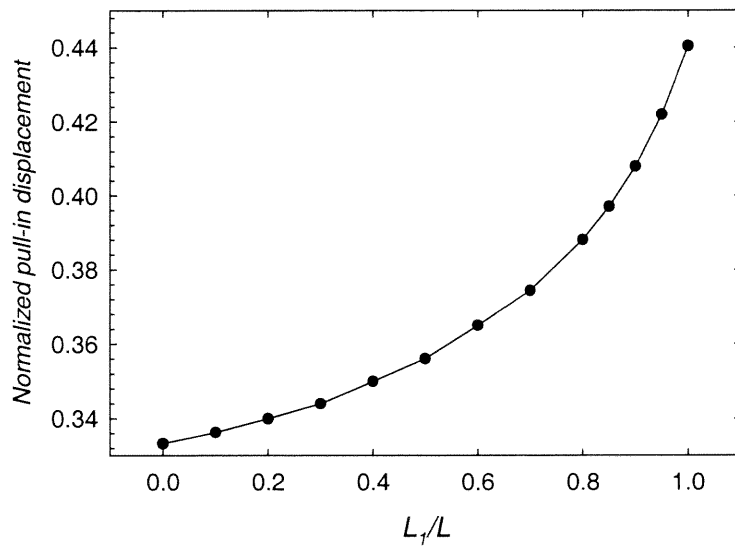


Figure 5

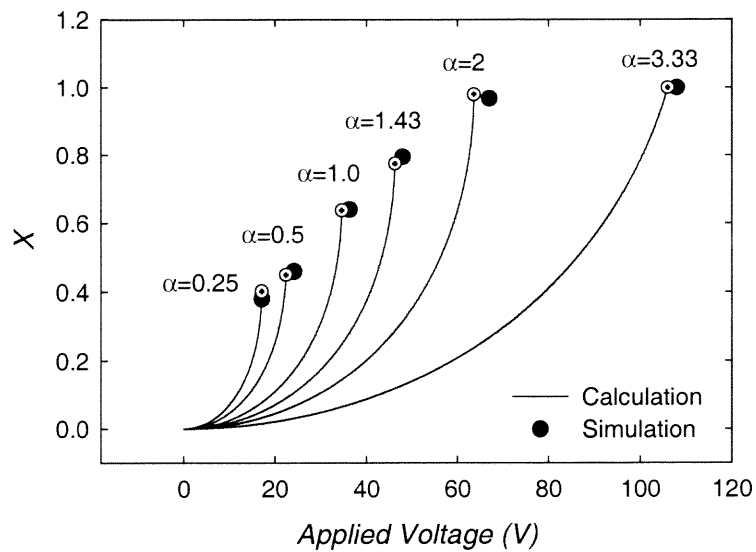


Figure 6

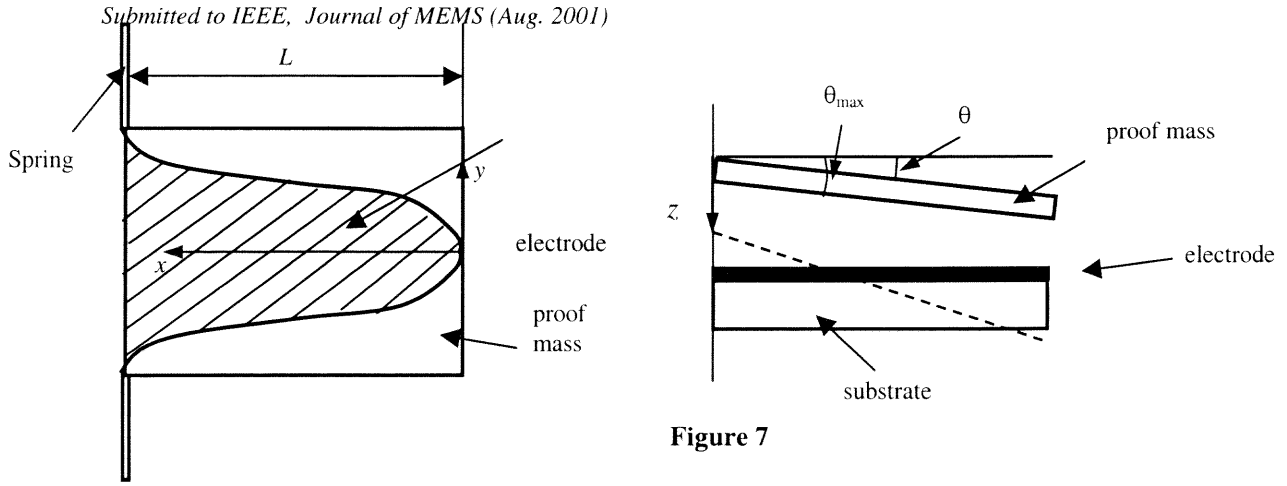


Figure 7

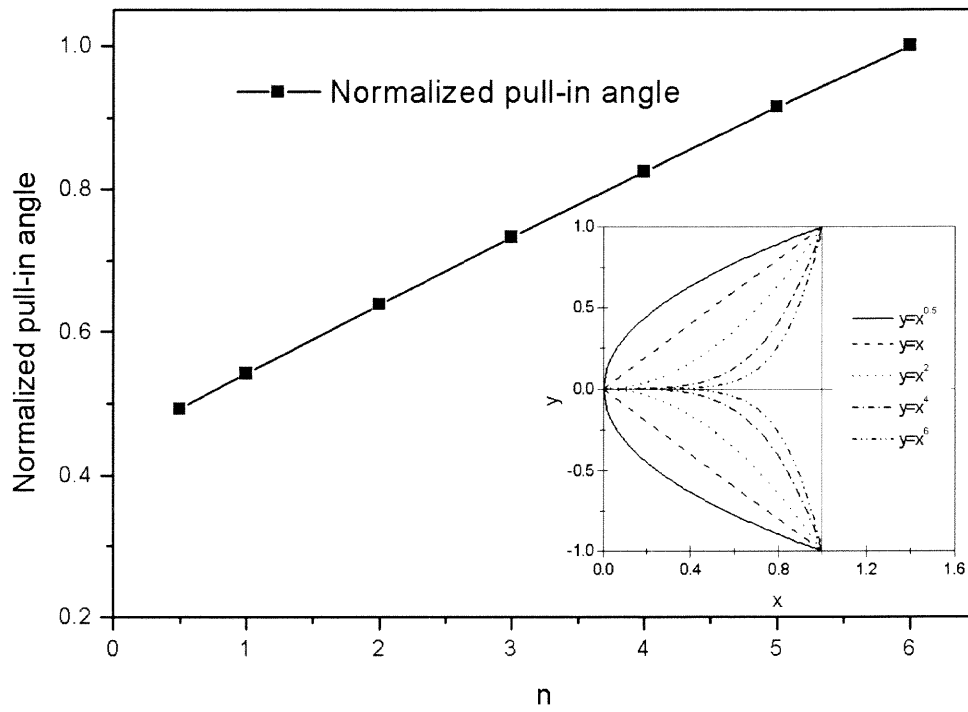


Figure 8



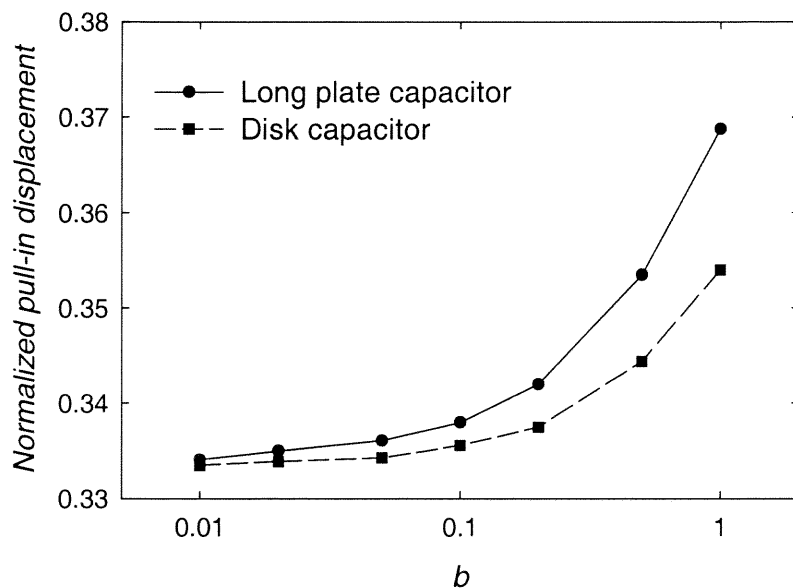


Figure. 9

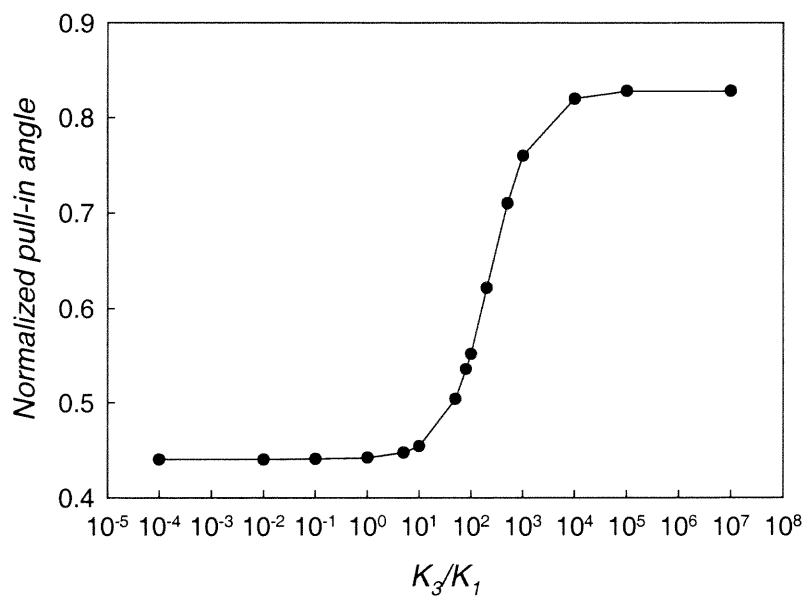


Figure 10

## Rapid MEMS Prototyping using SU-8, Wafer Bonding and Deep Reactive Ion Etching

S. K. Sampath<sup>1</sup>, L. St.Clair<sup>2</sup>, Xingtao Wu<sup>1</sup>, D. V. Ivanov<sup>1</sup>, Q. Wang<sup>3</sup>, C. Ghosh<sup>3</sup> and K. R. Farmer<sup>1</sup>

<sup>1</sup>Microelectronics Research Center, New Jersey Institute of Technology, Newark, NJ 07102

<sup>2</sup>EVI, Phoenix, AZ 85034

<sup>3</sup>Princeton Optronics, Inc., Princeton, NJ 08543

**Abstract--** We describe a technique to rapidly prototype microelectromechanical systems by combining the use of 1) patterned SU-8 photoresist to form an electrically insulating spacer layer on a silicon substrate, 2) wafer bonding to affix single crystal silicon above the spacer layer, and 3) deep reactive ion etching to form suspended structures over the patterned spacer. Technical details of the wafer bonding process are presented. Experimental results from a rapidly prototyped test structure are shown. It is expected that this process will not be limited to silicon-based systems.

micromachined glass or ceramics.[2,3] Also, patterned spacer layers ranging from ~1 to ~1000  $\mu\text{m}$  are possible using the resist, it is easily exposed using a standard UV aligner, the finished bottom surface leaves no polymer residue,[4] and cross-linked SU-8 is chemically resistant when cured above 100  $^{\circ}\text{C}$ , thermally stable to temperatures over 200  $^{\circ}\text{C}$  and compatible with the Bosch inductively coupled plasma DRIE technology. We find that our rapid prototyping approach is so successful, both in its simplicity and versatility, that it may even be sufficient for device production in some situations where thermal coefficient of expansion (TCE) mismatch between the spacer and electrodes may not be an issue.

### 1. INTRODUCTION

In the rapidly evolving microelectromechanical systems (MEMS) industry, the need exists to quickly and easily prototype devices in order to test or demonstrate their feasibility or functionality. A particular requirement common to many proposed MEMS applications is for a uniform, patterned, insulating, fairly robust spacer layer to separate, for example, fixed electrode planes from movable electrodes. The spacer must be bondable between the electrode planes, of controllable and uniform thickness, and able to withstand the thermal, mechanical and chemical stresses of device processing. In this paper we explore the possibility of using patterned thick photoresist, namely SU-8,[1] as the spacer layer for rapid prototyping, combining it with wafer bonding and deep reactive ion etching (DRIE) to quickly and easily produce "proof-of-principle" devices. Likely advantages of using SU-8 include the relatively low cost of the material, and flexibility and ease of use over other options such as

### 2. PROTOTYPING PROCESS DETAILS

To demonstrate the viability of the SU-8 approach we designed electrostatically actuated, mm-sized, ~50  $\mu\text{m}$  thick, piston-type actuator, spring suspended plates to sit ~23  $\mu\text{m}$  above a silicon ground plane. Design and simulation was accomplished using MEMCAD 4.8, to give a range of devices capable of up to several  $\mu\text{m}$ 's of vertical motion for ten's of volts applied bias. A schematic cross-section view of the device is shown in Figure 1. Our goal was to prototype a working demonstration structure as quickly and easily as possible by bonding an ultra-thin silicon membrane wafer[5] to a patterned SU-8 layer on a silicon handle wafer, then combining standard photolithography and DRIE to pattern and cut out the plate shape and springs. By using an ultra-thin silicon membrane, no post-bonding thinning or polishing step is required. A description of the fabrication sequence is

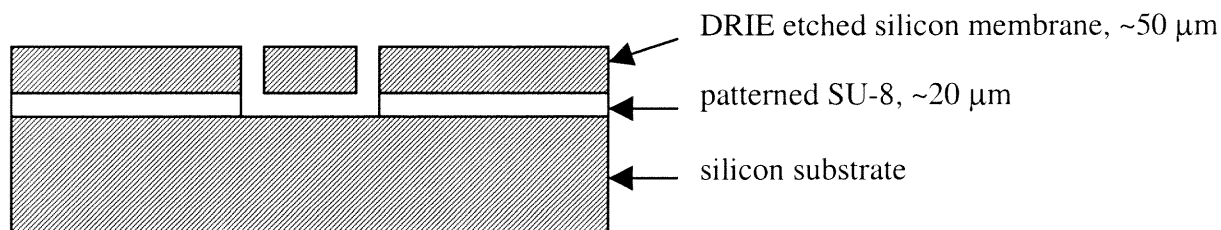


**Figure 1:** Cross-sectional illustration of a rapidly prototyped, electrostatically actuated, mm-sized, 50  $\mu\text{m}$  thick, spring suspended plate bonded via a ~23  $\mu\text{m}$  patterned SU-8 resist layer above a silicon ground plane.

**Table 1:** Rapid prototyping process details.

1. P-clean substrate and ultra-thin wafers
2. Oxidize substrate and ultra-thin wafers, ~250 nm, pyrogenic steam, 1050 °C
3. Spin SU-8 onto substrate, ~23 µm; expose and develop to form cavities
4. Bond ultra-thin wafer to patterned SU-8 <ul style="list-style-type: none"> <li>• Attach ultra-thin wafer to a handle wafer</li> <li>• Bond in EV-501 system: <math>1 \times 10^{-3}</math> mbar, 1500 N force, 100 °C, 10 min</li> </ul>
5. Photolithography on ultra-thin wafer surface for DRIE etching, Shipley 3813 photoresist
6. Dry etch oxide from exposed areas of ultra-thin wafer surface
7. DRIE ultra-thin wafer, Bosch process; stops on oxide at bond surface of ultra-thin wafer
8. Dry etch oxide from back surface of substrate wafer to enable electrical contact to substrate as a ground plane
9. Dry etch oxide from DRIE cavities to release suspended device structures
10. Metallize top surface by evaporation (Cr/Au); does not short active layer to substrate
11. Protect active devices with photoresist, dice wafer, clean individual chips and test.

provided in Table 1.

### 3. PATTERNING SU-8

SU-8 is a negative photoresist that can be spin coated and patterned using a UV contact aligner. Since it is an epoxy-based product, it is prone to thermal stresses that can lead to the formation of cracks during processing. Also, the resist needs to be handled carefully to avoid the creation of air bubbles that may impact coating results. In this demonstration project, our goal was to form a 23 µm spacer layer using the SU-8. Building on known pre- and post-exposure bake and developing processes provided by the SU-8 vendor, we developed the procedure to pattern the resist outlined in Table 2. Slow thermal ramps were important to minimize cracking of the resist near sharp features. No obvious residue remained in developed areas after processing. As shown in step 1 of Table 2, varying the spin rate allowed for control of the final spacer layer thickness from 21 to 32 µm for rates ranging from 2000 to 3500 rpm. A fairly wide range of spin rates, 2000 to 3000 rpm, gave rise to a relatively

**Table 2:** SU-8 patterning process.

1. Spin coat (specially programmed ramps to and from final spin speed): <ul style="list-style-type: none"> <li>• 2000 rpm for a 32 µm spacer layer thickness</li> <li>• 2500 rpm for a 25 µm spacer layer thickness</li> <li>• 3000 rpm for a 23 µm spacer layer thickness</li> <li>• 3500 rpm for a 21 µm spacer layer thickness</li> </ul>
2. Soft pre-exposure bake at 60 °C for 3 min, 2 min ramp to 95 °C, 5 min bake at 95 °C, >5 min ramp to room temperature
3. Expose, ~260 mJ/cm <sup>2</sup> (30 sec at ~8.5 mW/cm <sup>2</sup> )
4. >5 min ramp to 95 °C, 5 min post-exposure bake at 95 °C, >5 min ramp to room temperature
5. 1 <sup>st</sup> develop for 1 min in fresh PGMEA poured onto wafer surface, spin off developer, 2 <sup>nd</sup> develop for 4 min in fresh PGMEA poured onto wafer surface, spin dry

small thickness variation, 21 to 25 µm, near our target thickness.

## 4. BONDING TO SU-8

One key question was whether the ultra-thin wafer could be bonded to the patterned SU-8. Using EVI's universal bond tool (EV-501), and bonding in vacuum to seal the cavities formed in the resist, we have developed a successful bonding process. The process details are shown in step 4 of Table 1. The choice of 1500 N for 10 min was determined from the results of test bonds at forces ranging from 100 N to 2200 N, and compression times ranging from 5 min to 1 hr. We concluded that shorter times at higher forces gave the best results, with 5-10 min compression times over 1500 N yielding indistinguishable good results. The bonding temperature was determined from tests which showed that baking in the range of 150-200 °C produced a very hard resist layer that did not bond well. Our successful bonding is illustrated in Figure 2 which presents an IR image of a 75 mm diameter, 50 µm thick silicon wafer bonded to a ~20 µm thick patterned SU-8 layer on a standard thickness, 100 mm diameter silicon substrate. We find that the ultra-thin wafer bonds completely up to the cavity edges with no discernable delamination, and the bond is sufficiently strong that it withstands the subsequent processing steps, including SiO<sub>2</sub> dry etching, immersion in photoresist and SiO<sub>2</sub> stripping solutions (acetone and buffered oxide etch), and standard dicing using a diamond saw.

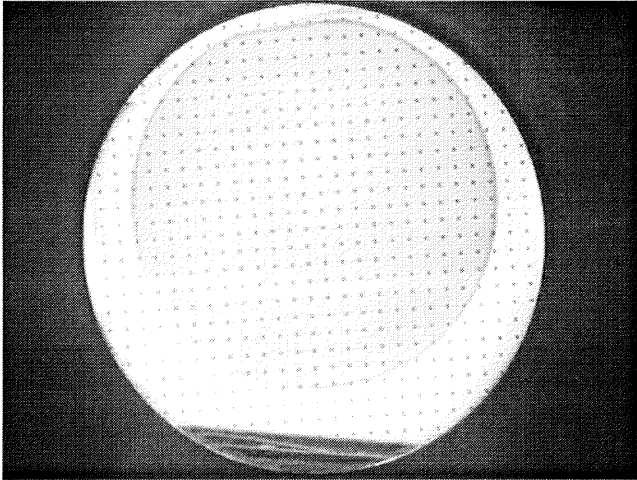


**Figure 2:** IR image of a 75 mm diameter, ~50  $\mu\text{m}$  thick silicon wafer bonded to a ~23  $\mu\text{m}$  thick patterned SU-8 layer on a standard thickness, 100 mm diameter silicon substrate.

### 5. DEMONSTRATION DEVICE

Figures 3 and 4 show VEECO optical profilometer images and analysis data for a completed, functioning chip. As described in Section 2, the active suspended plate is designed to be a vertical motion only, piston-type actuator

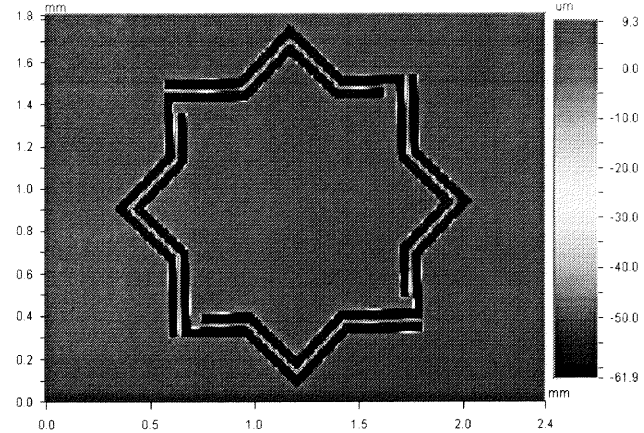


**Figure 3:** VEECO optical profilometer image of a completed, functioning chip. The plate shape is a square on top of a 45° rotated square. The square side length is 1 mm. The spring width is 10  $\mu\text{m}$ .

with approximately 1  $\mu\text{m}$  of motion for ~100 V applied across a 23  $\mu\text{m}$  thick spacer layer. As shown in Figure 3, the plate is suspended at four points by thin springs that follow the shape of the plate perimeter. The uniform coloring of the plate, springs and fixed chip surface indicates that the plate is flat and does not sag, tilt or otherwise diverge from the plane of the fixed chip surface. The X and Y profiles in Figure 4

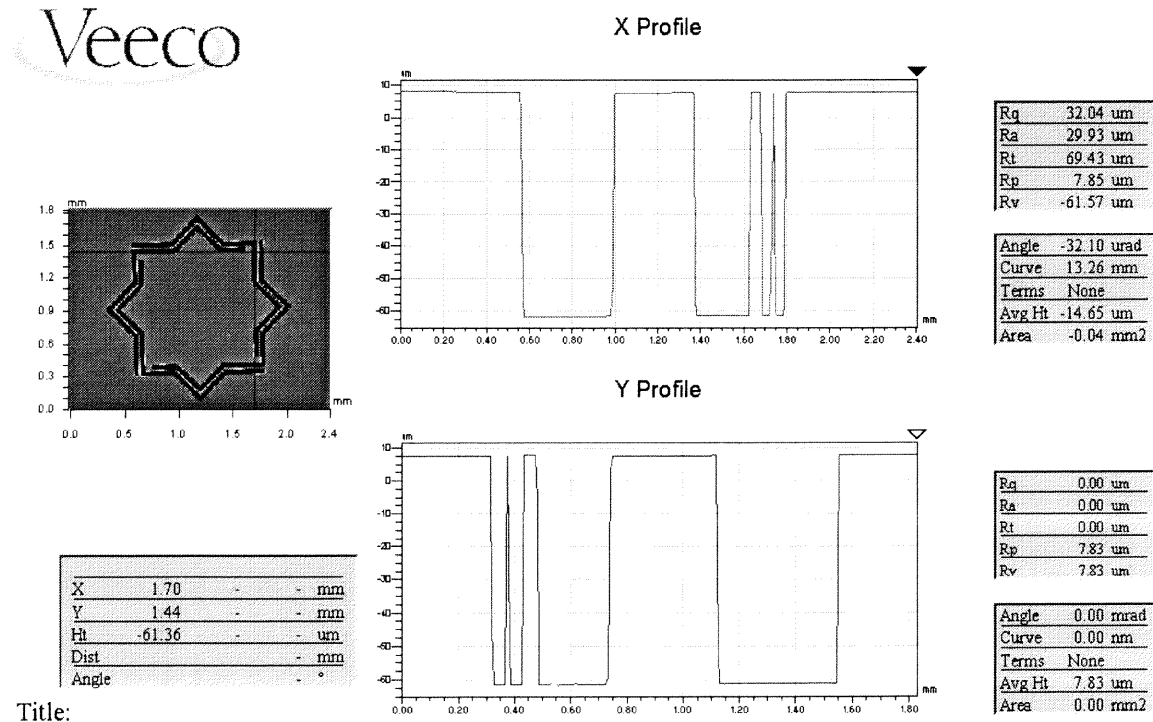


**Figure 4:** Two-dimensional analysis of the chip shown in Figure 3. The X and Y profile curves show transitions between the top of the released plate structure and the bottom of the cavity, i.e., the silicon substrate.

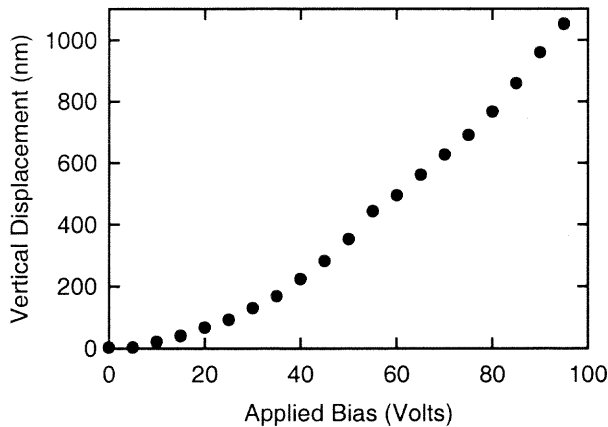


**Figure 5:** Measured vertical displacement of the movable plate as a function of applied bias.

measure the height of the transitions between the top surface of the suspended plate and the bottom of the cavity, which is found to be  $69\text{ }\mu\text{m}$ , consistent with a plate thickness of  $46\text{ }\mu\text{m}$ .

The successful demonstration of the device structure is illustrated in Figure 5. The figure plots the measured vertical membrane displacement versus the voltage between the silicon electrodes. For this particular device  $\sim 95\text{ V}$  gives  $\sim 1\text{ }\mu\text{m}$  of motion. It is important to note that the electrical isolation of the SU-8 spacer layer is sufficient to sustain at least  $100\text{ V}$ .

## 5. CONCLUSION

We have shown that patterned SU-8 photoresist can be used successfully as an electrically isolating, controlled thickness, uniform spacer layer as part of a method to rapidly prototype MEMS devices and systems. The method combines the use of SU-8, wafer bonding and deep reactive ion etching. Keys to the success of this approach have included the ability to bond silicon wafers to the patterned SU-8 layer, and the subsequent ability to process the bonded stack, including performing DRIE, standard RIE, wet

chemical processing and wafer dicing. In this paper we have provided process details for the rapid prototyping of an electrostatically actuated, mm-sized,  $\sim 50\text{ }\mu\text{m}$  thick, piston-type actuator, spring suspended plate, including the specific recipe for bonding a thin silicon membrane to an SU-8 layer patterned on a silicon substrate wafer. Devices fabricated using this method perform as expected. We believe that this rapid prototyping approach is so successful, both in its simplicity and versatility, that it may be sufficient for device production in some situations where TCE mismatch between the spacer and electrodes may not be an issue. In addition, we suspect that this approach may not be limited to silicon-based systems.

## 6. ACKNOWLEDGEMENTS

This work was supported through the National Science Foundation, awards ECS-9624798 and DMR-9871272, and the New Jersey Commission on Science and Technology through the NJ MEMS Initiative. Additional support for this work was provided through a collaboration with Princeton Optronics, Inc., Princeton, NJ.

## REFERENCES

- [1] SU-8 is a product of MicroChem Corporation, Newton, MA.
- [2] H. Lorentz, M. Despont, N. Fahrni, N. C. LaBianca, P. Renaud and P. Vettiger, *J. Micromech. Microeng.* **7**, 121-124, 1997.
- [3] H. Lorentz, M. Despont, N. Fahrni, J. Brugger, P. Vettiger and P. Renaud, *Sensors and Actuators A* **64**, 33-39, 1998.
- [4] X. Cai, A. Glidle and J. M. Cooper, *Electroanalysis* **12** (9), 2000.
- [5] "Ultra-thin" silicon wafers have been obtained from Virginia Semiconductor, Inc., Fredericksburg, VA.

## An Angle Based Design Approach for Rectangular Electrostatic Torsion Actuators

Zhixiong Xiao<sup>\*</sup>, XingTao Wu, Wuyong Peng, and K. R. Farmer  
New Jersey Institute of Technology, Microelectronics Research Center,  
121 Summit Street- Rm 200, Newark, NJ 07102, USA  
<sup>\*</sup>email address:xiao@adm.njit.edu, tel:973-596-3360, fax:973-596-6495

*Abstract*—In this paper, we develop a fast, angle based design approach for rectangular electrostatic torsion actuators based on several simple equations. This approach is significantly more straightforward than the usual full calculation or simulation methods. The main results of the simplified approach are verified by comparing them with analytical calculations and MEMCAD simulations with fractional difference smaller than 3% for torsion mode dominant actuators. Also, good agreement is found by comparison with the measured behavior of a micro-fabricated full-plate device.

*Index Terms* — Angle based design approach, rectangular electrostatic torsion actuators.

### I. INTRODUCTION

In response to the demand for increased information capacity, microelectromechanical systems (MEMS), including optical cross-connects, optical switches, and electrically controlled variable attenuators, are being investigated for the emerging all optical telecommunications network [1]. Electrostatic torsion actuators have been implemented in many of these optical MEMS systems. An important property of the actuators is their pull-in voltage, beyond which the electrostatic torque overcomes the mechanical torque, and the movable plate snaps abruptly to the fixed electrode plane. The aim of a typical design is to determine spring and electrode parameters for a chosen working point near pull-in that corresponds to a desired maximum controllable tilt angle at a given applied bias voltage. Numerous papers address torsion actuators and the related pull-in voltage [2-10]. Among them, Hornbeck [7] uses an analysis based on the balance between the supporting beam torsion spring torque and the distributed 2-D electrostatic torque on the plate, but this approach does not lead to a straightforward expression for the pull-in voltage and the fractional deflection at the pull-in. Osterberg [8] and Gupta [9] have used electrostatically actuated microelectromechanical test structures for measurement of device and material properties, including pull-in. With this approach, Osterberg derives a 1-D lumped model equation for the spring constant of a rectangular torsion beam, and uses this expression in a pull-in voltage equation. However, the fractional deflection is not derived. Degani, et al., [10] have proposed polynomial algebraic equations for the pull-in voltage and angle in torsion actuators. However, this calculation is relatively complicated and time consuming, and must be repeated for every design variation. In this paper, an angle based design approach for rectangular, electrostatic torsion actuators is proposed based on several straightforward equations. This approach makes the design optimization process much easier and faster than the usual full analytical calculation or finite element simulation methods. The results of the simplified approach are verified by comparing them with analytical calculations and MEMCAD simulations with fractional difference smaller than 3% for torsion mode dominant actuators. Also, the predicted

results are compared with the measured behavior of a full-plate device, and found to be in good agreement.

## II. THEORETICAL STUDY

Figure 1 shows a schematic view of an electrostatic rectangular torsion actuator consisting of two identical springs, a movable plate and a stationary electrode. The horizontal distance from the center of the springs (i.e., the axis of rotation) to the nearest edge of the fixed electrode is  $a_1$ .  $a_2$  and  $a_3$  are the horizontal distances from the center of the springs to the end of the electrode and to the end of the movable plate, respectively. The electrode/plate width and vertical separation distance are  $b$  and  $d$ , respectively. The length, width and thickness of each spring are  $l$ ,  $w$ , and  $t$ , respectively. Before pull-in, the mechanical torque,  $M_m$  equals the electrostatic torque  $M_e$  [10], i.e.,

$$K_\alpha \alpha = \frac{\epsilon_0 V^2 b}{2\alpha^2} \left[ \frac{1}{1 - \frac{\beta\alpha}{\alpha_{\max}}} - \frac{1}{1 - \frac{\gamma\alpha}{\alpha_{\max}}} + \ln \left( \frac{\alpha_{\max} - \beta\alpha}{\alpha_{\max} - \gamma\alpha} \right) \right] \quad (1)$$

where  $\alpha$  is the angle between the rectangular plate and the electrode, the maximum constrained tilt angle  $\alpha_{\max} = d/a_3$ , the electrode length ratio  $\beta = a_2/a_3$  and the reduced electrode edge location  $\gamma = a_1/a_3$ .  $V$ ,  $\epsilon_0$  and  $K_\alpha$  are the applied voltage, the dielectric constant of the vacuum, and the spring constant, respectively. In typical designs  $a_1$  is much smaller than  $a_2$  or  $a_3$ . Thus  $\gamma$  can be approximated as 0. This reduces equation (1) to

$$K_\alpha \alpha = \frac{\epsilon_0 V^2 b}{2\alpha^2} \left[ \frac{1}{1 - \frac{\beta\alpha}{\alpha_{\max}}} - 1 + \ln \left( 1 - \frac{\beta\alpha}{\alpha_{\max}} \right) \right] \quad (2)$$

At the pull-in point, the mechanical spring constant  $K_\alpha$  (i.e.,  $dM_m/d\alpha$ ) is equal to the electrostatic spring constant (i.e.,  $dM_e/d\alpha$ ). Thus differentiating equation (2) with respect to  $\alpha$ , multiplying by  $\alpha$  and subtracting equation (2), yields

$$\frac{1}{1 - \beta\theta_{pin}} - 1 + \ln(1 - \beta\theta_{pin}) - \frac{\beta\theta_{pin}}{3(1 - \beta\theta_{pin})^2} + \frac{\beta\theta_{pin}}{3(1 - \beta\theta_{pin})} = 0 \quad (3)$$

where  $\theta$  is the fractional deflection of the rectangular plate,  $\alpha/\alpha_{\max}$ , and  $\theta_{pin}$  is the fractional deflection at pull-in. Solving equation (3) yields

$$\beta\theta_{pin} \cong 0.4404 \quad (4)$$

When the electrode length ratio  $\beta=1$ ,  $\theta_{pin} \cong 0.4404$ , which means that the full plate electrode design gives about 44.04% travel range, a well-known result[2-6, 10]. When  $\beta=0.4404$ ,  $\theta_{pin}=1$ , i.e.,  $\alpha=\alpha_{\max}$ . For lower electrode length ratios and a uniform gap depth, pull-in does not occur.

As shown by Degani, et al., [7], the pull-in voltage  $V_{pin}$  can be obtained from equation (1),

$$V_{pin} = \sqrt{\frac{2K_{\alpha}d^3}{\epsilon_0 a_3^3 b} \frac{\theta_{pin}^3}{\left[ \frac{1}{1-\beta\theta_{pin}} - \frac{1}{1-\gamma\theta_{pin}} + \ln\left(\frac{1-\beta\theta_{pin}}{1-\gamma\theta_{pin}}\right) \right]}} \quad (5)$$

For typical designs where  $\gamma \approx 0$  (i.e., the nearest edge of the rectangular electrode is close to the torsion spring) and  $\beta\theta_{pin} \approx 0.4404$ , the pull-in voltage expression in equation (5) can be simplified as

$$V_{pin} \approx \sqrt{\frac{9.68K_{\alpha}\alpha_{pin}^3}{\epsilon_0 b}} \quad (6)$$

where  $\alpha_{pin}$  is the pull-in angle. Based on equation (6), if the pull-in angle and voltage are set, there would be numerous combinations of  $K_{\alpha}$  and  $b$  to satisfy the pull-in design. Note that in equation (6)  $V_{pin}$  is expressed in terms only of the spring constant, the rectangular plate width and the specified pull-in angle. For completeness, we note that  $\alpha_{pin}$  can be written as

$$\alpha_{pin} \approx 0.4404 \frac{d}{a_2} \quad (7)$$

and the pull-in voltage can be expressed as

$$V_{pin} \approx 0.909 \sqrt{\frac{K_{\alpha}d^3}{\epsilon_0 b a_2^3}} \quad (8)$$

Additional design generalizations can be made by normalizing the applied voltage and resulting tilt angle by their respective pull-in values in equations (2) and (6). Thus taking  $X = \alpha/\alpha_{pin}$  and  $Y = V/V_{pin}$ , the equations become

$$\frac{Y^2}{X^3} \frac{\left[ \frac{1}{1-0.44X} - 1 + \ln(1-0.44X) \right]}{0.2065} \cong 1 \quad (9)$$

and

$$V_{\alpha,X} \approx Y \sqrt{\frac{9.68K_{\alpha}\alpha^3}{\epsilon_0 b X^3}} \quad (10)$$

Equation (9) is a general structural equation for electrostatic torsion actuators with rectangular plates. It shows that the relationship between the normalized applied voltage and the normalized tilt angle is independent of the spring parameters, the rectangular plate width and length, the air gap depth and the electrode length and width if the nearest edge of the electrode under the rectangular plate is close to the torsion spring. In equation (10),  $V_{\alpha,X}$  is the required applied voltage for tilt angle  $\alpha$  at working point  $X$ . If  $\alpha$  is fixed at a maximum desired value, designers can select different working points to realize a particular actuation. For instance,  $X=0.9$  can be used to avoid the bad controllability at the pull-in point  $X=1.0$ . Then the voltage corresponding to  $\alpha$  at  $X$  can be obtained. Note that in equation (10)  $V_{\alpha,X}$  is expressed in terms only of the spring constant, the rectangular plate width, the specified angle, the normalized applied voltage and the normalized tilt angle.



Based on equations (4), (9) and (10), a straightforward design approach can be developed in which only simple calculations are needed for the full design of a rectangular electrostatic torsion actuator. Figure 2 shows a schematic view of the approach. In this figure,  $\otimes_\alpha$  is the resonant frequency for the torsion mode. The resonant frequency  $\otimes_\alpha$  is determined using

$$f_\alpha = \frac{1}{2\pi} \sqrt{\frac{K_\alpha}{I_\alpha}} \quad (11)$$

where  $I_\alpha$  is the mass moment of inertia about the rotation axis, which can be written as

$$I_\alpha = \iiint \rho(y^2 + z^2) dx dy dz \approx \frac{1}{3} \rho a_3 b w (a_3^2 + w^2) \quad (12)$$

where  $\rho$  is the material density. When  $t < w$ , the spring constant can be written as

$$K_\alpha = \frac{2}{3} G \frac{wt^3}{l} \left[ 1 - \frac{192t}{\pi^5 w} \sum_{n=1,3,5,\dots} \frac{1}{n^5} \tanh\left(\frac{n\pi w}{2t}\right) \right] \quad (13)$$

where  $G$  is the shear modulus and equals  $0.73 \times 10^{11}$  Pa for silicon[11].

Referring to figure 2, if the desired maximum controllable tilt angle  $\alpha$ , the working point  $X$ , and the required applied voltage  $V_{\alpha,X}$  are set by the designer, the spring constant can be obtained after choosing the rectangular plate width  $b$ . Then, the designer can choose the spring length, width and thickness based on the spring constant equation, the desired resonant frequency and practical fabrication considerations. With  $\alpha$  and  $X$ , the pull-in angle  $\alpha_{\text{pin}}$  can be obtained. After choosing the fractional deflection at pull-in  $\theta_{\text{pin}}$ , both the electrode length ratio  $\beta$ , and the maximum constrained tilt angle  $\alpha_{\text{max}}$  can be calculated. Specifying one of either the plate length  $a_3$  or electrode spacing  $d$  allows the other to be determined. Using  $\beta$  and  $a_3$ , the electrode length  $a_2$  can be obtained. Finally, by combining  $b$ ,  $a_3$  and the spring constant, the torsion mode resonant frequency,  $\otimes_\alpha$ , can be calculated. If the value of  $\otimes_\alpha$  is acceptable, then the design procedure stops. Otherwise, redesign is needed.

### III. VERIFICATION

To verify the simplified approach to actuator design outlined in figure 2, we compare the results of the key calculations in equations (4), (6), (9) and (10) individually with results from both full analytical calculations and MEMCAD simulations using typical design parameters. Four different devices are considered during the verification process. Their dimensions are listed in the table 1.

Device 1 in Table 1 is used for the verification of equation (4). For this device, table 2 shows the calculated fractional deflection at pull-in  $\theta_{\text{pin}}$ , and the product of  $\theta_{\text{pin}}$  with the electrode length ratio  $\beta$  for three values of  $\beta$ , 0.4404, 0.75 and 1. These results have been determined using both the full analytical calculation (a) and MEMCAD version 4.8 simulation (M). As predicted in equation (4),  $\beta\theta_{\text{pin}}$  is always approximately equal to 0.44. The MEMCAD meshing and convergence parameters are listed in the table.

Devices 1 (with  $\beta=0.75$ ) and 2 in Table 1 are used to verify the result from equation (6). The plate width and spring parameters of these two actuators are the same, however, the plate length and gap depth are different. Table 3 confirms that pull-in voltages are roughly the same at the same pull-in angle  $\alpha_{\text{pin}}$  for the two devices, as predicted in equation (6).

Devices 2 and 3 in Table 1, with completely different design parameters, are used to verify the relationship described in equation (9). Figure 3 plots analytical and MEMCAD solutions of  $X$  versus  $Y$  for devices 2 and 3 along with equation (9). The curves are nearly indistinguishable, thus confirming equation (9).

Devices 2 and 4 in table 1 are used to verify the relationship in equation (10). Table 4 shows the calculation and simulation results for the two structures with different rectangular plate length and air gap depth, but with the same plate width and spring parameters. Device 4 is designed using the approach in figure 2 to operate identical to Device 2, at the same working point  $X=0.8$ , with the same maximum controllable tilt angle  $\alpha=1.3435^\circ$  and the same applied voltage  $V_{\alpha,X}=97.5V$ . This behavior is confirmed by the simulation and calculation results. By comparing the analytical and MEMCAD simulation results, for example, the values of  $\beta\theta_{pin}$  in Table 2, the values of  $V_{pin}$  and  $\alpha_{pin}$  in table 3, the values of  $Y(X)$  in figure 3 or the values  $\theta_{pin}$  and  $\alpha_{pin}$  in table 4, the fractional difference is generally found to be smaller than 3%.

#### IV. EXAMPLE APPLICATION

As an example application, we wish to design an actuator that has a maximum controllable tilt angle  $\alpha=1^\circ$  at working point  $X=0.95$  and applied voltage  $V_{\alpha,X}=48V$ . For this specific application, we choose a plate width  $b=0.7mm$ , a plate length  $a_3=0.7mm$ , and a fractional deflection at pull-in  $\theta_{pin}=1$ . Following the procedure of figure 2, the required spring constant is found to be  $K_\alpha=2.405\times10^{-7}N\cdot m$ . Practical fabrication considerations and the desire for a very flat plate surface require the spring width to be  $w=50\mu m$  and spring thickness  $t=5\mu m$ , thus the spring length  $l=1185\mu m$ . A folded spring can be used to achieve this length. The resulting resonant frequency  $\otimes_\alpha$  is found to be 806Hz. The pull-in angle  $\alpha_{pin}\cong1.053^\circ$ , the electrode length ratio  $\beta\cong0.4404$ ,  $\alpha_{max}\cong1.053^\circ$ ,  $d\cong12.9\mu m$  and  $a_2\cong308\mu m$ .

To compare our design results with a fabricated device, we also consider a full plate actuator with  $\beta=1$ . A full plate actuator is easy to construct because the silicon substrate can be used as the fixed electrode. Using the design approach of figure 2, for this device  $\alpha_{pin}\cong0.464^\circ$  and  $V_{pin}=14.18V$ . At working point  $X=0.95$ ,  $\alpha\cong0.44^\circ$ ,  $V_{\alpha,X}=14.16V$ . Figure 4 shows an optical profilometry image of this device biased at pull-in. The image was measured using a VEECO NT 3300 system. Fabrication was accomplished using deep reactive ion etching and ultra thin wafer bonding technology[12]. The finished device differs slightly from the design, having a measured gap depth of  $11.2\mu m$  instead of  $12.9\mu m$ . Figure 5 shows the actuated angle and fractional deflection versus applied voltage, as measured using the profilometer. The fractional deflection near pull-in is 43.75% at  $V=11.75V$  which is very close to the theoretical value of 44.04% at a calculated pull-in voltage of  $11.47V$  for  $d=11.2\mu m$ . We also note that  $\alpha(0V)=0.0463^\circ$ , which is the result of the gravity force. This value is very close to the theoretical prediction of  $0.0466^\circ$ .

#### V. LIMITATIONS OF THE THEORY

The theory and the equations used in this paper have not considered 1) spring stiffening, 2) fringing fields and 3) the effect of bending mode actuator movement. Also,

in the calculation, the angle  $\alpha$  is approximately treated as  $\tan(\alpha)$ . This will give rise to less than 1% error even at  $10^\circ$ . Of the limitations, the bending mode effect will most strongly affect the application range of the theory. In order to get a large tilt angle at a reasonably low applied voltage, the springs need to be as long and thin as possible for a given plate thickness. However, if the springs are too long, the resulting electrostatic force induced bending mode movement will decrease the effective gap depth between the electrodes, decreasing both the pull-in angle and voltage.

For a double clamped structure, the spring constant of the bending mode  $K_z$  can be written as

$$K_z = \frac{192EI}{(2l)^3} = \frac{3}{2} \frac{Ew^3t}{l^3} \quad (14)$$

where  $E$  is the Young's modulus in the direction of bending mode. In this paper,  $E$  is  $1.31 \times 10^{11}$  Pa for (100) silicon[11].  $K_z$  decreases with  $l^{-3}$ , whereas  $K_\alpha$  decreases with  $l^{-1}$ . The resonant frequency of the bending mode  $f_z$  can be written as

$$f_z = \frac{1}{2\pi} \sqrt{\frac{K_z}{m}} \quad (15)$$

where  $m$  is the mass of the suspended structure.

To illustrate the effects of spring length on bending mode movement, and its impact on the simplified design approach of the paper, we have designed three devices A, B, and C, with target pull-in angles of 2.98, 3.90 and 4.38 degrees, respectively at 100 V. Only the spring length and gap depth vary. Table 5 shows the pull-in angle and the pull-in voltage for these three devices determined using both the design approach of the paper and MEMCAD simulations. Notice that the MEMCAD results predict serious decreases in the pull-in angle and voltage for the longer springs of Devices B and C.

A measure of the importance of the bending mode compared to the torsion mode can be obtained by calculating the resonant frequencies for each mode. Table 6 shows  $f_\alpha$ ,  $f_z$ ,  $f_\alpha/f_z$  and fractional differences in pull-in angle and voltage using MEMCAD and the theory in this paper for devices 1 ( $\beta=0.75$ ), 2, 3, 4, A, B and C. Notice that the fractional differences in pull-in angle and pull-in voltage are generally small (<3%) when the ratio of the resonant frequency of the torsion mode to that of the bending mode,  $f_\alpha/f_z$ , is small (<0.1%). For devices A, B and C, with longer springs that are more prone to bending, the fractional differences and the value of  $f_\alpha/f_z$  become large. The fractional differences for device C exceed 20%. From the simulation results in tables 5 and 6, we conclude that a pull-in angle of  $4^\circ$  would be difficult to obtain with  $w=10\mu\text{m}$ ,  $t=2\mu\text{m}$ ,  $a_3=200\mu\text{m}$  and  $b=300\mu\text{m}$ . In general, the design approach of this paper is useful only for actuators in which the torsion mode is dominant. For the designs we considered, we find that for  $f_\alpha/f_z < 0.1$ , the fractional difference between analytical calculations and MEMCAD simulations is <3%.

## VI. CONCLUSIONS

This paper has presented several basic equations to describe rectangular electrostatic torsion actuators, which may give designers a better understanding of their performance. Based on these equations, a straightforward, angle based design approach has been

proposed, which can avoid time consuming simulations. The results have been verified by comparing them with analytical calculations and MEMCAD simulations with fractional difference smaller than 3% for torsion mode dominant actuators. Also, good agreement is found by comparison with the measured behavior of a microfabricated full-plate device.

## ACKNOWLEDGEMENT

This work was partially supported by the NJ Commission on Science and Technology through the NJ MEMS Initiative, and by NSF through award No. DMR-9871272.

## REFERENCES

- [1] J. A. Walker, "The future of MEMS in telecommunications networks," *J. Micromech. Microeng.*, vol. 10, pp.R1-R7, 2000.
- [2] J. Buhler, J. Funk, J. G. Korvink, F. P. Steiner, P. M. Sarro, and H. Baltes, "Electrostatic aluminum micromirrors using double-pass metallization," *IEEE J. Microelectromech. Syst.*, vol. 6, no.2, pp.126-135, 1997.
- [3] H. Toshiyoshi and H. Fujita, "Electrostatic micro torsion mirrors for an optical switch matrix," *IEEE J. Microelectromech. Syst.*, vol. 5, no.4, pp. 231-237, 1996.
- [4] S. W. Chung, J. W. Shin, Y. K. Kim, and B. S. Han, "Design and fabrication of micromirror supported by electroplated nickel posts," *Sens. Actuators A*, vol. 54, pp. 464-467, 1996.
- [5] Y. Uenishi, M. Tsugai, and M. Mehregany, "Micro-opto-mechanical devices fabricated by anisotropic etching of (110) silicon," in *IEEE Proc.-Microelectromechanical Syst.*, pp. 319-324, Jan. 1994.
- [6] M. Fischer, M. Giousouf, J. Schaepperle, D. Eichner, M. Weinmann, W. von Munch, and F. Assmus, "Electrostatically deflectable polysilicon micromirrors-Dynamic behavior and comparison with results from FEM modeling with ANSYS," *Sens Actuators A*, vol. 67, pp. 89-95, 1998.
- [7] L. J. Hornbeck, "Deformable-mirror spatial light modulators", *SPIE Critical Review Series*, vol.1150, *Spatial Light Modulators and applications III*, pp. 86-102,1989.
- [8] P. M. Osterberg, "Electrostatically actuated micromechanical test structures for material property measurements", Ph.D dissertation, Dept . Elec. Eng. Comput. Sci., Massachusetts Institute of Technology, September, 1995.
- [9] R. K. Gupta, "Electrostatic pull-in test design for in-situ mechanical property measurements of microelectromechanical systems(MEMS)", Ph.D dissertation, Dept . Elec. Eng. Comput. Sci., Massachusetts Institute of Technology, June, 1997.
- [10] O.Degani, E. Socher, A. Lipson, T.Leitner, D. J. Setter, S. Kaldor, and Y. Nemirovsky, "Pull-in study of an electrostatic torsion microactuator," *IEEE J. Microelectromech. Syst.*, vol. 7, no.4, pp. 373-379, 1998.
- [11] S. P. Timoshenko and I. N. Goodier, *Theory of Elasticity*. New York: McGraw-Hill, 1970, ch. 3, pp.40-46.

[12] R. A. Brown, V. Aksyuk and K. R. Farmer, "Micromachined, electrostatically-actuated optical modulators fabricated by fusion bonding of single-crystal, ultra-thin silicon wafers," in *Proc. the 5<sup>th</sup> International Symposium on Semiconductor Wafer Bonding: Science, Technology and Applications*, Honolulu, Hawaii, Oct. 17-22, 1999, Electrochemical Society Proceedings, Vol. 99-35, pp. 407.

### Figure captions

Figure 1 A schematic view of a rectangular electrostatic torsion actuator, consisting of two springs, a movable rectangular plate, and a stationary electrode.  $a_1$  is the distance between the axis of torsion to the nearest edge of the electrode plate,  $a_2$  is the distance to the end of the plate,  $a_3$  is the distance to the end of the proof mass.  $d$  is the air gap depth and  $b$  is the width of the rectangular plate.

Figure 2 A schematic view of the design principle. The tilt angle  $\alpha$ , the applied voltage  $V_{\alpha, X}$ , the rectangular plate width  $b$ , the working point  $X$ , the air gap depth  $d$  (or the rectangular plate length  $a_3$ ) and the fractional deflection at pull-in  $\theta_{pin}$  are the input parameters. The spring parameters, the rectangular plate length or gap depth, the electrode length  $a_2$  and the torsion mode resonant frequency are the output parameters.

Figure 3 Curves of  $X$  versus  $Y$  for devices 2 and 3 determined using analytical calculations, MEMCAD simulations and equation (9).  $X$  is the ratio of the tilt angle to pull-in angle.  $Y$  is the ratio of the applied voltage to pull-in voltage. For the MEMCAD simulation of device 3, a 27 node element was used for structure meshing. The node number is 8478 and the convergence tolerance is  $1 \times 10^{-3}$ . The pull-in voltage by the design approach is 166.73V and the pull-in voltage by MEMCAD is  $99.16V < V_{pin} < 99.18V(M)$ . The pull-in angle by the design approach is  $2.525^\circ$ , and the pull-in angle by MEMCAD is  $2.537^\circ$ .

Figure 4 Optical profilometry image of a fabricated, full-plate torsion actuator under test. The applied voltage is 11.85V and the movable plate is snapped down to the bottom electrode.  $w=50\mu m$ ,  $t=5\mu m$ ,  $l=1185\mu m$ ,  $a_3=700\mu m$ ,  $b=700\mu m$ ,  $d=11.2\mu m$  and  $\beta=1$ .

Figure 5 Measured tilt angle  $\alpha$  and fractional deflection versus applied voltage for the actuator in figure 4.

### Table captions

Table 1 Design parameters for the devices used to verify the main results of the theoretical study section of the paper.

Table 2 The calculated fractional deflection  $\theta_{pin}$ , and the product of  $\theta_{pin}$  and the electrode length ratio  $\beta$  for different values of  $\beta$ , 0.4404, 0.75 and 1, for device 1.

Table 3 Pull-in voltages and angles for devices 1 and 2, determined using full analytical calculations (a) and MEMCAD simulations (M). The two devices have different rectangular plate length, air gap depth and electrode length ratio, but they have the same spring parameters and rectangular plate width. The pull-in voltages are almost the same at the same pull-in angle.

Table 4 The simulation results for two structures with different rectangular plate length and air gap depth, but with the same rectangular plate width and spring parameters. At  $X=0.8$ , the applied voltage  $V_{\alpha, X}$ , is approximately equal to the values determined using equation (10).

Table 5 Pull-in angle and pull-in voltage for three devices determined using the design approach of this paper (d) and MEMCAD simulations (M). The design pull-in voltage is 100 V for three different design pull-in angles. The spring length and gap depth vary for each design.

Table 6 Calculated torsion and bending mode resonant frequencies for the different devices considered in this paper, and fractional differences in pull-in angle and voltage determined using the design approach of the paper (d) and MEMCAD simulations (M).

Table 1

	$l(\mu\text{m})$	$w(\mu\text{m})$	$t(\mu\text{m})$	$a_3(\mu\text{m})$	$b(\mu\text{m})$	$d(\mu\text{m})$	$a_2(\mu\text{m})$
Device 1	100	10	3	200	300	10	Variable, $a_2=a_3\beta$
Device 2	100	10	3	300	300	20	300
Device 3	200	20	3	400	400	25	250
Device 4	100	10	3	408.6	300	15	224.7

Table 2

	$\beta=1$	$\beta=0.75$	$\beta=0.4404$
$\theta_{\text{pin}}$	0.4404(64.42V)(a) 0.4381(65.41V)(M)	0.5872(99.18V)(a) 0.5733(99.16V)(M)	1.00005(220.41V)(a) 0.9843(216.04V)(M)
	Meshing and convergence (M): • 27 node element • node number: 10608 • $V_{\text{pin}}$ convergence range: 65.41V < $V_{\text{pin}}$ < 65.43V • Convergence tolerance: $1 \times 10^{-3}$	Meshing and convergence (M): • 27 node element • node number: 13536 • $V_{\text{pin}}$ convergence range: 99.16V < $V_{\text{pin}}$ < 99.18V • Convergence tolerance: $1 \times 10^{-3}$	Meshing and convergence (M): • 27 node element • node number: 10974 • $V_{\text{pin}}$ convergence range: 216.04V < $V_{\text{pin}}$ < 216.05V • Convergence tolerance: $1 \times 10^{-3}$
$\beta\theta_{\text{pin}}$	0.4404(a) 0.4381(M)	0.4404(a) 0.4300(M)	0.4404(a) 0.4335(M)

Table 3

	$V_{\text{pin}}(\text{V})$	$\alpha_{\text{pin}}(^{\circ})$
Device 1 ( $\beta=0.75$ )	99.18(a) 99.16V < $V_{\text{pin}}$ < 99.18V(M)	1.6830(a) 1.6418(M)
	Meshing and convergence (M): • 27 node element • node number: 13536 • Convergence tolerance: $1 \times 10^{-3}$	

Device 2( $\beta=1.0$ )	99.18V(a) 100.66V< $V_{pin}$ <100.68V(M)	1.6835(a) 1.6925(M)
	Meshing and convergence (M): <ul style="list-style-type: none"> <li>• 27 node element</li> <li>• node number: 12836</li> <li>• Convergence tolerance: <math>1 \times 10^{-3}</math></li> </ul>	

Table 4

	Device 2		Device 4		Equation (10)
X	0.8(a)	0.7591(M)	0.8(a)	0.7827(M)	0.8
Y	0.982	0.9686(M)	0.982	0.9788(M)	0.982
$\alpha(^{\circ})$	1.3436(a)	1.2848(M)	1.3435(a)	1.3149(M)	1.3435
$V_{\alpha,X}(V)$	97.4(a)	97.5(M)	97.4(a)	97.5(M)	97.5
$\theta_{pin}$	0.4404(a)	0.4429(M)	0.8(a)	0.7985(M)	
$\alpha_{pin}(^{\circ})$	1.6835(a)	1.6925(M)	1.6835(a)	1.6800(M)	
$\alpha_{max}(^{\circ})$	3.821		2.104		
$\beta$	1		0.55		
$V_{pin}(V)$	99.18(a)	100.66V< $V_{pin}$ <100.68V(M)	99.21(a)	99.61V< $V_{pin}$ <99.65V(M)	
	Meshing and convergence (M): <ul style="list-style-type: none"> <li>• 27 node element</li> <li>• node number: 12836</li> <li>• Convergence tolerance: <math>1 \times 10^{-3}</math></li> </ul>		Meshing and convergence (M): <ul style="list-style-type: none"> <li>• 27 node element</li> <li>• node number: 9876</li> <li>• Convergence tolerance: <math>1 \times 10^{-3}</math></li> </ul>		

Table 5

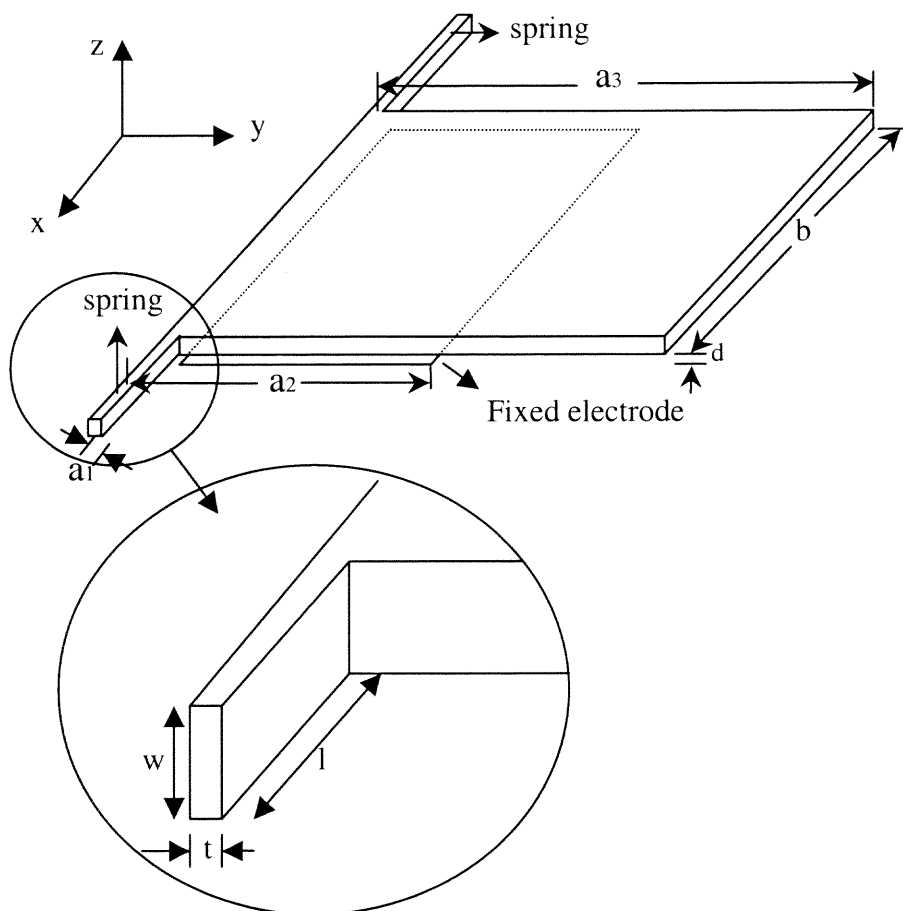
	Device A w=10 $\mu$ m, t=2 $\mu$ m, a <sub>3</sub> =200 $\mu$ m, a <sub>2</sub> =88.08 $\mu$ m, b=300 $\mu$ m	Device B w=10 $\mu$ m, t=2 $\mu$ m, a <sub>3</sub> =200 $\mu$ m, a <sub>2</sub> =88.08 $\mu$ m, b=300 $\mu$ m	Device C w=10 $\mu$ m, t=2 $\mu$ m, a <sub>3</sub> =200 $\mu$ m, a <sub>2</sub> =88.08 $\mu$ m, b=300 $\mu$ m
	l=174.8 $\mu$ m, d=10.4 $\mu$ m	l=390.9 $\mu$ m, d=13.6 $\mu$ m	l=552.8 $\mu$ m, d=15.3 $\mu$ m
$\alpha_{pin,d} (^{\circ})$ (design)	2.98	3.90	4.38
$\alpha_{pin,M} (^{\circ})$ (MEMCAD)	2.88	3.26	3.11
V <sub>pin,d</sub> (V)(design)	100	100	100
V <sub>pin,M</sub> (V)(MEMCAD)	95.41 V < V <sub>pin</sub> < 95.43V	86.45V < V <sub>pin</sub> < 86.46V	76.90V < V <sub>pin</sub> < 76.92V
	Meshing and convergence (M): • 27 node element • node number: 7932 • Convergence tolerance: 1 $\times 10^{-3}$	Meshing and convergence (M): • 27 node element • node number: 12018 • Convergence tolerance: 1 $\times 10^{-3}$	Meshing and convergence (M): • 27 node element • node number: 6402 • Convergence tolerance: 1 $\times 10^{-3}$

Table 6

	Device 1 ( $\beta=0.75$ )	Device 2	Device 3	Device 4	Device A	Device B	Device C
f <sub><math>\alpha</math></sub>	12.0KHz	6.55KHz	4.159KHz	4.12KHz	5.137KHz	3.435KHz	2.889KHz
f <sub>z</sub>	119.0KHz	97.1KHz	59.4KHz	83.2KHz	42.0KHz	12.6KHz	7.468KHz
f <sub><math>\alpha</math></sub> / f <sub>z</sub>	0.101	0.0675	0.07	0.0495	0.122	0.273	0.387
Fractional difference for $\alpha_{pin}$ , ( $\alpha_{pin,d}-\alpha_{pin,M}$ )/ $\alpha_{pin,d}$	2.45%	-0.53%	-0.47%	0.21%	3.36%	16.41%	29.00%
Fractional difference for V <sub>pin</sub> , (V <sub>pin,d</sub> -V <sub>pin,M</sub> )/V <sub>pin,d</sub>	0.02%	-1.49%	2.42%	-0.40%	4.59%	13.55%	23.10%



Figure 1



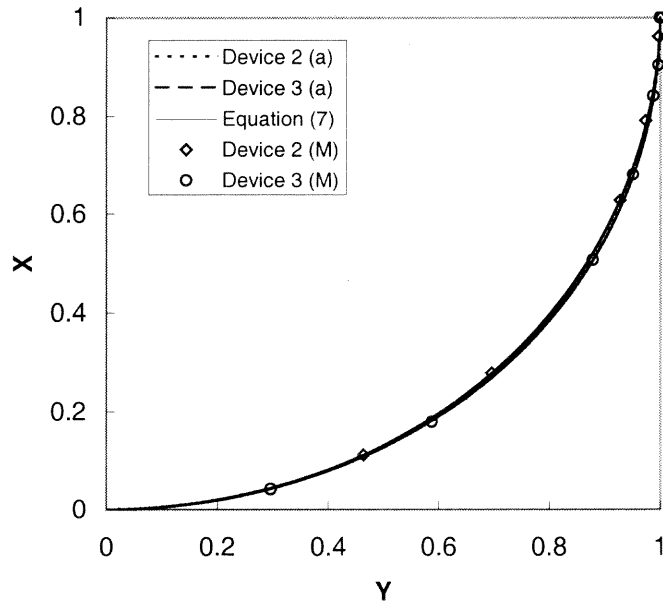


Figure 3

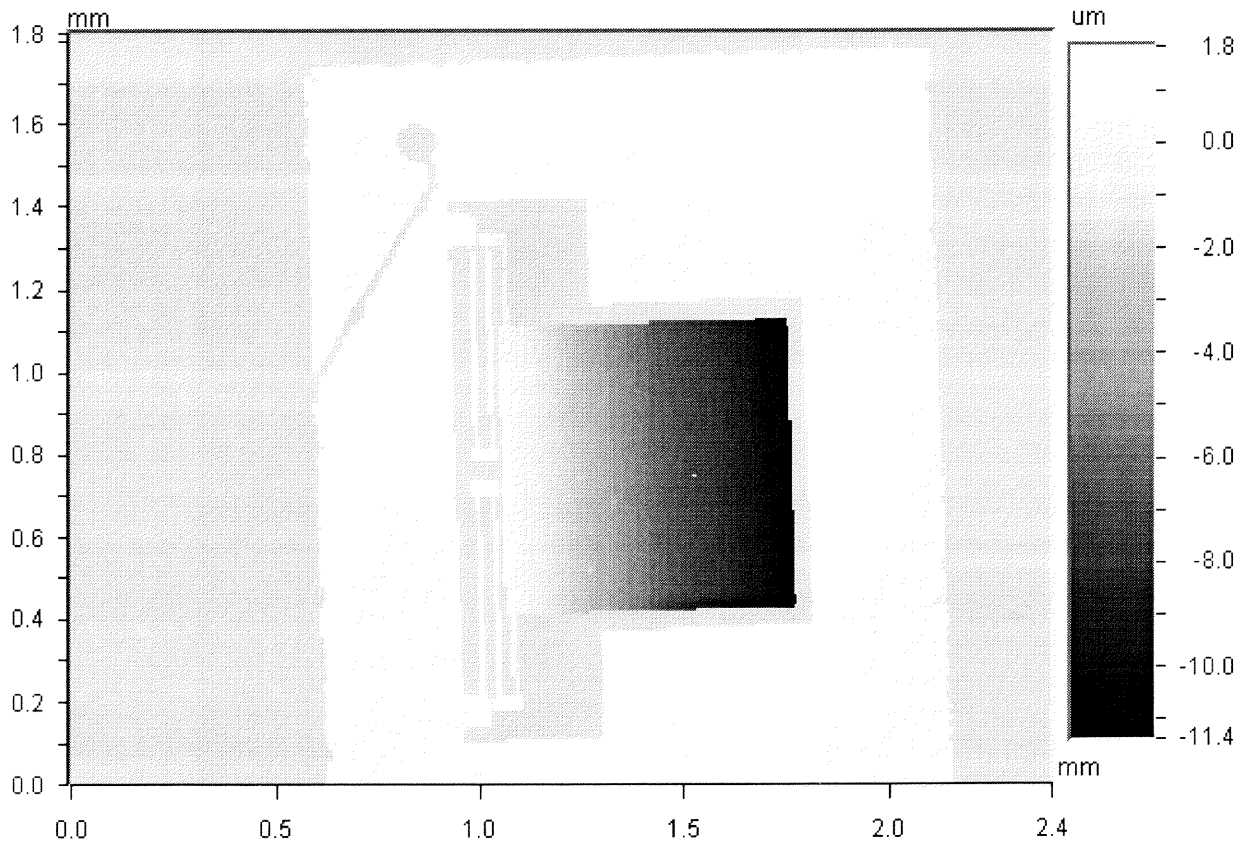


Figure 4

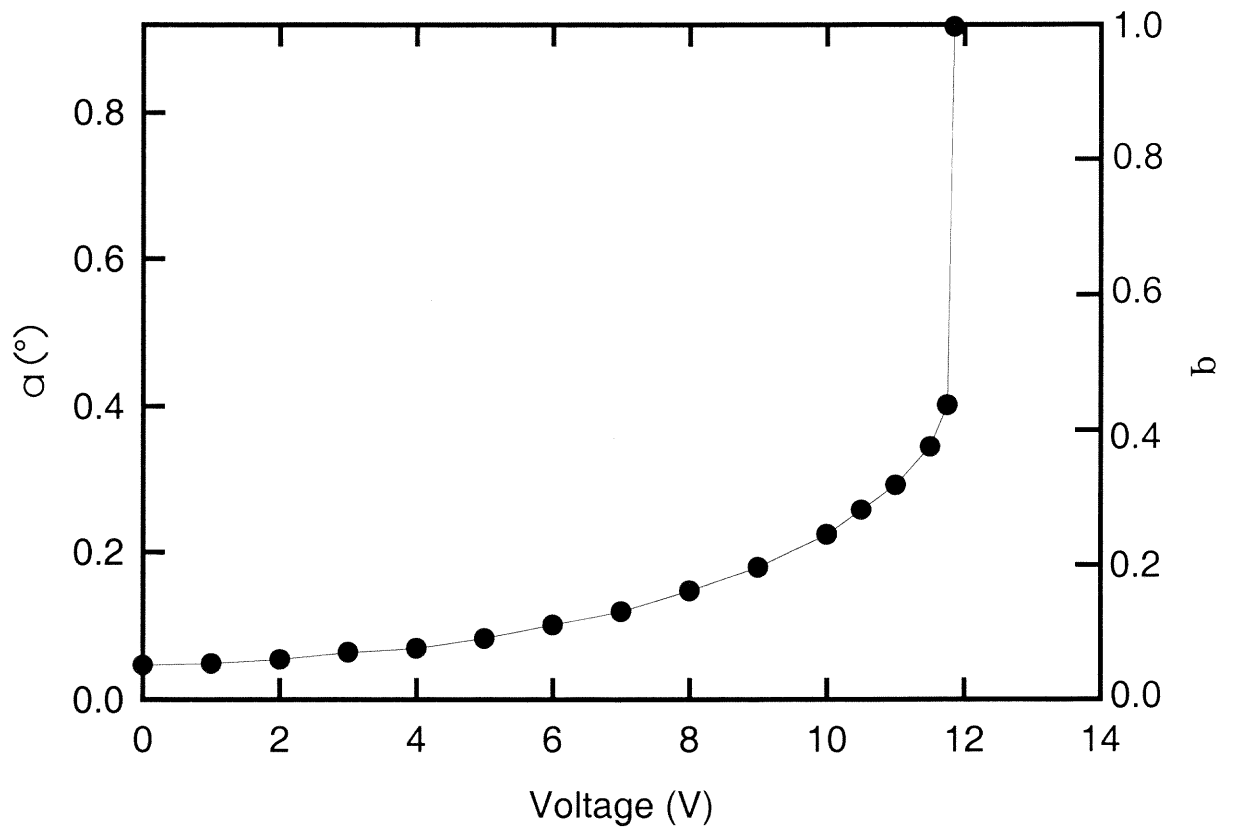


Figure 5





## REFERENCES

1. O.N. Tufte et al. 1963. "Piezoresistive Properties of Silicon Diffused Layers," *J App Phys*, 34:313.
2. Wu, M.C., "Micromachining for optical and Optoelectronic Systems," *Proceedings of the IEEE*, Vol. 85, No. 11, (November 1997), pp. 1833-1856.
3. K. Eric Drexler, "Nanosystems: Molecular Machinery, Manufacturing, and Computation", Appendix B, B. 8: Feynman's 1959 Talk, John Wiley & Sons (1992).
4. Lee, S.S., Motamedi, E., Wu, M.C., "Surface-micromachined free-space fiber optic switches with integrated microactuators for optical fiber communication systems," in *Proceedings of the 1997 International Conference of Solid-State Sensors and Actuators (TRANSDUCERS 97)*, 1997, paper 1A4.07P.
5. Barber B., Giles C.R., Askyuk V., Ruel R., Stulz L., Bishop D. "A fiber connectorized MEMS variable optical attenuator" *IEEE Photon. Tech. Lett.* 10, 1262-1264 (1998)
6. Lin L.Y., Shen J.L., Wu M.C., Segent A.M. "Tunable three-dimensional solid Fabry-Perot etalons fabricated by surface micromachining" *IEEE Photon. Tech. Lett.* 8, 101-103 (1996)
7. Petersen K.E. "Micromechanical light modulator array fabricated on silicon" *Appl. Phys. Lett.* 31, 521-523 (1977)
8. R. B. Apte, F. S. A. Sandejas, W. C. Banyai, and D. M. Bloom, "Deformable Grating Light Valves for High Resolution Displays", *Proceedings of the 1994 Solid-State Sensor and Actuator Workshop (Invited paper)*, Hilton head, SC, June 13-16, 1994, pp. 1-6.
9. Feustel A., Müller J., Relling V. "A microsystem mass spectrometer", pp. 299-304 in *MicroTotal Analysis Systems*, van den Berg A., Bergveld P., Eds., Kluwer Academic Publishers, The Netherlands (1995)
10. Kiang M.-H., Solgaard O., Lau K.Y., Muller R.S. "Polysilicon optical microscanners for laser scanning displays" *Sensors and Actuators A70*, 195-199 (1998)
11. Senturia, S. D., "CAD for Microelectromechanical Systems", Invited Talk at *Transducers '95*, June 25-29, Stockholm, Sweden; also appears in the proceedings, Vol. 2, Paper No. 232-A7.

12. M.J. Daneman, N.C. Tien, O. Solgaard, K.Y. Lau, R.S. Muller, Actuated Microreflector with Two Degrees of Freedom and a Large Travel Range, Solid-State Sensor and Actuator Workshop, Hilton Head Island, South Carolina, June, 1996
13. M. T. A. Saif, B. E. Alaca, and H. Sehitoglu, "Analytical Modeling of Electrostatic Membrane Actuator for Micro Pump," IEEE Journal of Microelectromechanical Systems, September 1999, Vol. 08, No. 3, pp. 335.
14. D. Ishihara, M.J. Jeong, S. Yoshimura, G. Yagawa, and Y.J. Kim, "Structural Design of Micro Electrostatic Actuator for Optical Memory", The 4th International Conference on Modeling and Simulation of Microsystems, MSM 2001, pp. 157-160, 2001, Hilton Oceanfront Resort, Hilton Head Island, South Carolina, US.
15. A. M. Volpicelli, E. R. Deutsch, S. D. Senturia, "Use of Computer Microvision to Automate Electrostatic Material Property Measurement Procedures," *Transducers '99, Sendai Japan*, pp. 920-923, June 7-10 1999.
16. S. D. Senturia, N. Aluru, J. White: *Simulating the behavior of MEMS devices: computational methods and needs*. IEEE Computational Science & Engineering, January 1997, pp. 30-54.
17. J. E. Mehner, J. Wibbeler, F. Bennini, W. Dötzel: *Modeling and simulation of micromechanical components*. Proc. Workshop System Design Automation, Rathen b. Dresden 2000, pp. 163-177.
18. P. Schwarz: *Microsystems CAD: From FEM to System Simulation*. Proc. SISPAD '98, Leuven, pp. 141-148.
19. G. K. Fedder, Q. A. Jing: *A hierarchical circuit-level design methodology for micromechanical systems*. IEEE Trans. CAS-II 46(1999)10, pp. 1309-1315.
20. Ofir Degani, Eran Socher, Ariel Lipson, Tomer Leitner, Dan J. Setter, Shmuel Kaldor and Yael Nemirovsky, "Pull-in Study of an Electrostatic Torsion Microactuator," J. Microelectromech. Syst., vol. 7, pp. 373-379, 1998.
21. E. S. Hung and S. D. Senturia, "Extending the Travel Range of Analog-Tuned Electrostatic Actuators," J. Microelectromech. Syst., vol. 8, pp. 497-505, 1999.
22. Pottinger M., Eyre B., Kruglick E., Lin G. "MEMS: the maturing of a new technology" Solid State Technology, Sept. Issue, 89-96 (1997)

23. J.H. Comtois, M.A. Michalick, N. Clark and W. Cowan, "MOEMS for adaptive optics," *Broadband Optical Networks and Technologies: An Emerging Reality/Optical MEMS/Smart Pixels/Organic Optics and Optoelectronics*, 1998 IEEE/LEOS Summer Topical Meetings, pp. II/95 -II/96
24. M. Bartek, I. Novotny, J.H. Correia, V. Tvarozek, Quality factor of thin-film Fabry-Perot resonators: dependence on interface roughness, accepted for publication in *Journal Sensors and Actuators A*, Elsevier Science, 2000.
25. R. Puers and D. Lapadatu, "Electrostatic forces and their effects on capacitive mechanical sensors," *Sensors and Actuators A*, vol. 56, pp. 203-210, 1996.
26. Ofir Degani, Eran Socher, Ariel Lipson, Tomer Leitner, Dan J. Setter, Shmuel Kaldor and Yael Nemirovsky, "Pull-in study of an electrostatic torsion microactuator," *J. Microelectromech. Syst.*, vol. 7, pp. 373-379, 1998
27. E. K. Chan and R. W. Dutton, "Electrostatic micromechanical actuator with extended range of travel," *J. Microelectromech. Syst.*, vol. 9, pp. 321-328, 2000.
28. R. Legtenberg, J. Gilbert and S. D. Senturia, "Electrostatic curved electrode actuators," *J. Microelectromech. Syst.*, vol. 6, pp. 257-265, 1997.
29. Olivier Francais and Isabelle Dufour, "Enhancement of elementary displaced volume with electrostatically actuated diaphragms: application to electrostatic
30. E. S. Hung and S. D. Senturia, "Extending the Travel Range of Analog-Tuned Electrostatic Actuators," *J. Microelectromech. Syst.*, vol. 8, pp. 497-505, 1999.
31. P. M. Osterberg and S. D. Senturia, "M-TEST: A test chip for MEMS material property measurement using electrostatically actuated test structures," *J. Microelectromech. Syst.*, vol. 6, pp. 107-118, 1997.
32. Z. X. Xiao, X. T. Wu, W. Y. Peng and K. R. Farmer, "An Angle Based Design Approach for Rectangular Electrostatic Torsion Actuators," *J. Microelectromech. Syst.*, (accepted).
33. X. T. Wu, Z. Xiao, J. Zhe and K. R. Farmer, "Modeling and Simulation of Two Passive Feedback Methods to Obtain Large Travel Range of Electrostatic Micro Mirrors," *Proc. 4<sup>th</sup> Int. Conf. Modeling and Simulation of Microsystems*, Hilton Head, SC, March 19-21, 2001, pp. 382-385.
34. Xingtao Wu, Richard A Brown, Smitha Mathews and K.R. Farmer, "The Effects of Oxide on the Travel Range Extension of Electrostatic Micro Mirror", *OMEMS 2000*, IEEE, pp. 198-199.



35. Jiang Zhe, Xingtao Wu, Jin Cheng, Jingshan Wang and K. R. Farmer, "Analytic Pull-in Study on Non-deformable Electro Static Micro Actuators", submitted to IEEE 2001 International Electron Device Meeting.
36. J. Guckenheimer and P. Holmes, *Nonlinear Oscillations, Dynamical Systems, and Bifurcations of Vector Fields*. New York, Springer Verlag, 1983.
37. H. B. Palmer, "The Capacitance of a parallel-Plate Capacitor by the Schwartz-Christoffel transformation", *Electrical Engineering* 56, pp. 363-366, March, 1937.
38. Hitoshi Nishiyama and Mitsunobu Nakamura, "Capacitance of Disk Capacitor" *IEEE transactions on components, hybrids, and manufacturing technology*. Vol. 16, No. 3.
39. D. J. Bishop, and V. A. Aksyuk, "Optical MEMS Answer High-Speed Networking Requirements," *Electronic Design*, April 5, 1999, pp. 85-92.
40. J. E. Ford, V. A. Aksyuk, D. J. Bishop, and J.A. Walker, "Wavelength Add/Drop Switching Using Tilting Micromirrors," *J. Lightwave Technol.*, Vol. 17, No. 5, May 1999, pp. 904-911.
41. L. Y. Lin, E. L. Goldstein, and R. W. Tkach, "Free-space micromachined optical switches with sub-millisecond switching time for large-scale optical crossconnects," *IEEE Photonics Technol. Lett.*, April 1998.
42. N. A. Jackman, S.H. Patel, B. P. Mikkelsen, and S. K. Korotky, "Optical Cross Connect for Optical Networking," *Bell Labs Technical Journal*, Vol. 4, No. 1, 1999, pp. 262-281.
43. S. -S. Lee, L.-S. Huang, C. -J. Kim, and M. C. Wu, "Free space fiber-optic switches based on MEMS vertical torsion mirror," *J. Lightwave Technol.*, vol 17, no. 1, pp. 7-13, 1999.
44. C. Marxer and N. F. de Rooij, "Micro-opto-mechanical 2x2 switch for single-mode fibers based on plasma-etched silicon mirror and electrostatic actuation," *J. Lightwave Technol.*, vol. 17, no.1, pp. 2-6, 1999.
45. S. S. Lee, E. Motomedi, and M. C. Wu, "Surface-micromachined free space fiber optic switches with integrated microactuators for optical fiber communication systems," in *Transducer'97*, Chicago, IL, June 16-19, 1997.
46. J. E. Ford, J. A. Walker, D. S. Greywall and K. W. Goossen, "Micromechanical Fiber-Optic Attenuator," *Journal of Lightwave Technology*, vol. 16. no. 9, September 1998, pp. 1663-1670.

47. C. R. Giles, V. Aksyuk, B. Barber, R. Ruel, L. Stulz and D. Bishop, "A Silicon MEMS Optical Switch Attenuator and Its Use in Lightwave Subsystems," IEEE Journal of Selected Topics in Quantum Electronics, vol. 5. no. 1, January/February 1999, pp. 18-25.
48. R. A. Brown, V. A. Aksyuk and K. R. Farmer, "Micromachined, Electrostatically-actuated Optical Modulators Fabricated by Fusion Bonding of Single-Crystal, Ultra-Thin Silicon Wafers", ECS-Hawaii, JECS, 1999
49. J. E. Ford and J. A. Walker, "Dynamic spectral power equalization using micro-optomechanics," IEEE photon. Technol. Lett., vol. 10, pp. 1440-1442.
50. J. D. Patterson, "Micro-mechanical Voltage-Tunable Fabry-Perot Filters Formed in (111) Silicon, Ph.D. Thesis, University of Colorado, 1997.
51. Moller, S.; Amann, M.-C. "Tuning performance and spectral selectivity of widely tunable vertical Mach-Zehnder lasers," Quantum Electronics, IEEE Journal of , Volume: 36 Issue: 2 , Page(s): 192 –197, Feb. 2000.
52. B. E. Deal, "The Current Understanding of Charges in the Thermally Oxidized Silicon Structure," *J. Electrochem. Soc.: Solid-State Science and Technology*, Vol. 127, No. 4 (April 1980), pp. 979-981.
53. S. M. Sze, *Physics of Semiconductor Devices*, New York: John Wiley & Sons, 1969.
54. Price, R. H., J. E. Wood, and S. C. Jacobsen, "The Modeling of Electrostatic Forces in Small Electrostatic Actuators," Tech. Digest. IEEE. Solid-State Sensor and Actuator Workshop, June 1988, pp. 131-135.
55. Trimmer, W. S. N., and K. J. Gabriel, "Design Considerations for a Practical Electrostatic Micro-Motor," *Sensors and Actuators*, Vol. 11, No. 2, 1987, pp. 189-206.
56. Ostenberg, P., H. Yie, X. Cai, J. White and S. Senturia, "Self-Consistent Simulation and Modeling of Electrostatically Deformed Diaphragms," IEEE Micro Electro Mechanical Systems Workshop, 1994, pp. 28-32.
57. "User Guide" and "Reference" of MEMCAD<sup>TM</sup> 4.8 Software of Conventor. Inc.
58. James A Walker, "The future of MEMS in telecommunications networks", *J. Micromech. Microeng.* 10 (2000) R1-R7.
59. Max Born and Emil Wolf, "Principles of Optics", Pergamon Press, 1980.
60. Lorentz H, Despont M, Fahrni N, LaBianca N C, Renaud P and Vettiger P, *J. Micromech. Microeng.* 7, 121-124, 1997.

61. Lorentz H, Despont M, Fahrni N, Brugger J, Vettiger P, Renaud P Sensors and Actuators A 64, 33-39, 1998.
62. Cai X, Glidle A and Cooper J M Electroanalysis **12** (9), 2000.
63. S. K. Sampath, L. St. Clair, Xingtao Wu, D. V. Ivanov, Q. Wang, C. Ghosh and K. R. Farmer, "Rapid MEMS Prototyping using SU-8, Wafer Bonding and Deep Reactive Ion Etching", Proceedings of 13<sup>th</sup> Conference of UGIM, May, 2001.
64. Co-Research Report (Princeton Optronics. Inc. and MRC, NJIT)
65. David A. Koester, Ramaswamy Mahadevan, Busbee Hardy and Karen W. Markus "MUMPs™ Design Handbook, Revision 6.0," Cronos Integrated Microsystems, A JDS Uniphase Company.
66. Peter Enoksson, "Novel Resonant Micromachined Silicon Devices for Fluid Applications," Ph.D. Thesis, Royal Institute of Technology, 1997, ISSN 0281-2878.
67. Peter Enoksson, Goran Stemme and Erik Stemme, "Fluid Density Sensor Based on Resonance Vibration," Sensors and Actuators A 46-47 (1995) pp. 327-331.
68. Peter Enoksson, Goran Stemme and Erik Stemme, "Silicon Tube Structures for a Fluid Density Sensor," Sensors and Actuators A 54 (1996) pp. 558-562.
69. David Westberg, Oliver Paul, Gert Andersson and Henry Baltes, "A CMOS-Compatible Fluid Density Sensor," J. Micromech. Microeng. 7 (1997), pp. 253-255.